

RESOLVING THREE-DIMENSIONAL IMPACTS ON UNDERSTANDING  
CASCADIAN SUBDUCTION ZONE CONDUCTIVITY AND FLUID  
STRUCTURES

by

BLAKE ANTHONY PARRIS

A DISSERTATION

Presented to the Department of Physics  
and the Graduate School of the University of Oregon  
in partial fulfillment of the requirements  
for the degree of  
Doctor of Philosophy

June 2020

DISSERTATION APPROVAL PAGE

Student: Blake Anthony Parris

Title: Resolving Three-dimensional Impacts on Understanding Cascadian Subduction Zone Conductivity and Fluid Structures

This dissertation has been accepted and approved in partial fulfillment of the requirements for the Doctor of Philosophy degree in the Department of Physics by:

Richard Taylor	Chair
Dean Livelybrooks	Advisor
James Imamura	Core Member
Douglas Toomey	Institutional Representative

and

Kate Mondloch	Interim Vice Provost and Dean of the Graduate School
---------------	--

Original approval signatures are on file with the University of Oregon Graduate School.

Degree awarded June 2020

© 2020 Blake Anthony Parris

.

## DISSERTATION ABSTRACT

Blake Anthony Parris

Doctor of Philosophy

Department of Physics

June 2020

Title: Resolving Three-dimensional Impacts on Understanding Cascadian Subduction Zone Conductivity and Fluid Structures

The Magnetotelluric Observations of Cascadia using a Huge Array (MOCHA) experiment provides amphibious data useful for imaging subducted fluids from trench to mantle wedge corner. A type of seismic activity known as Episodic Tremor and Slip is thought to play a key role in regional seismic activity along the Cascadian Subduction Zone, potentially influencing future mega thrust earthquakes. Through magnetotelluric imaging providing 3-D electrical conductivity maps of the Cascadia subduction zone we have discovered correlation between possible fluid concentrations and Episodic Tremor and Slip.

In using MOD3DEM, a finite difference inversion package, we encountered problems inverting sea floor stations due to the strong, nearby conductivity gradients and stations exhibiting out of quadrant phase anomalies. We introduce improved interpolation schemes that more accurately track EM fields across large conductivity gradients at cell boundaries, with an eye to enhancing the accuracy of the simulated



responses and, thus, inversion results. With a future aim of inverting the stations exhibiting these phase anomalies, we use forward models to determine what geologically feasible structures could produce the observed anomalous behavior.

This dissertation includes previously unpublished co-authored material.

## CURRICULUM VITAE

NAME OF AUTHOR: Blake Anthony Parris

### GRADUATE AND UNDERGRADUATE SCHOOLS ATTENDED:

University of Oregon, Eugene, OR  
University of Washington, Seattle, WA

### DEGREES AWARDED:

Doctor of Philosophy in Physics, 2020, University of Oregon  
B.S. in Physics, 2012, University of Washington

### PROFESSIONAL EXPERIENCE:

Graduate Research Fellow, Department of Physics, University of Oregon,  
Eugene OR, Summer 2015 - Spring 2016, Fall 2019, Spring 2020, Summer  
2020

Graduate Teaching Fellow, Department of Physics, University of Oregon,  
Eugene OR, Fall 2012 - Winter 2015, Fall 2016, Spring 2017 - Summer 2018,  
Summer 2019, Winter 2020

Science Literacy Program Education Mentor, University of Oregon, Eugene OR,  
AY 2018 - 2019

Science Literacy Program Fellow, University of Oregon, Eugene OR, Spring 2015  
and Winter 2017

### GRANTS, AWARDS AND HONORS:

Summer Institute on Scientific Teaching Education Fellow, Summer 2018

Weiser First Year Teaching Assistant Award from the UO Physics Department,  
Fall 2012- Spring 2013

## PUBLICATIONS:

Roe ET, Bies AJ, Montgomery RD, Watterson WJ, Parris B, Boydston CR, et al. (2020) Fractal solar panels: Optimizing aesthetic and electrical performances. PLoS ONE 15(3): e0229945. <https://doi.org/10.1371/journal.pone.0229945>

## ACKNOWLEDGEMENTS

I want to give thanks to my family, my Mom and my sister Shayna who helped me get this far. Their kind words and unconditional support have always meant the world to me.

I want to thank my partner Kaitlin who helped me get through the final hurdles of getting this degree. Her constant companionship, understanding, and support were and are what I needed to get through.

I want to express my sincere gratitude to my advisor Dean Livelybrooks, for the continuous support and advice he has given me over the last 8 years. I could not have gotten this far with out him.

I want to also express my sincere gratitude to Elly Vandegrift, who taught me the importance of equitable teaching practices, and had a large role in shaping my teaching style over the years.

I want to thank the rest of my committee Richard Taylor, James Imamura, and Doug Toomey for their feedback. I want to thank all of the professors I have taught with over the years, especially Dan Steck and Scott Fischer, they helped shape me into the educator that I am today.

I want to thank the GTFF, especially the disability access caucus, for their camaraderie and support over the years.

I want to thank all of the undergraduates who have worked in the Livelybrooks lab over the years. They helped me learn how to be a better educator as well.

Thanks to all of the other graduate students who have been there for me over the years, a thank you to Richard Wagner for giving me the LaTeX files and advice

I needed to finish this thesis, and thanks to Peter Lindstrom who helped the group get started in the beginning.

For my Dad.

Just like I promised.

## TABLE OF CONTENTS

Chapter	Page
I. INTRODUCTION . . . . .	1
1.1. The Role of Fluids in the Cascadian Subduction Zone . . . . .	6
1.2. MAGNETOTELLURICS . . . . .	14
1.3. ModEM 3D AND INVERSIONS . . . . .	20
1.4. THESIS OUTLINE . . . . .	25
II. MAGNETOTELLURIC INVESTIGATION OF CASCADIA . . . . .	26
2.1. Notable Results . . . . .	27
2.2. Discussion . . . . .	38
2.3. Summary . . . . .	47
III. IMPROVED INTERPOLATION ACROSS A CONDUCTIVE BOUNDARY FOR MOD3DEM . . . . .	49
3.1. Background . . . . .	51
3.2. Methods . . . . .	52
3.3. Results . . . . .	63
IV. MEETING THE CHALLENGE OF MAGNETOTELLURIC IMPEDANCE ‘PHASE TAILS’ . . . . .	69
4.1. Model Geometric and Associated Geological Settings . . . . .	77
4.2. Methods and Geological Constraints . . . . .	85
4.3. Results and Discussion . . . . .	106
4.4. Summary and Future Work . . . . .	110
V. REFLECTION . . . . .	112

Chapter	Page
APPENDIX: GLOSSERY OF TERMS . . . . .	114
REFERENCES CITED . . . . .	119



## LIST OF FIGURES

Figure	Page
1.1. Typical Subduction Zone . . . . .	2
1.2. MOCHA Survey and Other Cascadia MT Stations . . . . .	5
1.3. Fluid Metamorphically Stored in the Slab . . . . .	7
1.4. Metamorphic Phases Diagram . . . . .	10
1.5. Example of Resolution for MODEM3D . . . . .	15
1.6. Stations Used in Inversions of Cascadia. . . . .	16
1.7. Field Distribution on a Yee Grid Element . . . . .	22
2.1. MOCHA Conductances . . . . .	29
2.2. MOCHA Cross Sections . . . . .	30
2.3. Along Slab MOCHA Cross Section and ETS Correlation . . . . .	32
2.4. Conductance vs ETS Plot . . . . .	34
2.5. Isosurface Siletzia . . . . .	36
2.6. Cross Correlation . . . . .	41
2.7. Terrane Contrast . . . . .	43
3.1. Sea Land Interface . . . . .	50
3.2. Stair Step Bathymetry . . . . .	51
3.3. Planar Interface . . . . .	53
3.4. Shantsev Ratio . . . . .	64
3.5. ElectricField Plot . . . . .	66
3.6. Magnetic Field Plot . . . . .	67
4.1. MOCHA Phase Tail example . . . . .	70

Figure	Page
4.2. Starting Model Cross Section . . . . .	75
4.3. Phase Tail Site on a USGS Map . . . . .	76
4.4. Field Discontinuity . . . . .	79
4.5. Example of E field distribution around an L shaped conductor . . . . .	81
4.6. Unsmoothed MOCHA Model . . . . .	84
4.7. MC13 vs Model Site . . . . .	108

## LIST OF TABLES

Table	Page
3.1. Adapting ModEM3D . . . . .	54
4.1. Phase Tail Plot . . . . .	89

## CHAPTER I

### INTRODUCTION

The possibility of a devastating, large-scale earthquake threatens the human population living in the Pacific Northwest of North America within the Cascadia Subduction Zone. As shown in Figure 1.1, the Cascadian subduction zone is a spreading center, a region where new oceanic crust is formed, moves relatively landward, plows below (subducts) less dense continental crust, and eventually sinks deep enough to contribute to magmas forming volcanoes [1].

As the relative motion of the two involved tectonic plates is generally not continuous but, rather, episodic, Cascadia (Figure 1.2) is one of several subduction zones worldwide where large ‘megathrust’ earthquakes and consequent tsunamis occur. Another example is off northeastern Japan, site of the disastrous 2011 M9.0 Tohoku earthquake and accompanying tsunami. A large-scale megathrust event occurs when the two plates buckle and slip rapidly along their common interface, known as a thrust surface [1]. We will refer to the the area surrounding the points of contact between the subducting oceanic plate and the North American Plate as the *plate interface* through out this paper. During interseismic, quiescent periods they are prevented from slipping because the thrust surface is locked (the ‘locked zone’), see area A of Figure 1.1. That is not to say that nothing of note happens during quiescent periods, measurable deformation occurs, particularly in the overlying continental crust, and smaller-magnitude earthquakes accommodate localized stress buildup within either plate, among other things. If we can better understand the physicochemical processes occurring along the plate interface, from the locked zone (Area A 1.1) to mantle-wedge corner (MWC) (Area B of Figure 1.1) and even further down the plate interface (down-dip), we can better understand megathrust

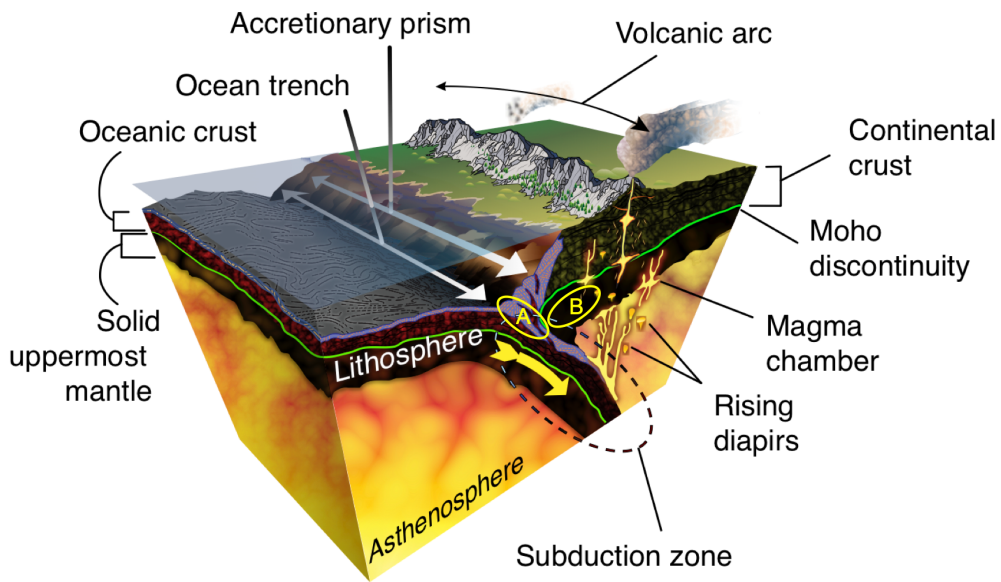


FIGURE 1.1. A typical subduction zone, though the subduction zone properly defined is indicated by a dashed oval here, we are defining the subduction zone to comprise the region from the offshore spreading center to the volcanic arc. Area A is the offshore locked zone, where the continental and oceanic plates are stuck together. Area B refers to the MWC, the area with nominally triangular cross-section constrained by the Moho and the subducting plate.

events. Geoscientists strive to develop frameworks for these physical and chemical processes congruent with a wide variety of observations, for example, variations of seismic activity within the leading edge of continental crust where it overrides a just-subducted oceanic plate (Figure 1.1). Subducted fluids, both in free form or held within pressure-/temperature-dependent metamorphic mineral phases, are thought to play important roles in many of these processes, for example mediating episodic tremor and slip (ETS) events occurring just above the mantle wedge corner [[2]; [3]]. Several important questions about how fluid concentrations and processes affect subduction zone phenomena can be explored by geophysical techniques, specifically magnetotellurics via the Magnetotelluric Observations of Cascadia using a Huge Array (MOCHA) experiment, potentially illuminating this geohazardous region. This chapter will pose a subset of these questions that will be revisited and discussed in further chapters of this dissertation.

A particular useful geophysical tool in the study of fluids, magnetotellurics, uses electromagnetic waves generated within the Earth's ionosphere and by thunderstorms as probes in order to generate conductivity maps in three dimensions [4]. Resulting 3-D models require pictures of cross sections or slices along a line of latitude to show us what is underground. These maps allow for the visualization of fluid concentrations, typically within sedimentary or fractured metamorphic rocks, and other conductive geological features that can be correlated with known geological processes related to the plate interface. To make these maps, data simulated using 3D computational models for gridded electrical conductivity, are compared to actual observations made by magnetometers and electric dipole sensors strategically placed in areas of geological interest. These sensors detect low frequency radio waves entering the Earth and exciting currents within that, in turn, will serve as sources of

secondary electric fields that are also detected using these sensors. We can use these signals to calculate a frequency-dependent electrical resistance called an impedance. This set of impedances tells us what is conductive and what is not. Each frequency sounds to some effective depth, due to the electromagnetic skin depth effect, the longer the wavelength of a wave the deeper it can penetrate the earth, so having a wide range of frequencies means we gain knowledge of a wide range of depths from our data. Using a collection of observed impedances at various frequencies, our data, we can use an iterative finite difference modeling technique, called an inversion, to generate our models.

To study the Cascadian interplate interface we placed sensors both on land and at sea across a large section of the Cascadia subduction zone during the MOCHA experiment, Figure 1.2. MOCHA, one of the world's first 'amphibious 3-D' surveys, began with the acquisition of 173 stations, 102 onshore stations and 71 offshore stations, from a large, nominally rectangular array of stations spaced and average of 25 kilometers apart. The array provided amphibious data useful for imaging subducted fluids from trench to mantle wedge corner (MWC). We encountered problems when using a popular, finite-difference inversion package, ModEM 3D ([5]), particularly with sea floor stations. This inversion package iterates smoothed models until data statistically matches observations, while interpolating fields across extreme changes in conductivity, such as those found on the sea floor is currently problematic. These problems arise due to the strong, nearby conductivity gradients, as well as stations exhibiting strong phase anomalies. This dissertation describes: the work done inverting the MOCHA data set and its implications for understanding roles played by fluids within the Cascadia Subduction Zone; details about efforts to improve modeling of amphibious data using the ModEM 3D software, and; details

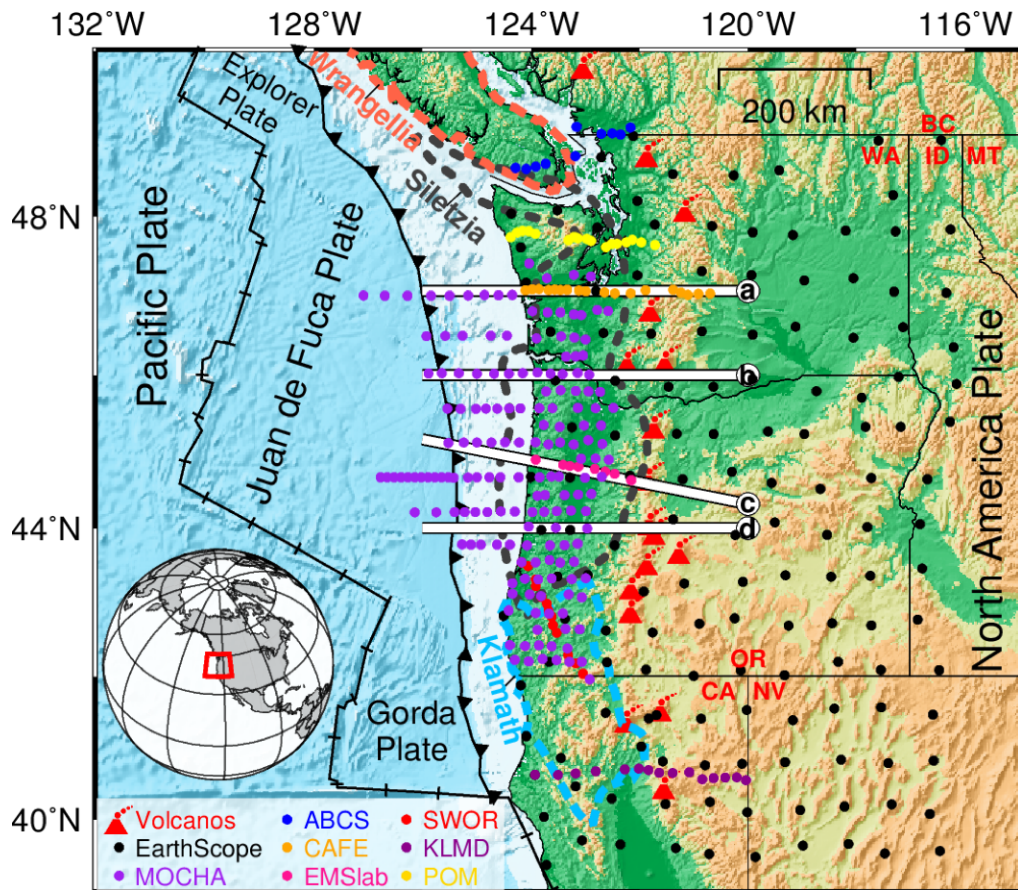


FIGURE 1.2. Stations used in inversions of Cascadia. Line a, b, c, and d refer to cross section depicted in Figure 2.2 shown in Chapter II. The dotted lines indicate the three distinct geological terranes in the region, Wrangellia, Siletzia, and Klamath.



about, explanations for, and potential solutions to the problem of observations exhibiting anomalous, out-of-quadrant phase rollout ('phase tails') in MT data. The remainder of Chapter 1 introduces important background on, magnetotellurics, inversions, ModEM 3D, the geological processes related to the presence of fluids along the Cascadian plate interface, and anomalous phase tail behavior, referenced throughout the rest of this work. This chapter concludes with an outline of the rest of this dissertation.

## **1.1 The Role of Fluids in the Cascadian Subduction Zone**

Fluids play a critical role in geological processes happening along the entire plate interface of the Cascadian subduction zone, starting at the trench, then along the accretionary wedge, and extending past the mantle wedge corner, and beyond to flux the melting of mantle material fueling magma production. The full extent of the effect of fluids in this region is unknown, however key questions persist that can be addressed through comparisons between the presence of conductivity concentrations, or the lack thereof, and the location of key geological process. This thesis explores four of these questions that fall under the purview of the MOCHA study.

We will frame this description of free fluid availability, sequestration and release as within an upper slab and the overlying crust ('the interface') as the slab descends to greater depths and, thus, higher temperature and pressure regimes. We begin by examining the zone between the spreading centers and the trench. Here water first enters the slab through fractures in the sedimentary layer of the oceanic plate, pulled in during hydrothermal circulation; this fluid also circulates in the shallow basalt layer of the oceanic crust [7]. Next, at the trench, where the Juan De Fuca oceanic plate first subducts beneath the North American continental plate, area A in

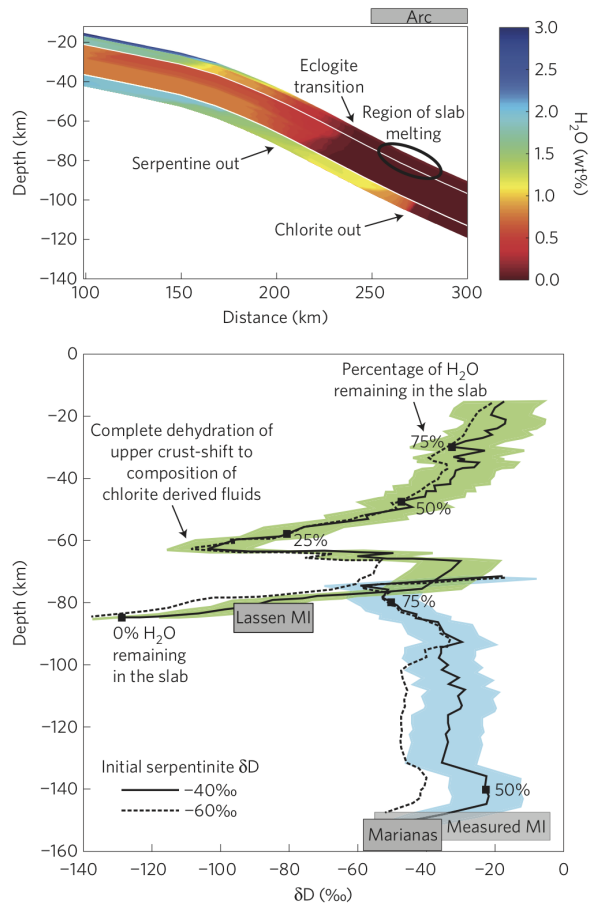


FIGURE 1.3. Diagram from Walowski et al. [6] depicting in the top Figure the percentage, with a 15% error margin, of  $H_2O$  per weight present in the subducting slab per depth. In the bottom Figure the percentage of water left in the slab is displayed, the green zone is for Cascadia which is relevant for this paper. The x-axis is hydrogen isotope percentage, it depicts the percentage of hydrogen in the fluid that is the isotope deuterium, the values are negative because they are calculated in reference to the standard defined Deuterium percentage.

Figure 1.1, sea water become trapped in the subducting plate by flowing into fracture zones around normal faults as they persist into the trench [7]. As the plate subducts it carries wet ocean sediments with it, introducing more fluid into the system. The degree of fluid sequestration through this process is a function of the development and structural characteristics of the sedimentary accretionary prism. Once the fluid hydrologically connects to the upper slab, including the uppermost basalt layer, and the plate subducts further into the trench, the fluid undertakes hydration reactions, such as serpentinization. These hydration reactions store the water metamorphically within clusters of metamorphic rock types known as mineral facies [8]. Traveling farther down-dip with the slab, fluids persist within these metamorphic facies, past the trench and into the area known as the locked zone. This is where the accretionary wedge, the most distal forearc feature of the North American plate in direct contact with the slab, is locked against the subducting plate owing to frictional forces. The two plates become locked causing this accretionary wedge to begin to buckle upward as the oceanic plate continues to subduct. Further hydration metamorphism happens in this region, involving clays leading to greenschist facies, representing a substantial amount of bound fluid present in the slab, around 2% per weight stored metamorphically in the upper slab [9]. These facies are thought to affect the thickness and density of the plate [10]. The consolidation and thickness of the subducting sediment layer atop the oceanic plate here, under the accretionary wedge, is thought to control how much the North American Plate deforms as the oceanic plate subducts below [11]. A significant amount of fluid, about 2-3 % per weight stays stored in pores in the upper slab through a process known as fluid pore compacture [9]. Traveling deeper down-dip along the subducting slab we reach the area known as the forarc Mantle Wedge Corner (MWC), Area B in Figure 1.1, this area is

where the subducting oceanic plate meets the Mohorovic Discontinuity (Moho), the seismically-defined boundary surface between the continental crust and the mantle. This region is significant because the specific make up of metamorphic facies in the mantle and lower crust along the MWC have density and porosity properties that allow fluids, sourced from dewatering reactions down-dip along the slab, to collect here by preventing their egress away into the upper crust [12]. These dewatering reactions occur under favorable pressure and temperature conditions, for Cascadia this occurs at depths between roughly 30-60 km depending on the reaction as shown in Figure 1.3. At depths of 60 km (Figure 1.3) only around  $25\% \pm 15\%$  of fluids originally retained in hydrous metamorphic assemblages remain within the slab [6]. Metamorphic dewatering increases the porosity of the resultant metamorphic facies, allowing the teacups worth (100 ml) of water released by them to more easily migrate up-dip [12]. There the fluids are thought to collect in the lower crust, above the MWC.

Throughout the slab fluids, in either free form or captured within metamorphic facies, affect important geological processes throughout the plate interface. Furukawa et al. [3], suggests that pressure caused by the accumulated fluid or fracturing caused by fluid escaping through more permeable, through fractures caused during dewatering processes, metamorphic facies may be key to understanding an important geological phenomenon known as Episodic Tremor and Slip(ETS).

ETS events correspond with the occurrence of swarms of low-frequency tremor that occur every 11-22 months depending on location [13]. These events correspond with a small updip slip along the plate interface, releasing the same amount of energy as a magnitude 6 or 7 earthquake, but over the span of 10-14 days rather than the few minutes of a typical earthquake [14]. The danger and interest in these events

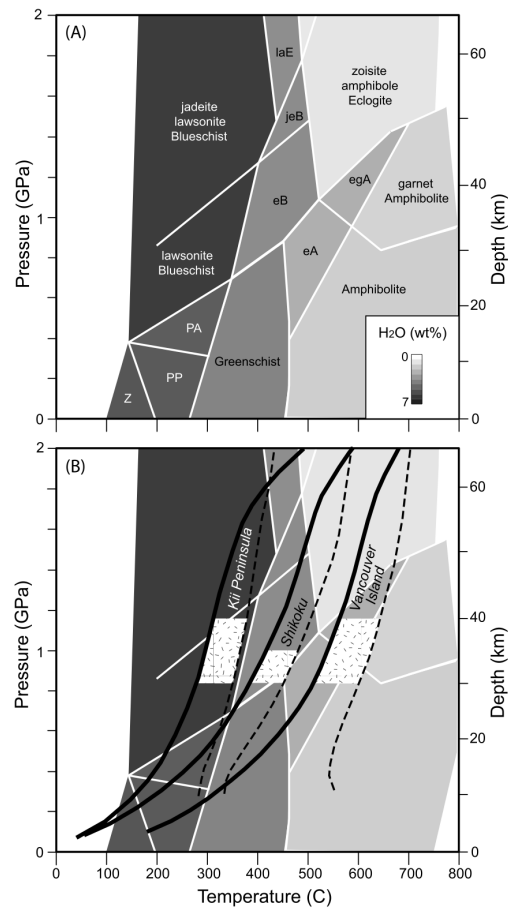


FIGURE 1.4. Taken from Peacock [12]. This diagram shows at what pressure and temperatures metamorphic phase transitions take place, the darkness indicates the maximum  $H_2O$  content present in the phases during each phase, transitions to a lighter color region indicate a dewatering reaction, introducing fluid into the system.

resides in the fact that they have been observed prior to large scale events [15]. The direct cause of ETS remains unknown but is thought to be related to the presence of fluids or to fractures caused by these fluids, sourced from dehydration reactions below the MWC [3]. We will use the term 'ETS occurrence' to signify the spatial density of tremor events occurring during a given ETS event for a given area of the crust. ETS occurrence has been observed to vary north to south along Cascadia [16]. We address key questions that relate to these observations of latitudinal variation:

- a) Are there any clear correlations between specific longitudinal fluid concentrations along the plate interface and spatio-temporal patterns of ETS occurrence, as you travel North South along Cascadia?
- b) If so, is the amount of fluid entering the slab near the trench or the amount of fluid released through dewatering reactions below or near the MWC more critical to ETS occurrence?
- c) Lastly, does ETS occurrence correlate more strongly with locations of fluid egress through deformation-caused fractures in a metamorphically altered crust, does it correspond more strongly with the location of pooled fluid above the MWC, or is the proximity between the two more important?

While episodic fluid egress through fractures and fluid pooling remain the main candidates for what causes ETS, the presence of fluids in the system does not always increase ETS occurrence. Fluid can flow through permeable zones found in serpentized lower crust within the overlying plate, and can serve to limit the build-up of fluid pressure [17]. This old metamorphic rock, created from the serpentinization of the accretionary wedge of the former Farallon Plate( [18]), can

provide egress to fluids escaping the slab interface through fracture zones [17]. This brings up alternative questions to address,

- d) Does migration of metamorphic, dewatered fluid away from the MWC through fracture zones in older, serpentized rock serve to reduce pore pressure buildup?
- e) If so, does an inverse-correlation between fluid flow and ETS exist?

If fluid escapes before it can collect along the MWC, the fluid pressure could be kept below whatever threshold may be required for ETS to occur. Additionally, in this scenario fluid could be present and flowing but never reach concentrations significant enough to observably-enhance electrical conductivity nor impact, within limits of detection, seismic  $v_p/v_s$  (p-wave velocity divided by s-wave velocity) ratios.

Another important feature of ETS that begs its own question, why do average ETS event intervals have a strong dependence on latitude? The Northern region of Cascadia, from Vancouver B.C through Washington state sees ETS events happening roughly every 14 months, the central region ,Oregon, experiences ETS events roughly every 2 years, while the southern region, Northern California, sees them roughly every 11 months [19].

- f) Why do these significant differences in ETS repetition rates occur, are there any correlations with the locations and amount of the fluid concentrated in these and the frequency of ETS occurrence?

The accretionary wedge of Cascadia is divided into several modified Terranes, remnants of old plates such as the Farallon [13]. Each terrane can be characterized, in part, by the location and type of accreted metasedimentary blocks present, as well as the strength and porosity of the overlying crust [19]. Oregon and Washington

both lie in the Siletzia terrane, a remnant of the old Farallon plate [20]. However, the segment of Siletzia comprising the Olympic Peninsula, and underlain by the Crescent formation, has a different composition and fundamental rheology than Oregon's Siletz terrane [19]. Fluid has more difficulty finding egress away from the interface through the overlying basalt layer of the Siletzia terrane in the North American Plate than the rest of the accretionary wedge. Schmalzle et al. [19] propose that the thicker yet more eastward concentration of Siletzian basalt in Washington, compared to Oregon could impose different fluid flow or pooling regimes in the two regions potentially accounting for difference in ETS occurrence between the regions. The development of fractures in lower crust metabasalts through episodic fluid flow could influence how strain develops near the plate interface [19]. More competent, less permeable basalt could also cause pooling that could apply strain to the plate interface via increased pressure [19]. Leading to another pair of testable questions:

- g)** does this proposed difference in fluid flow and pooling between these two distinct regions of Siletzia in Washington and Oregon correspond with a similar pattern of fluid concentration?
- h)** If a correlation does exist does the amount of detected channeled/concentrated fluid correlate with ETS occurrence?

In order to investigate any of the questions posed in this section we need a way to see the fluid concentrations through out the Cascadian subduction zone; the technique that we use to do this is called magnetotellurics.



## 1.2 MAGNETOTELLURICS

Magnetotellurics (MT hereafter) is an electromagnetic geophysical method used to develop models of the electrical conductivity structure of the Earth, which as we discussed in the previous section, varies substantially according to the presence of free fluids. This makes MT a good candidate for mapping the fluid content of structures. The MT study of primary interest to this thesis is the MOCHA Experiment, as such we will use it as a reference when needed. MT uses naturally-occurring electromagnetic (EM hereafter) fields, in the 'sub-radio frequency' regime, sourced by the Earth's ionosphere for frequencies ranging from .001 Hz to 1 Hz, and sourced by thunderstorms for frequencies higher than 1 Hz, to sound into the Earth [4]. Due to the distance between the Earth and the sources, these fields take the form of uniform, plane-polarized electromagnetic waves that impinge orthogonally upon the Earth's surface [4]. MT treats the Earth as an ohmic conductor [4]. EM fields employed by MT induce currents in the weakly-to-strongly conducting Earth and oceans, ranging from 10,000 to .01 ohm-m. A frequency-  $\omega$  and resistivity-  $\rho$  controlled skin depth relationship determines the depths of penetration, defined by equation 1.1 [21], with  $\mu$  defined as the magnetic permeability of the medium, which for the earth is typically the same as the value for vacuum. 1.2 describes a communally used approximation of the formula used in MT estimations.

$$\delta = \sqrt{\frac{2\rho}{\omega\mu}} \tag{1.1}$$

$$\delta = 0.5\sqrt{\rho T} \tag{1.2}$$

In short the skin depth is the exponential rate of decay of an EM-fields amplitude into an earth of uniform resistivity,  $\rho$ , for a field of angular frequency,  $\omega$  [21]. As such

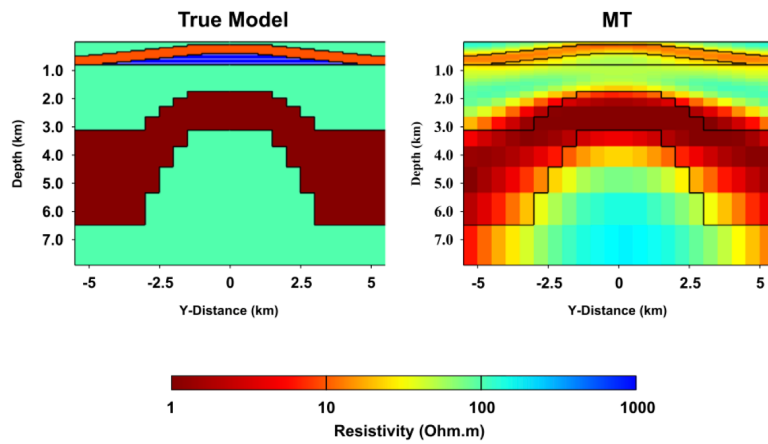


FIGURE 1.5. An example of the resolution of a synthetic model created by MODEM3D, note how the resistor directly under the top conductor is not imaged at all by MOD, demonstrating MT's ability to indentify the top of conductors more accurately than the top of resistive structures. [5].

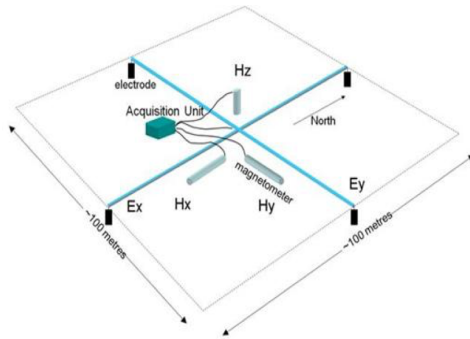


FIGURE 1.6. A common magnetotelluric site setup, this arrangement was used for the sites in the MOCHA experiment. X is the direction of strike

fields with a longer period inform us about a deeper part of the Earth. The skin depth effect acts as a primary control over a model's resolution, the waves that penetrate deepest into the earth will necessarily have longer wavelengths making it harder to resolve fine structure at depth [4]. Structures with smaller scale features than the skin depth of the penetrating wave will not be resolved as well, however MT is particularly good at differentiating the top of conductors from a resistive background [21]. Resolution depends heavily on location due to the skin depth's dependence on surrounding resistivity [21]. Figure 1.5 from Kelbert et al. [5] demonstrates the resolution of a synthetic model run through the ModEM3D Inversion software. I want to bring specific attention to the fact that the tops of the conductor are resolved accurately but the bodies of the conductors are smoothed out, additionally the depth to the center of conductance of conductive features can be inaccurate, as the shapes can be smeared out. MT has trouble pinpointing when conductors terminate at depth, but it can tell the conductance, conductivity-thickness product, of a structure accurately [21]. Further, testing can be undertaken where chosen features in a model are constrained to specific depths to determine what structural constraints fit the data most accurately.

MT measurement entails acquiring time series of 5 components of the EM-fields representing some combination of source fields propagating downwards and secondary fields arising from currents induced within the Earth. Signals, arising from an orthogonal array of electrodes placed to form two dipoles to measure the horizontal components of electric-(E) field and a 3-component fluxgate magnetometer, as in Figure 1.6, record voltages and magnetic field data. We estimate the electric field by dividing a voltage detected between two earth-contacting electrodes by the distance between the two electrodes. Each MOCHA station was occupied for 2-5 weeks in order to process periods from 1 to 10,000 seconds [22]. The incoming waves and the waves induced or reflected by the conductive structure of the earth cannot be directly distinguished from one another by the equipment. We get around this by assuming that the source fields naturally occur in many different random polarizations, but EM-waves will be polarized by the structure of the earth into specific polarization modes [21]. If we record data for a long enough period of time the random polarizations of the incoming waves will average out, leaving the waves that are polarized by the Earth [21]. Additionally the way the impedance itself is defined, as the E-fields divided by the source H fields, help differentiate the source fields from those induced within the Earth [21]. The Transverse Magnetic TM mode, where the magnetic field points parallel to the direction of strike and the Transverse Electric TE mode where the electric field propagates parallel to strike serve as the two primary polarization modes polarized by the Earth used in MT. We define strike as the direction of least conductive variance, it is the trend of the largest conductive structures, for example the coastline bordering extremely conductive ocean water. The Earth will naturally polarize reflected and induced EM waves along or orthogonal to the direction of strike [4]. This dissertation, keeping with common MT notation,

uses a Cartesian coordinate system where the x-direction is oriented along strike, and defines the direction going down into the earth as the positive z direction.

The raw data is stored as a set of time series, voltages and magnetic field data taken across different date ranges for each site, but all at a common sampling frequency. We then Fourier transform them into the frequency domain, into complex-valued earth response functions, the complex impedance tensor  $Z$ , the complex tipper function  $T$ . The complex-valued errors for impedances and tippers is estimated across evenly-distributed frequency bands [4]. The impedance is calculated for four modes including  $Z_{XY}$ , the TE mode defined as  $\frac{E_X}{H_Y}$ ,  $Z_{XX}$  defined as  $\frac{E_X}{H_X}$ ,  $Z_{YX}$  the TM mode defined as  $\frac{E_Y}{H_X}$ , and  $Z_{YY}$  defined as  $\frac{E_Y}{H_Y}$ , [21]. The complex Tipper function stores the z component's of the magnetic field in a similar notation dividing by the x and y components of the magnetic field to normalize for field magnitude,  $T_x$  defined as  $\frac{H_z}{H_x}$  and  $T_y$  defined as  $\frac{H_z}{H_y}$  [21]. We use the impedance to calculate the resistivity of the earth at various depths determined by the periods used, as in equation 1.3, where  $\omega$  is the angular frequency  $\frac{2\pi}{t}$ , t defined as the period [21]. A resistivity can be defined for every mode, often one mode can have worse quality data than the other. We use estimates of the error for each resistivity compared to mean values of the resistivity in the region to estimate quality, though this process can be complex [23]. Equation 1.3 defines the resistivity that you would expect to observe at a spot if you could physically measure it in situ, known as the apparent resistivity.

$$\rho = \frac{|Z|^2}{\omega\mu_0} \quad (1.3)$$

Additionally the impedance is characterized by a quantity known as the impedance phase, defined by equation 1.4 where i and j are indices for an x or y coordinate.

$$\phi_{ij} = \text{Tan}^{-1}\left(\frac{\text{imaginary}\left(\frac{E_i}{H_j}\right)}{\text{real}\left(\frac{E_i}{H_j}\right)}\right) \quad (1.4)$$

The impedance phase, defined simply as phase for the rest of this work, is a property of each mode that defines the phase shift between the electric and magnetic fields in that mode [21]. The phase is sensitive to sounding through transitions from areas of higher to lower conductivity, or vice versa, and can normally be related directly to the slope of log-log plots of apparent resistivity versus period [21]. Normally the  $Z_{xy}$  phase ranges from 0 to 90 degrees, and the  $Z_{yx}$  phase is between -180 and -90, but is often ‘trapped’ into the first quadrant for visualization purposes. Generally higher phase means sounding into more conductive material. Many magnetotelluric surveys undertaken worldwide, including the ElectroMagnetic Sounding of the Lithosphere/Aesthenosphere Boundary(EMSLAB) array and the MOCHA Array, have observed anomalous behavior where phase rolls out of quadrant exceeding 90 degrees [24]. If the phase becomes anomalous owing to structural peculiarities, and not simply noise, important details about the structure present in a model might be lost. Chapter IV delves into my efforts to deal with this in greater detail [24].

We place MT stations as far away from potential EM noise sources like power lines, trains, and nearby cities as possible. With a technique known as remote referencing, we use nearby stations as reference points for each frequency, to reduce the effect of outside noise on the data using coherence testing [23], [25]. The EM wavelengths used in MT span wide distances, when spaced appropriately nearby stations will receive a signal from the same EM wave, but not see the same noise

signals [23]. Once gathered, we use the MT data to create conductivity models used to map the region using linearized, model-iterative inversion [21].

### 1.3 ModEM 3D AND INVERSIONS

Modeling magnetotelluric data relies on an iterative modeling technique called an inversion. Several different variants of the inversion method exist, depending on the computational 'forward' modeling method used, and the algorithm used to converge the multiple iterations to compute a final model, but the basic idea is the same [21]. An initial model is created using a preferred computational modeling technique, usually the finite element or finite difference modeling method. Currently finite difference works best for modeling data in 3 dimensions [23]. Historically, inversion was undertaken to create 2D models that fit the data acquired at stations placed approximately along lines. This scheme reflected the computational limits of the time, and assumed that the electrical conductivity of the Earth's crust is largely unvarying in a given, horizontal direction, the aforementioned 'strike' [21]. However this assumption is met only infrequently. For a given iteration of an inversion, forward-modeled 'responses' are then compared to the observed data and an RMS error is calculated to determine how well the model fits the data. This information about residuals is used by a chosen algorithm to change the boundary conditions and the values of the conductivities inside the chosen model for the next iteration [5]. The complexity of the Earth and the fact that the system is under-determined, meaning that there are more unknown model variables than data points, guarantees that there will always be multiple conductivity models that could fit a given set of modeled data, this is known as the non-uniqueness problem [26]. To get around the non-uniqueness problem magnetotelluric inversion makes the assumption of minimal

variation in conductivity structure across the boundaries of small areas, such as a rectilinear block, something that is commonly referred to as smoothness [26]. This dissertation focuses on the inversion software MODEM3D created by Gary Egbert, Naser Meqbel and Anna Kelbert; used to generate our models of Cascadia and in our efforts to improve the modeling of offshore and phase tail data. The rest of this discussion will discuss how MODEM3D operates and introduce some of the forward modeling complications we will address later on in this thesis. MODEM3D adapts the inversion strategies previously developed by Gary Egbert and Weerachai Siripunvaraporn for the WSINV3DMT inversion method ([27]), as such their works will be referenced along with the relevant MODEM3D papers when discussing how MODEM3D inverts data into models.

First we will delve into a typical iterative step of the MODEM3D inversion method. We construct the first section of the inversion process, known as a forward model, using a starting model defined by a large 3-D grid, with predefined boundary conditions and a given conductivity for each cell in the grid [28]. Using a staggered Yee grid, as depicted in Figure 1.7, 3 components for the electric(E) and magnetic(H) fields are calculated using Maxwells equations at all the edges and faces respectively of each block for each of the two source polarizations used [28], the TE ( $H_y$  source) and TM ( $H_x$  source) polarizations [29]. Having two polarizations dictates the calculation of two forward models, one for each polarization [29].The solutions for the fields located at the neighboring edges or faces(nodes) at each of the grid blocks are averaged together using standard weighting, coefficients determined by how far away the nodes are from the data site, to calculate modeled field values [28].

For each polarization, these values are used to find an impedance  $Z$  at the location of each site for each frequency using:  $Z = E/H$ , this process is here called



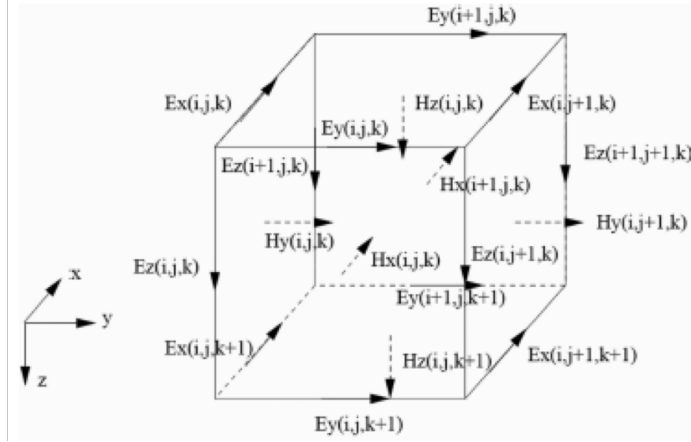


FIGURE 1.7. An example of a cell element in a staggered Yee grid, with Electric fields assigned to the center of grid edges and Magnetic fields assigned to the center of grid faces, taken from [5]. This is the grid used in ModEM3D.

interpolation [28]. Recall that for a given station each frequency corresponds to sounding to a different depth. For a given iterative step the interpolated model data is then compared to the actual data, to calculate a residual. The residual tells us how well modeled data fits the observed data. The method then uses the residual to redefine boundary conditions and conductivities for a new starting model [28]. This process is repeated until either a sufficiently low residual is calculated (these are normalized by the data variances), or the decrease in the residual after each forward model stalls, meaning that the decrease between residuals for sequential iterations becomes smaller than a predetermined amount [29]. What the inversion does next depends on the phase of the inversion process.

The MODEM3D inversion process undergoes 2 phases, due to the necessity of smoothing brought on by the non-uniqueness problem discussed previously. MODEM3D employs the OCCAM approach to smooth its models, developed by Constable et al. [26] for the OCCAM Inversion [5]. OCCAM systematically addresses the tradeoff between goals of reducing residuals versus ensuring smoothness

by introducing a 'tradeoff parameter,' essentially an iteration-adapted Lagrange Multiplier between model roughness and misfit [26] . All of this can be best characterized by describing a key component of MODEM3D, its own penalty functional shown in equation 1.5.

$$U(m, \lambda) = (m - m_0)^T C_m^{-1} (m - m_0) + \lambda^{-1} \{ (d - F(m))^T C_d^{-1} (d - F(m)) - X^{*2} \} \quad (1.5)$$

The first term on the right hand side of this equation describes the roughness term for the model. The OCCAM approach describes the roughness term as the sum of the square of the differences between modeled variables,  $m$ , in adjacent cells  $R = \sum_i (m_i - m_{i-1})^2$  [26]. In equation 1.5 the model covariance matrix term  $C_m$  serves the purpose of the sum here,  $m$  refers to an array of the modeled variables and  $m_0$  refers to the array of the previous iterations variables, or the initial starting values for the variables if this is the first iteration [5]. This roughness term describes how much variation there exists for a given variable between adjacent cells through out a model; the lower this value the smoother the model. MODEM3D uses  $m - m_0$ , the change in the array of variables  $m$  between neighboring iterations, instead of  $m$  alone because it aims to reduce the roughness introduced between each iteration of the inversion. The second term in equation 1.5, known as the sensitivity term, describes how well the model fits the data. The  $C_d^{-1}$  term is the data covariance matrix, it stores the information needed to calculate the RMS data misfit between the modeled data  $F(m)$  and the data  $d$ ,  $X^{*2}$  describes the target RMS data misfit for the model, and  $\lambda$  the Lagrange multiplier represents the trade off parameter between smoothness and model fit [29]. MOD3DEM's central goal is to minimize or, more accurately phrased, find the stationary point of this penalty functional and use that stationary point to update  $m$ , the starting parameters and boundary conditions

of the model, for the next iteration. The two phase approach previously mentioned constrains how MODEM3D can find the stationary point on each iteration. The first phase focuses on reducing the RMS data misfit below a predefined value  $X^{*2}$  using an initially predefined value for  $\lambda$ . If the decrease in RMS misfit between successive iterations fails to decrease below a predefined amount,  $\lambda$  will be reduced to prioritize fit and the next iteration will start [29]. Once the target  $X^{*2}$  is reached phase 2 will begin, this phase increases  $\lambda$  after each successive iteration to find the smoothest model possible that has an RMS misfit below the target value [29].

When there is a sea-land interface, this process is vulnerable to two problems that complicate things. First, an inaccurately-interpolated field can introduce errors, especially if the change in conductivity between two cell blocks is very large, such as at the seafloor. Secondly, since the model uses a finite difference technique, rectangular blocks are used to model the sea floor, approximating it as a kind of stair step structure; causing problems with the interpolation because it is estimating the fields using an inaccurate geometry. Since the sea is a large conductor itself, its presence and its bathymetry causes errors in the modeling technique. We are developing changes for the MODEM MT software to better model features at sea, and improve modeling of the air earth interface as well [5]. In Chapter 3 this dissertation will discuss how we implement these changes using an approach first introduced by Daniil V. Shantsev and Frank A. Maaø [30]. This interpolation approach involving a tilted planar interface will allow us to make more accurate models of regions including strong conductivity contrasts. By accounting for boundary condition constraints of fields using more accurate interpolation techniques.

## 1.4 THESIS OUTLINE

The layout of this dissertation is as follows. Chapter II describes the work done involving MT inversions of Cascadia and the geological insight we take from them about the role fluids play in Cascadia and its subduction zone. Chapter III describes the work done adapting the ModEM 3D software to interpolate ocean sites using a planar interface. Chapter IV discusses forward modeling work completed to determine the realistic geological structures behind the anomalous phase activity in the Cascadia region, with an aim to improve inversion accuracy. Lastly, Chapter V ties everything together and draws conclusions for our work and briefly lays out a path forward for future investigation.

## CHAPTER II

### MAGNETOTELLURIC INVESTIGATION OF CASCADIA

This chapter dives into the MOCHA experiment and what inversion of MOCHA data supplemented with data from other MT arrays has revealed about the role that fluids play in Cascadia and its subduction zone. The MOCHA experiment is a collaborative research project, working with Gary Egbert and Adam Shultz at Oregon State University, Paul Bedrosian at the United States Geological Survey, Kerry Key at the University of California San Diego SCRIPPs, and Bo Yang at Wuhan University in China. This study uses data from 393 long-period MT sites (Figure 1.2) to image the fluid concentrations in the crust and subducting slab, in hopes of addressing the questions about Cascadia brought up in section 1.1 of this dissertation. The MOCHA Array itself consists of 71 offshore sites extending from the trench to the coast and 102 onshore sites extending from Northern Washington through Oregon down to the California border. We augmented the experiment with 6 preexisting surveys: The Alberta-British Columbia South survey (ABC-S) [31], Cascadia Array for Earthscope Magnetotelluric Data Set (CAFE) [32], ElectroMagnetic Sounding of the Lithosphere-Aesthenosphere Boundary (EMSLAB) [[33]; [34]], Klamath Modoc Survey (KLMD) [35], Puget Sound and Olympic Mountains Transect (POM) [36], Southwest Oregon Survey (SWORMT) [37] and 144 Earthscope sites [38] to improve the experiment's extent and density of coverage. This chapter will focus on the region between central western Washington and western Oregon where we have the highest data density. Analysis of inversions of this large data set that map electrical conductivity have demonstrated the important role that the lithology of the overlying crust plays in fluid transport, especially with regards to latitudinal variations in fluid flow. This chapter will present the results of an inversion of this data set using the MOD3DEM

inversion software discussed in section 1.3. It will then discuss what those results imply for the tectonics of the region, with focus given to the questions raised in section 1.1.

## 2.1 Notable Results

The preferred MT inversion with results analyzed here concluded iterations with an RMS misfit between simulated and observed data of 2.6. My best inversion and Bo Yang's both achieved an RMS error of 2.6. The models are non-unique, as discussed in section 1.3, many inversions can have the same RMS error. However, smoothed models that are more geologically satisfying can be arrived at through various constraints upon the inversion process [21]. The inversions undertaken independently by myself and collaborator Bo Yang shown here have achieved RMS errors of 2.6 and 2.8 respectively (Figure 2.1). Both of these have undergone constraint strategies to prioritize more geologically realistic models. A multi-run approach was undertaken, designed to constrain, first, the TE mode. The TE mode was given a 5% error floor and the rest of the data was given a 10% error floor, so that the TM mode would not overshadow the TE mode. The experience of others ([21]) is that the TE mode better resolves deep crustal conductors, leading to more geologically accurate results. Once this phase was completed it was used to constrain another run with a 5% error floor on all of the data. For this dissertation we have decided to use Bo Yang's inversion as the preferred inversion and basis for our analysis. Bo's inversion has access to more sites, and Yang has greater experience with inverting various regional data sets, including elsewhere in the world. Although I am using Yang's inversion here, all processing of these inversion results and their analysis are my own, with the

exception of Figure 2.2 and Figure 2.5 [currently Figure 2.2 is a cross section taken by Bo Yang, will be replaced with my own cross section].

We show four distinct cross sections, two of which Figure 2.2a at 47 and Figure 2.2c at 45, line up with the 2-D CAFE [32] and EMSLAB [[34]; [33]] profiles respectively. All sections are oriented east-west with the exception of EMSLAB. These cross sections supplement the older 2D models [35], by providing improved cross-latitudinal resolution, owing to a higher site density and the addition of the offshore sites. Our 3-D model gives a much more complete picture of the regions surrounding and including those initially modeled for CAFE, EMSLAB, and other previous MT experiments included in our inverted dataset. Before this model, all longitudinal variations in the conductivity features modeled were primarily speculation. Previous profiles had literal gaps in knowledge between the fixed latitude 2-D inversions. 2-D inversions assume that conductivity doesn't vary in the direction of strike, this can lead to inaccuracies in modeled conductivity values when used to invert data with 3-D characteristics [21]. For example, in Figure 2.3a, the fact that the conductor located between 47, near the CAFE profile, and 45, near the EMSLAB profile, extended through out the region between the two lines would have gone unnoticed without a 3-D inversion. This specific conductor is of particular importance to the 'phase tail' discussion in chapter IV.

Figure 2.3 a depicts the conductance determined from the conductivity thickness product integrated locally over 10 km from the top of the slab into the overlying crust. Conductance is more accurately resolved by MT than conductivity [21]. Additionally, a rough estimate of F, the amount of fluid sequestered in a region assuming steady state conditions and some interconnectivity, can be made using the definition of conductance(C)(eq. 2.1) in conjunction with eq. 2.2, which relies on the fact that

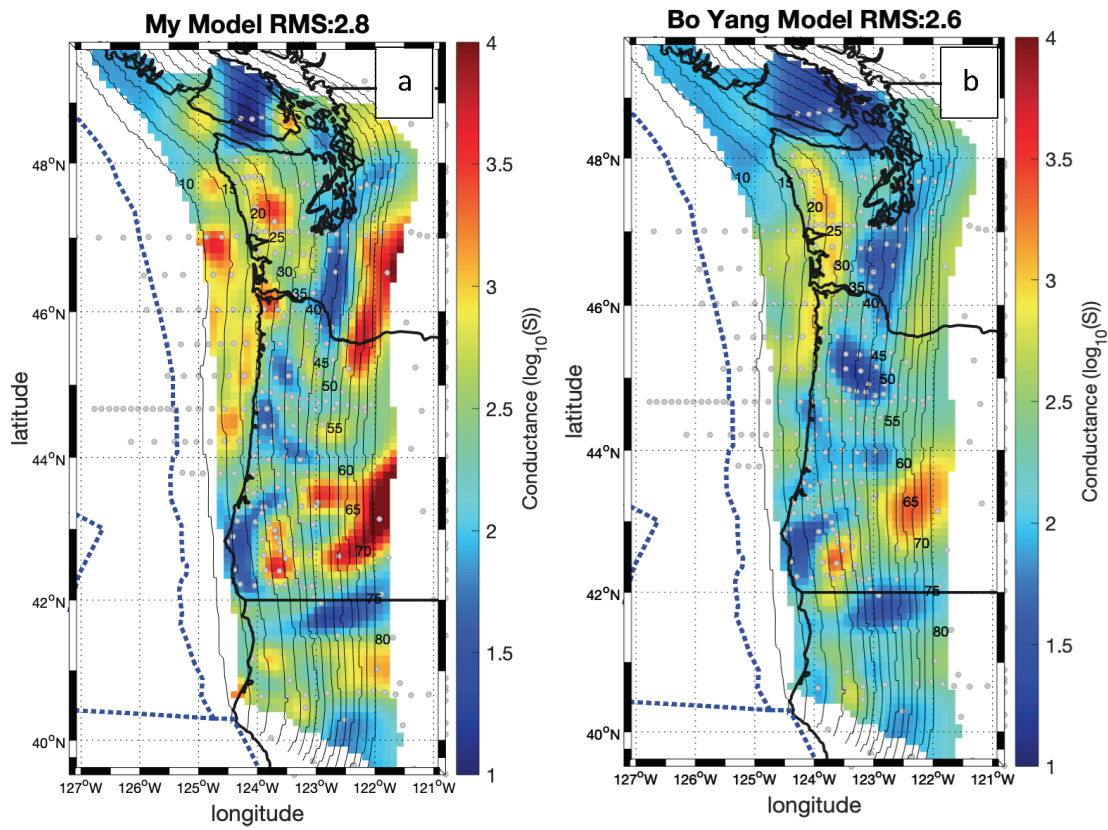


FIGURE 2.1. Above slab conductance profiles of two of the most promising inversions done of the Mocha data, a is my model and b uses Bo Yang’s model.



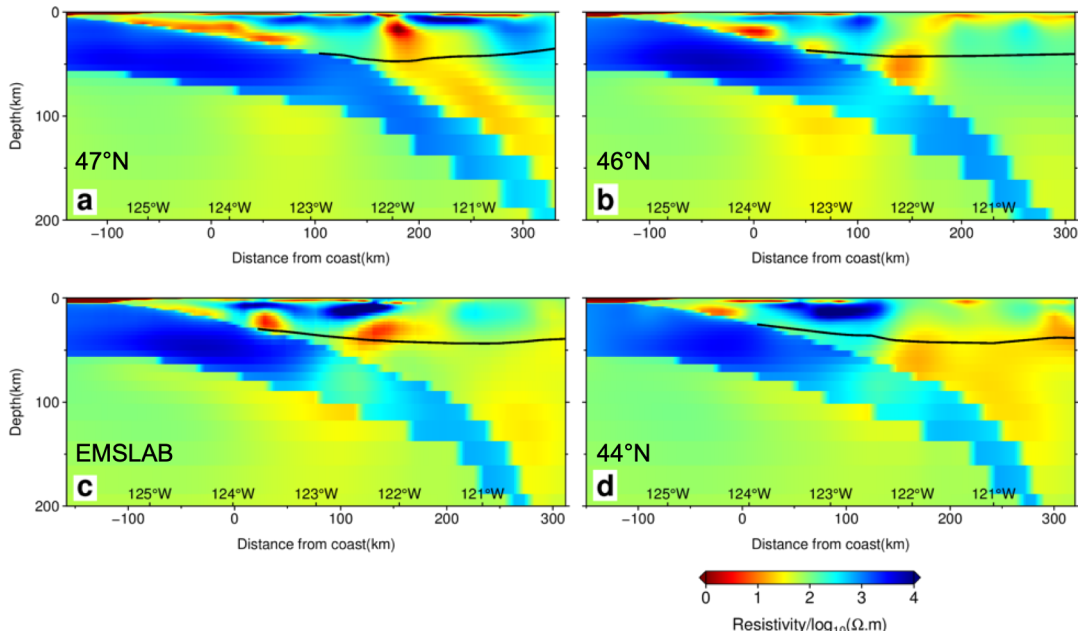


FIGURE 2.2. Cross sections taken from the preferred 3D MOCHA resistivity model of Cascadia. Each image refers to a line depicted in Figure 1.2 from Chapter I [22]. The black line references the location of the continental Moho, from [39], the location of the MWC is estimated in combination with the McCrory [40] slab data used to define the slab in the model. Line a and c were placed along the CAFE and EMSLAB profiles respectively, in order to compare this model to the previous work.

the amount of fluid in the region is proportional to  $\frac{\sigma_f}{\sigma_r}$ , where  $\sigma_r$  is the conductivity of the conductive region and  $\sigma_f$  is the conductivity of the sequestered fluid, following Archies law [41]. In eq. 2.1  $h$  is the length of the conductor(it's depth in this context) and  $\sigma$  is the conductivity. In eq. 2.2  $A$  is the area of the region taken in cross section, as in Figure 2.2,  $C_r$  is the conductance of the dry rock, and  $w$  is the width.

$$C = \sigma \times h \quad (2.1)$$

$$F \approx \frac{A \times \sigma_r}{\sigma_f} = \frac{w \times C_r}{\sigma_f} \quad (2.2)$$

Assuming the conductivity of the (saline) fluid stays relatively constant around  $3.33 \frac{S}{m}$ , and that steady state conditions are met, if the bulk conductance of the fluid holding rock is known, the amount of fluid present per length along strike can be roughly estimated. As normally assumed for MT models analyzed in previous research[35]), large conductance concentrations correlate with fluid released and impounded from dewatering reactions in the subducting plate. As discussed in section 1.1 these fluids could be present owing to fluids freely circulating within the shallow basalt layer of the oceanic crust, metamorphic dewatering, or from fluids trapped in the pores of sedimentary or metamorphic rocks. Figure 2.3a depicts three main zones of fluid concentration, not always present in every line of latitude, but found in many. The location of these concentrations can be more easily generalized by averaging the conductance along the contour lines of constant slab depth in Figure 2.3a, thus revealing the depth ranges with the highest conductance. This averaging distinguishes three distinct slab depths, roughly corresponding to three distinct concentrations of conductance.

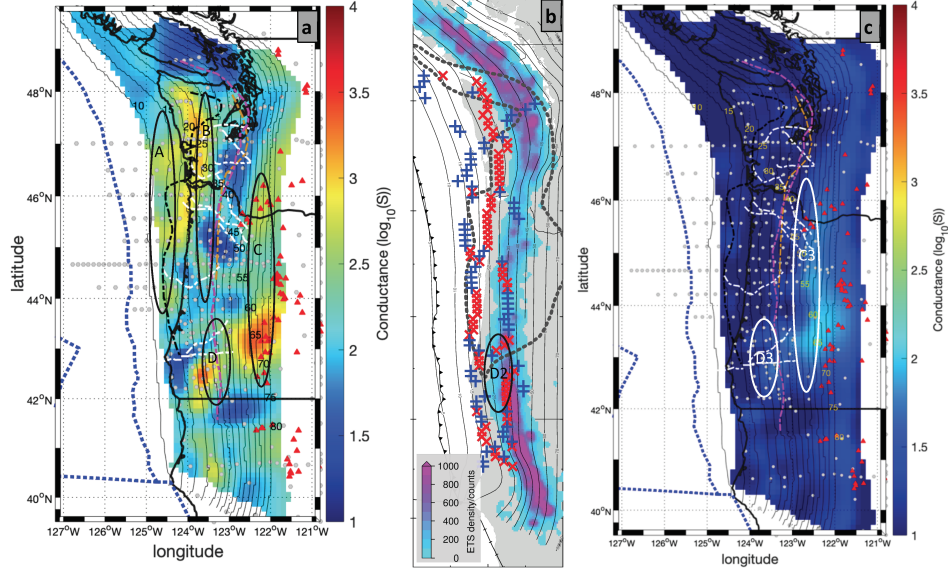


FIGURE 2.3. **a)** A conductance map along the subducting slab taken from the preferred 3D MOCHA resistivity model of Cascadia [22]. Thin lines depict depth contours to the estimated top of the subducting slab taken from [40]. Conductance here is defined as the conductivity thickness product, integrated over the 10km layer above the slab. The gray dots depict the location of MT stations and the red triangles depict the locations of volcanic centers along the arc. The dashed black line depicts the westernmost edge of the Siletzia Terrane determined by [42]. The dashed magenta line depicts the location of the MWC as defined by [43]. The dashed burnt orange line depicts an estimation of the MWC using a combination of the slab data from [40] and the Moho data from [39]. The dashed orange line estimation is the most similar to the MWC depicted in Figure 2.2. The exact details of the MWC in Figure 2.2 are necessarily imprecise owing to model gridding limitations and uncertainty restricted by both the resolution of the model grid and the increased uncertainty of the location of the Moho near the MWC [39]. Dashed white lines indicate the location of crustal fault lines from [44]. Black, open ovals outline four distinct regions of conductance concentrations, A-C centered along the three contour lines with the highest average conductance, D depicts the concentrations lying along the MWC south of 43.6° **b)** An ETS density map showing ETS-related tremor events that have occurred between 2009 and 2019 sourced by [45]. This map is overlaid by the two points of highest conductance in our preferred conductivity model, with red indicating the location of highest conductance. The dotted line indicates the boundary of the Siletzia Terrane. Oval D2 depicts oval D from a) here for reference. **c)** A conductance map similar to a), but with the conductivity product integrated over the 10 km below the slab top. White oval's C3 and D3 cover the same regions as C and D in a).

The first set of conductance concentrations are located offshore, ranging between the 10 km and 25 km contour lines, and centered at 17.5 km (Figure 2.3a circle A). This patch likely marks the accumulation of fluids resulting from sediment compaction of the shallow sediment layer atop the oceanic crust [46]. Fluid-filled pore collapse in the metabasalts of the oceanic plates subducting crust could also contribute to this fluid pulse [46].

The second patch of conductivity concentrations centers on the 30km depth contour line (Figure 2.3a circle B), roughly where Moho location data suggests the MWC is expected to be located, for south of 47.5 [39]. This conductor has a large amount of variability by latitude. These variations could be ascribed to variations in mechanisms leading to fluid concentration along the MWC. Figure 2.3a shows that north of approximately 46.3 the central conductance concentration stays near the average at 30km, but below 46.3 a weaker central conductance concentration sits east, around 40km depth. Further south around 44.8 the central concentration appears near its average depth of 30km once again. We attribute the southern part of this conductance concentration to fluid migrating up from metamorphic dewatering reactions further down dip [[3]; [12]]. Comparing the location of the conductivity peaks along the MWC in Figure 2.3a moving west from roughly 46.3 until returning east near 44.8, to the tremor occurrence plotted in Figure 2.3b at that same location shows correlations between those conductivity peaks and a reduction of tremor occurrence density. To better visualize the limits of this correlation Figure 2.4 depicts a plot of the average conductances versus latitude averaged over a 15 km depth range centered at the location of the contour lines of constant slab depth of 30km, and at the approximate depth of the MWC, 40km south of approximately 46.5 and 47km north of it. These conductance plots correspond to conductance

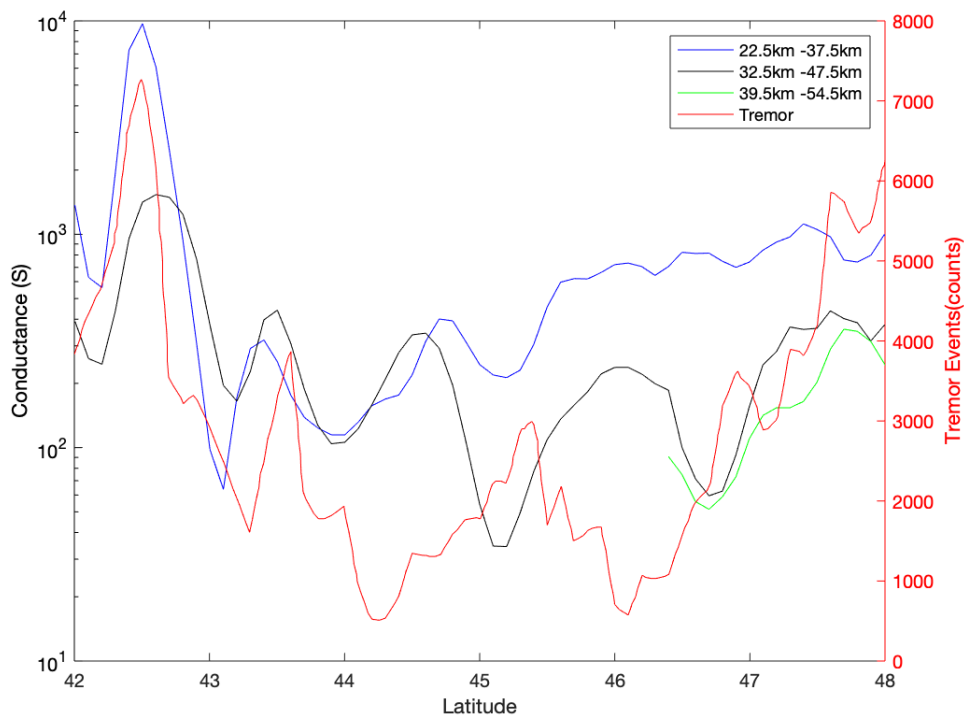


FIGURE 2.4. A plot of the conductance shown in Figure 2.3a as averaged across a 15km range of slab depths, for three depth ranges (blue, black, and green lines). The conductance along each of the contour lines from Figure 2.3a was averaged, the depth of one of the contour lines with highest conductance was used as the center depth for the 30 km line (solid blue line). The black and green lines use the contour lines that most closely align with the MWC lines from Figure 2.3a 40km (south of 46.5) and 47km (north of 46.5), as the center depths for the conductance averaging. The green line starts at the latitude where the MWC is thought to reach that depth. The red line is number of events versus latitude summed over bands of width 0.1 degree in longitude centered on the longitudes located in the middle of the event concentrations.

concentration B and the concentrations above the plotted MWC shown in Figure 2.3a. We plotted a red line depicting the number of tremor events for each latitude next to the conductance plots to determine any potential correlations. The shape of the 30 km conductance line more closely resembles the tremor line from 42 to 44, and then with a reduced similarity from 44 northward. This reinforces the idea that the northern and southern sections of this conductance concentration are caused by different mechanisms. The 40km and 47km centered average conductance lines lie along the two main depths that traces the MWC, the 40km line shows that conductance and tremor correlate from 42 to 43.6 and anti-correlate from 43.6 to roughly 47. These correlations requires further explanation in the next section, taking into account the location of the MWC with respect to its surrounding geology.

The third conductance concentration is not as strong as the other two. It is located around an area centered at a depth of 65km (Figure 2.3 a circle C). This conductance concentration lines up with the location of the volcanic arc and likely represents fluids released by metamorphic facies reactions contributing to volcanism [32].

Sections of conductance concentrations A and B from Figure 2.3a appear to lie along the westward border of Siletzia as defined by [42]. Figure 2.5a further emphasizes the correlation between the boundaries of Siletzia and some of the conductive structures seen in our model. The blue 300 ohm-m resistive structure fits within the defined boundary of Siletzia with an additional, southern block corresponding with the resistive core of the Klamath terrane. The conductors surrounding the iso-structure, especially the northern section of conductance concentration B from Figure 2.3, would then correspond with sedimentary and metasedimentary complexes accreted to to the leading edge of core Siletzia. These

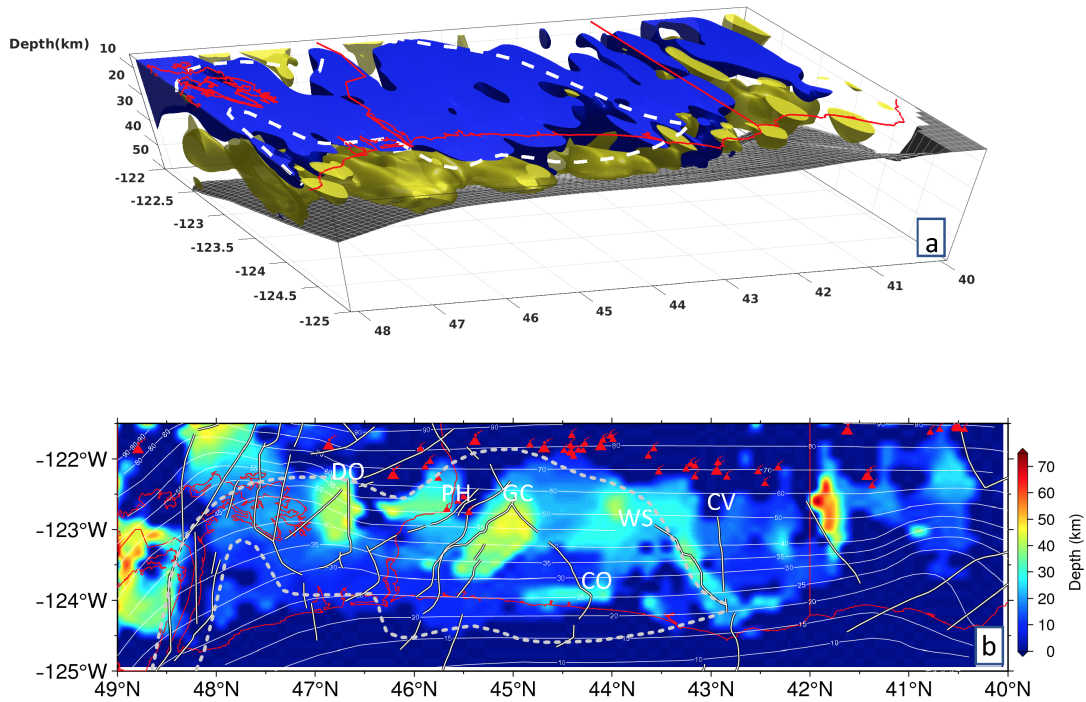


FIGURE 2.5. a) An isosurface plot created by Bo Yang of the model from Figure 2.3, showcasing a 3D view of the large scale conductive and resistive features in the model. A yellow 30 ohm-m iso-surface is displayed below a blue 300 ohm-m iso-surface. The white dashed line shows the boundary of Siletzia as defined by Wells et al. [42]. b) A plot showing the depth to the bottom of the resistive iso-surface displayed in part a. The small red triangles are volcanic vents, and the larger are arc volcanos. Crustal fault lines interpreted as penetrating the crust, as defined by Wells et al. [44] and shown in 2.3 are drawn in white. The Corvalis Fault (CO), the Canyonville Fault (CV), Wildlife Safari Fault (WS), the Gales Creek Fault (GC), Portland Hills Fault (PH), and the Doty Fault (DO) are labeled. The contour lines represent the depth of the slab as in 2.3.

accretionary complexes are likely remnants of an accretionary wedge, in this case a Farallon subduction zone remnant [18]. In our model a series of elongate, sub-coastal conductors step eastward near 46 in a pattern that matches a similar jog in the western boundary of Siletzia as defined by Wells et al. [42]. The correlation between these independently observed interpretations of Siletzia lends credence to Wells et al. [42]’s interpretation of the Siletzian boundary. This boundary is a property of the crust not the slab, suggesting that the crust and not the slab is controlling the conductivity structure of the interface zone. Intriguingly, our model shows variation in thickness across Siletzia (Figure 2.5b). The thinner areas see a greater concentration of fault lines, while the thicker, deeper-reaching blocks tend to be bordered by faults that Wells et al. [44] speculate as reaching through the overlaying crust to near the slab surface. Additionally the area of Siletzia near and north of 45 has more of these blocks that are 20 to 25 km thicker than the majority of the terrane. This region exhibits less volcanic activity than the region to the south between 45- 42, that has a generally thinner Siletzia terrane. There appears to be a correlation between terrane thickness and fluid flow down dip along the slab to the volcanic arc. Increased volcanic activity necessitates introducing more fluid into the mantle below the arc. This effect could potentially be attributed to the increase in crustal faulting caused by variations in Siletzia [44]. As shown in Figure 2.5b and Figure 2.3a, the increased presence of faults correlates to increased volcanic activity at the arc, these faults could play some role in channeling fluid towards the arc. Alternatively the correlation between terrain thickness and decreased volcanism may relate to differences in fluid channeling caused by variations in lithology(permeability, competence, etc.), potentially controlled by terrane thickness, across Siletzia [19]. As depicted in Figure 2.3c oval C3, there is a conductance concentration lying below the



mantle near the volcanic arc south of 46 where volcanism is enhanced, hinting at the presence of fluids. This also corresponds with a geological shift from stratovolcanos in the north, such as MT. Ranier, St. Helens, and Mt. Hood to volcanism in graben structures in the south such as MT. Jefferson and the Three Sisters.

## 2.2 Discussion

Here we discuss what the results from the MOCHA experiment imply for better understanding the tectonics of the region, focusing on questions from section 1.1. Three main items inspired by the previously discussed results present themselves:

- The implications of correlation and anti-correlation between ETS occurrence and the location of fluid concentrations along the mantle-wedge corner.
- Constraints on the extent of Siletzia, implied by conductance concentrations found in our model.
  - \* The role Siletzia’s thickness plays in fluid migration along the slab.
- The role played by ‘crustal faults’ within the subduction zone [44].

These items interlink in terms of how they affect the Cascade region but provide anchor points for this discussion.

As discussed in section 1.1 the increased pressure associated with the presence of fluids, sourced from dewatering reactions along the slab, and pooling at the MWC, so as to episodically open small fractures, is thought to cause ETS events [[3]; [12]] . With this explanation in mind we might expect to find high conductance concentrations near the MWC in regions showing high ETS occurrence. Figure 2.3a shows that such an obvious connection does not exist, except for conductance

concentrations located along the mantle wedge corner south of approximately 43.5. It is important to note that the two MWC lines in Figure 2.3a were both included because the exact location of the MWC in Cascadia is still under some debate. We determined the location of the orange line-depicted MWC by noting where the [40] slab data and the [39] Moho data intersect. The MWC from [43] is inferred from a velocity model with its own uncertainty, taken together the two lines give an estimate of the location of the MWC north of 43 . From approximately 43.6 to 43.3 (Figure 2.3a oval D) there lies a patch of high conductance along the MWC that lines up with a peak in ETS occurrence(Figure 2.3b). South of 43.3 the conductor gives way to an area of high resistance that spans to 43 that correlates with a reduction in ETS occurrence, south of this lies a conductor that extends past 42.2 that corresponds with another increase in ETS occurrence. Outside of between 42.2 and 47 our site coverage becomes less dense and the model less reliable as a result. This pattern of strong conductors correlating with increased ETS occurrence supports the Furukawa et al. [3] model, where slab-derived fluids below the MWC migrate to its uppermost boundary and serve as fluid reservoirs thought necessary for tremor production. Further, the same latitudinal span on Figure 2.4 shows a correlation between ETS occurrence and increased conductance averaged along the 40 km contour line. The conductance calculated for 2.4 was averaged over a 15km depth window; following Furukawa et al. [3] it is likely that fracture causing fluids escaping from the MWC contribute to the conductance concentration plotted here. For this region, then, there appears to be a correlation between strong conductance concentrations and increased ETS occurrence, answering that question from 1.1. However, an anticorrelation between ETS occurrence and conductance along the MWC exists north of 43.6 according to our model Figure 2.3. The 40 km slab

depth line depicted in figure 2.4, tracing an approximate MWC between 42 and 46.5 according to [43], shows that the correlation between ETS occurrence (tremor count) and conductance concentrations along the MWC changes from positive to negative near 43.6. A cross-correlation calculation, Figure 2.6a, between the tremor line and the 40km centered line in Figure 2.4 shows a positive correlation of 0.67, well above the blue confidence line, which shows the confidence bounds of the cross correlation. Figure 2.6b, which only contains the section of the 40 km conductance line north of 43.6N, in other words within Siltezia, shows a negative correlation of -0.33 below the confidence line.

Anticorrelation between conductance and ETS occurrence north of 46.3N suggests that a Furukawa-style mechanism, implying the development of significant and MT-detectable fluid concentrations along the MWC, is ruled out [3]. It is possible that the fluid is not pooling in the same way that it appears to be to the south of 43.6. Fluid fracturing could be the primary mechanism for ETS, through the consistent flow of over pressurized fluids through weak material such as talc, thought to be a product of serpentinization reactions involving silicon rich fluids released further down dip of the slab [16]. These fluids might ultimately egress through the metasediment channels imaged as oval A in Figure 2.3a. Though MT is sensitive to conductance, its resolution diminishes with depth [21]. If a layer along the slab interface that supports enhanced fluid volume percentage is sufficiently thin, it is likely not detectable using MT [21]. Whether or not we can image fluids in sufficient concentration as to raise conductance to be detectable by MT, we do image a correlation between areas with high conductance concentrations along the MWC and a reduction of ETS occurrence between 47 and 43.6 (Figure 2.3 and 2.4 ). These conductance concentrations, most notable between roughly 44.5 and

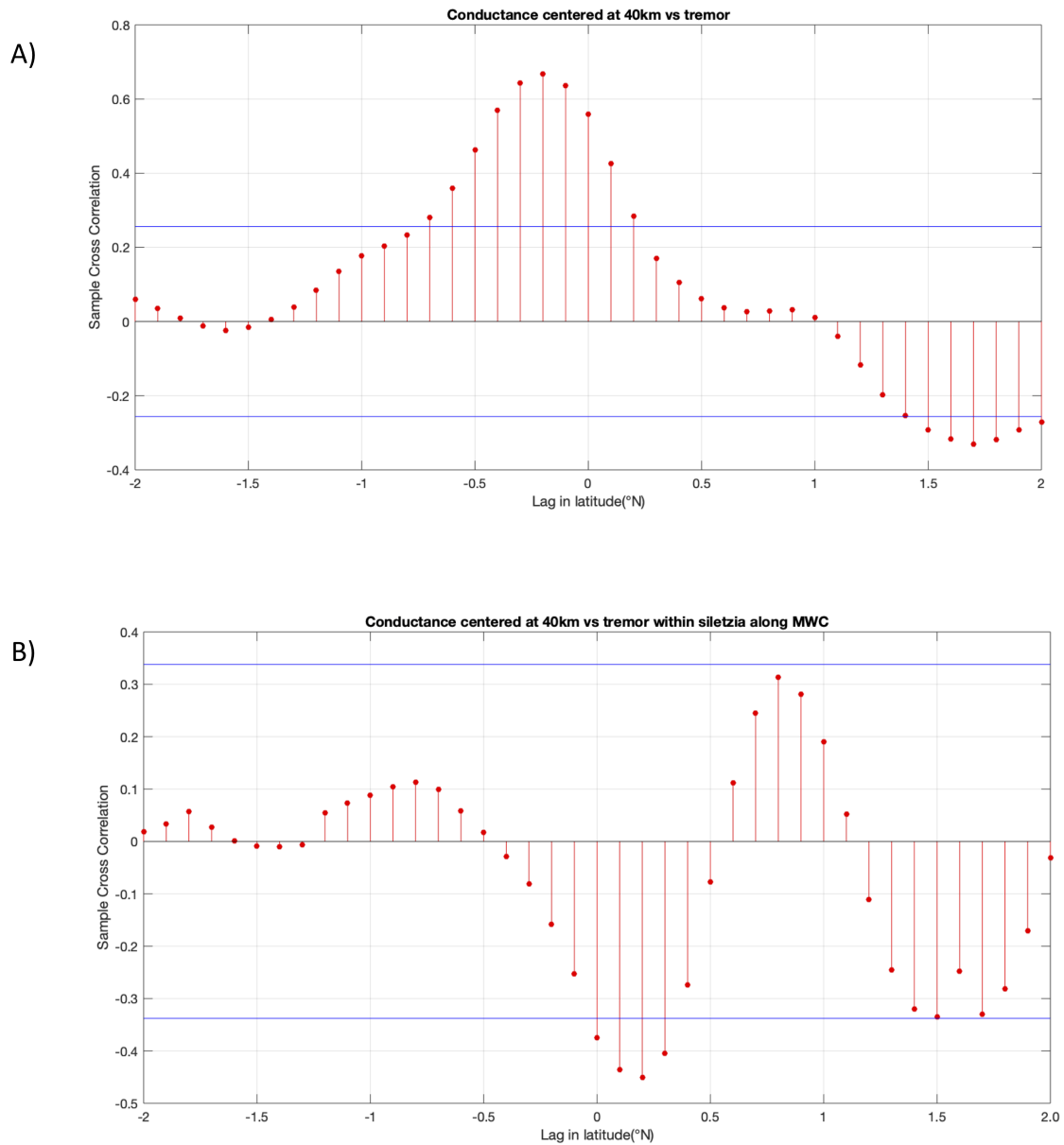


FIGURE 2.6. A) Cross correlation plot between the 40 km centered conductance line and tremor line in Figure 2.4. B) Cross correlation plot between 40 km centered conductance and tremor as in A, but only for the data located north of 43.6, putting it within Siletzia. The blue lines indicate the confidence bounds for each plot.

43.6 and between roughly 46.2 and 45.5, indicate the presence of collecting fluids. This correlation lines up with the thinking of [17] discussed in 1.1, one of our main questions in that section was whether we would find a correlation between fluid concentrations and reduced ETS occurrence. The area north of 43.6 lies within a portion of the Siletzia terrane comprising of, among other things, older, permeable, serpentized, metamorphic rock originating from the Farallon plates accretionary wedge [18]. As previously discussed this permeable rock would allow fluid to drain away from the MWC, leading to less fluid being available to cause pooling or fractures that could trigger ETS [17]. This possibly explains the observed decrease in ETS occurrence near these conductance concentrations.

Recall from section 1.1 that Siletzia is segmented and that the northern section, primarily located in Washington state north of 46.3 and known as the 'Crescent' terrane, has a different composition and rheology than the southern 'Siletz' section. Figure 2.7a depicts a modified version of a figure from [19], with the Crescent terrane highlighted by a star in the Olympic Peninsula profile. This part of Siletzia is thought to come from the sub-Farallon mantle, not its accretionary wedge [18]. [19] describes Siletzia as an impermeable cap, in the Crescent terrane this prevents fluid from flowing away from the plate interface before it reached accretionary complex. Figure 2.7 shows that the Crescent terrane is narrower in longitudinal extent but thicker in depth than the Siletz terrane to the south of 46.3. The northern part of Siletzia that includes the Crescent formation is marked by a resistive feature found north of 46.3 along the MWC in Figure 2.3a. This could explain why the [17] style anticorrelation between ETS occurrence and areas of high conductance does not hold farther north than 47 in our models. [17] require the presence of permeable structures, like brittle metamorphic rock for fluid egress, the impermeable Crescent terrane is devoid of

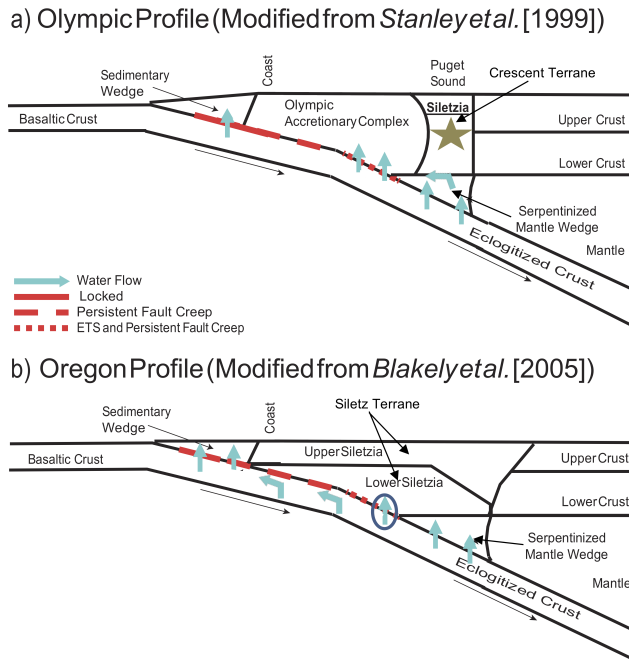


FIGURE 2.7. A modified version of figure 8 from Schmalzle *et al.* [19]. Section a) shows a profile along the Olympic Peninsula. The star emphasizes the region of Siletzia located at this latitude known as the Crescent terrane, this Siletzia is more fractured than the Siletzia in Oregon. This terrane is narrow and thick, as opposed to the Siletz terrane to the south in b. Section b) shows a profile located in Oregon along the Willamette Valley. The circled blue arrow shows a variable amount of fluid that can enter lower Siletzia, depending on the location of along the Siletz Terrane. The amount of fluid that can egress into the crust will vary, based on the specific composition of lower Siletzia in a given region.

those features [19]. The resistive Siletzia north of 46.3 would prevent fluids from escaping the slab interface before entering the MWC. Siletzia is thought to be more fractured with depth [19]. Fractured Siletzia becomes more permeable with increased pressure, implying that fluid can more easily enter this section of Siletzia at greater depths, but can not leave the plate interface through the shallower sections of the terrane [19]. This allows for fluid egress to and along the slab interface through the Crescent terrane but not immediately away from it into the upper section of the crust [19]. Once the fluid has propagated past the Crescent terrane(Figure 2.7) it enters the accretionary complex. The accretionary complex is more permeable than Siletzia, allowing for the kind of fluid fracturing supported by [3], accounting for the increased ETS occurrence in this region(Figure 2.3b). This would suggest that the proximity of the MWC to the Accretionary Complex north 43.6 is important for the enhanced ETS occurrence there. The accretionary complex is located much close to the MWC in Olympic profile than the Oregon profile. When the fluid enters the accretionary complex near the Crescent terrane it is located deeper down than it would be in the Oregon profile. This fluid would be under more pressure, allowing for an increased likelihood of opening fractures that could influence ETS behavior [3].

The location of conductance concentrations calculated under the slab interface (Figure 2.3c oval C3) correlate with the region of reduced ETS occurrence between 46 and 44, with some extension to the south. This conductance concentration is located within the top of the slab where dewatering reactions occur and correlates with the section of the Cascadian arc with the most volcanic activity. This conductance concentration(Figure 2.3c oval C3) indicates that there is likely more fluid dewatering from the slab south of 46, than to the north of this. It's likely, then, that more fluids

find their way into the overlying mantle so as to 'flux' more mantle melting, leading to more magma production, and ergo more volcanism.

The change in how conductance concentrations corresponds to ETS occurrence on either side of approximately 43.6 correlates with an important boundary, the boundary between the Siletzia terrane and the Klamath terrane to the south, depicted in Figure 2.3b. This also corresponds with the second to most southern fault depicted in Figure 2.3a the Wildlife Safari Fault[44]. These terranes have different lithologies and general metamorphic make up, notably the resistive core of the Klamath terrane is generally thinner than that of Siletzia, as found south of 43.6 in Figure 2.5b. Differences in fluid flow between the two regions is expected, they have different lithologies near the MWC. Further exploration of variations within the Klamath Terrane would require the extension of MOCHA further into California, currently, coverage of the Klamath terrane is sparser.

As noted above, the composition, strength, and permeability of the Siletzia terrane play a key role in the location of conductance concentrations through out the model. Figure 2.3a oval A shows that the western most conductance concentrations located above the slab interface in our model gather around the western boundary of Siletzia. These zones of enhanced conductance map the locations of accretionary wedge fragments as imaged using seismic tomography [43]. This suggests that mapping the boundary surface between our conductive and resistive features(Figure 2.5) would provide constraints on the extent of Siletzia. Figure 2.5a shows that the 300 ohm-m iso-surface of our model fits the Siletzia boundaries as defined by [42] but continues through the southern border along the Wildlife Safari Fault. The model here(Figure 2.5b) shows a deep, narrow resistive feature, trending approximately NE-SW, and indicating the start of the Klamath Terrane. In addition the isosurface



is broken into blocks of various thickness, hinting at different crustal textures across Siletzia. Part of Siletzia consists of the remnants of the old Farallon subduction zone ([18]), the conductive patches along the MWC in Figure 2.3a are likely fragments of the old subduction zones accretionary wedge [18]. The southern boundary of Siletzia along the Wild Life Safari Fault lines up with a very thick resistive feature(Figure 2.5b) that appears directly above the plate interface Figure 2.3a. [47] states that the southern edge of Siletzia near the Klamath Terrane was once located along the trench where the Farallon Plate began subduction under the North American Plate, making it likely that this thick resistive feature is a remnant of that subducting Farallon lithosphere. Figure 2.5) depicts that the varying thickness of Siletzia helps describe the fluid flow through out the region. The distribution of various thickness's of lithosphere ultimately controls where fluid can move through out the crust [16]. To illustrate this further, crustal faults border these blocks of thick lithosphere [44], which serve to channel fluid through out the crust.

Conductance concentrations located between 48 and 43.6 fig (2.3a) along the MWC correlate with a reduction in ETS occurrence. Deep crustal faults that extend to the slab interface, lie adjacent to these conductance concentrations. The conductance concentration near 47.5 infringes upon the Doty Fault, 45 upon the Portland Hills Fault and the Gales Creek Fault, 44.5 upon the Corvallis Fault, 43 upon the Wildlife Safari Fault, and 42.5 upon the Canyonville Fault (Figure 2.3, Figure 2.5b) [44] . [44] shows that tremor density decreases in areas surrounding deep crustal faults, attributing this to fluid migrating away from the MWC toward these faults, and reducing the overall fluid pressure of the system. [44] emphasizes that this fluid channeling may not be directly related to ETS, but it could explain the extent of the conductance concentrations that we see adjacent to these faults.

Fluid escaping through more fractured, and thus permeable, serpentinized rock as previously discussed could move toward these faults instead of through the MWC, giving another possible explanation to the reduced ETS occurrence and conductance concentration correlation. Additionally these faults may only open when sufficient fluid is present and could seal up again due to quartz build up from sediment rich fluid (quartz sealing)[44]. Opening and resealing of the faults could contribute to the episodic nature of ETS by forcing fluids to flow towards the MWC when the faults are sealed. [48] shows that ETS events are dynamic phenomena, the locations of slow slip and tremor migrate systematically throughout the duration of the event, traveling along a NW-SE trajectory in Northern Washington and Vancouver Island. This migration of ETS related tremor through time could be related to changing fluid flow mechanics mediated by faults and the thick patches of serpentinized Siletzia represented in our model [49]. Figure 2.3c depicts the conductance concentration 10 km below the plate interface. The conductance concentrations in this plot (oval C3) correlate with increased arc volcanism and a thick patch of Siletzia imaged in Figure 2.5b.

### **2.3 Summary**

Our model notes a correlation between conductance concentrations and increased ETS occurrence south of 43.6 in the Klamath terrane that supports the idea that highly pressurized fluid and the fractures reopend by them can cause ETS events [[3]; [12]]. North of 43.6, in the Siletzia terrane, an anticorrelation exists where conductance concentrations correlate with a reduction in tremor. This supports the idea that fluids can drain from the plate interface through serpentinized material in the crust, reducing ETS occurrence [17]. The near-shore, modeled, conductance

concentrations line up with the border of Siletzia. The thinner regions of our modeled Siletzia line up with locations of crustal faults and decreased tremor, supporting the idea that fluid egress through the faults reduces ETS occurrence [44] .

## CHAPTER III

### IMPROVED INTERPOLATION ACROSS A CONDUCTIVE BOUNDARY FOR MOD3DEM

While using ModEM3D [5] to invert the MOCHA dataset discussed in chapter II, we encountered problems inverting, particularly, sea floor stations due to the strong, nearby conductivity gradients (Figure 3.1). These conductivity contrasts are an issue because of the continuity requirements in Maxwell's equations [30]. Maxwell's equations require that the components of the electric field tangent to a surface be continuous across a conductive boundary [50]. However, using the finite difference method utilized in ModEM3D requires field solutions based on a staggered, rectilinear Yee grid (Figure 1.7) and interpolation of the electric and magnetic fields for station locations interior to grid cells. Electric fields are interpolated using a tri-linear spline technique, where weights are determined for the eight nearest electrical field estimates, creating a kind of weighted average for the field [5]. The normal interpolation depends on the expansion of the electric and magnetic fields in the form of equation 3.1 and assumes a continuous derivative across the typically-tilted conductive boundary [30].

$$E_x(z) = E_x(z_0) + \frac{\partial E_x(z - z_0)}{\partial z} \quad (3.1)$$

The derivative of the electric field is not equal on either side of the sea/land interface for electric fields. This discontinuity introduces error into the interpolated fields near the ocean/land interface, the error is then propagated through out the model through successive iterations during the inversion process. As a work-around, we have found that denser, finer model grids and intermediary lower conductivity layers near

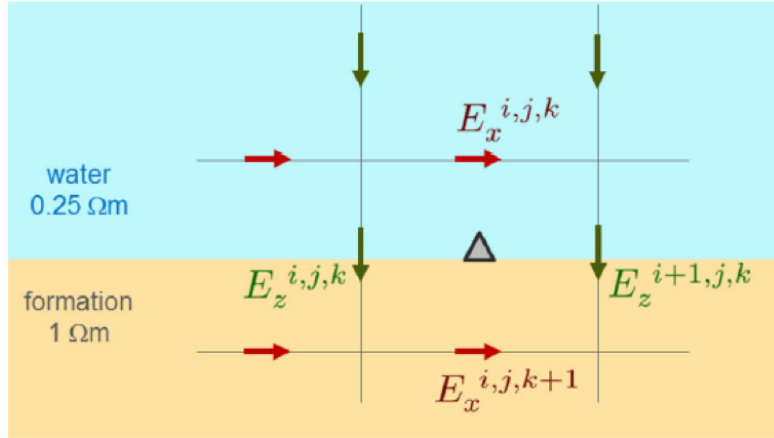


FIGURE 3.1. A cross section view taken from Shantsev and Mao [30] of the type of grid used in ModEM3D, demonstrating the conductive boundary between ocean and land cells. Electric fields are defined at nodes located at the cell edges. The fields at these nodes are then interpolated to the site location, indicated here as a grey-filled triangle.

the land-sea interface produce better inversions, as characterized by reduced data residuals. This is partly due to our ability to more accurately capture topography and bathymetry. This solution reduces the error, but it does not address the underlying problems.

A rectilinear grid, like that used in the finite difference method, can never fully model topography or bathymetry. A grid will always have a stair step like edge to it when trying to model a sloped surface (Figure 3.2). This introduces an inherent inaccuracy into the model and introduces more cell interfaces that have high conductivity gradients across them. We are experimenting with the joint addition of two improved interpolation schemes that more accurately track EM fields across cell boundaries, with an eye to enhancing the accuracy of the simulated responses and, thus, inversion results. This chapter explains the background of both of these interpolation strategies, the details behind them, and then discusses the results

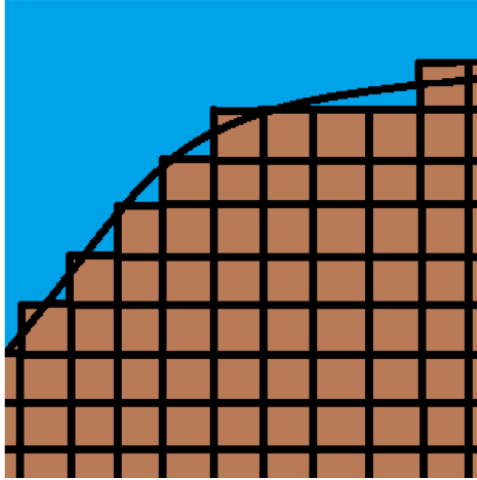


FIGURE 3.2. An illustration of an attempt to model bathymetry using a grid, such as that used in the finite difference method. A stair step like slope attempts to fit the sloped land sea interface.

of their implementation into the forward modeling kernel within the ModEM3D inversion package.

### 3.1 Background

The first scheme seeks to improve how fields are interpolated across a conductive boundary by adapting a strategy developed by Shantsev and Maaø ([30]). They introduce an extra interpolation term that corrects the discontinuity in the derivative of the electric field across the conductive boundary. We modify equation 3.1 to include a term (equation 3.2) that corresponds to this discontinuity. Using a combination of Maxwell’s equations and current conservation the discontinuity in the field derivatives between medium 1 and medium 2 is:

$$\frac{\partial E_{x2}}{\partial z} - \frac{\partial E_{x1}}{\partial z} = \left( \frac{1}{\sigma_{z2}} - \frac{1}{\sigma_{z1}} \right) \frac{\partial J_z}{\partial x} \quad (3.2)$$

where  $J_z$  is the current density normal to the interface, equal to  $E_z\sigma_z$ ,  $\sigma$  is the medium's conductivity, and numbers by coordinates/variables indicate the medium the coordinate/variable is referencing, this equation holds true for the x and y components of the E and H fields. This enhances the accuracy of the interpolated fields calculated by the forward solver.

In the second scheme, we introduce a new planar geometry capable of tracking sloping conductivity interfaces, determined by bathymetry or topography, and embedded within a normally rectilinear grid, and tested for now using a simplified Matlab version. This new geometry allows us to more accurately model large conductivity-contrasting boundaries such as the land-sea interface or the air-land interface. We rotate into a coordinate system defined by the local, tilted plane using the singular value decomposition (SVD). The interpolation is done in this system, using the plane to more accurately define where the conductivity boundaries occur. We then use a QR decomposition to create coefficients that are used to interpolate the fields from a Yee grid to a station on the new interface. Unlike the interpolation scheme this replaces, the new, QR-defined coefficients serve to interpolate using contributions from all 3 solution field components, to reflect the interpolation being across a tilted plane, to estimate a given components (say  $E_x$ ) at the cell-interior station location. Figure 3.3 shows an example of this planar interface intersecting a grid cell.

### 3.2 Methods

In order to incorporate the planar geometry and Shantsev and Maa's ([30]) interpolation terms, the simplified Matlab version of ModEM3D's forward model needed to be modified so that the new interpolation strategies could be implemented.

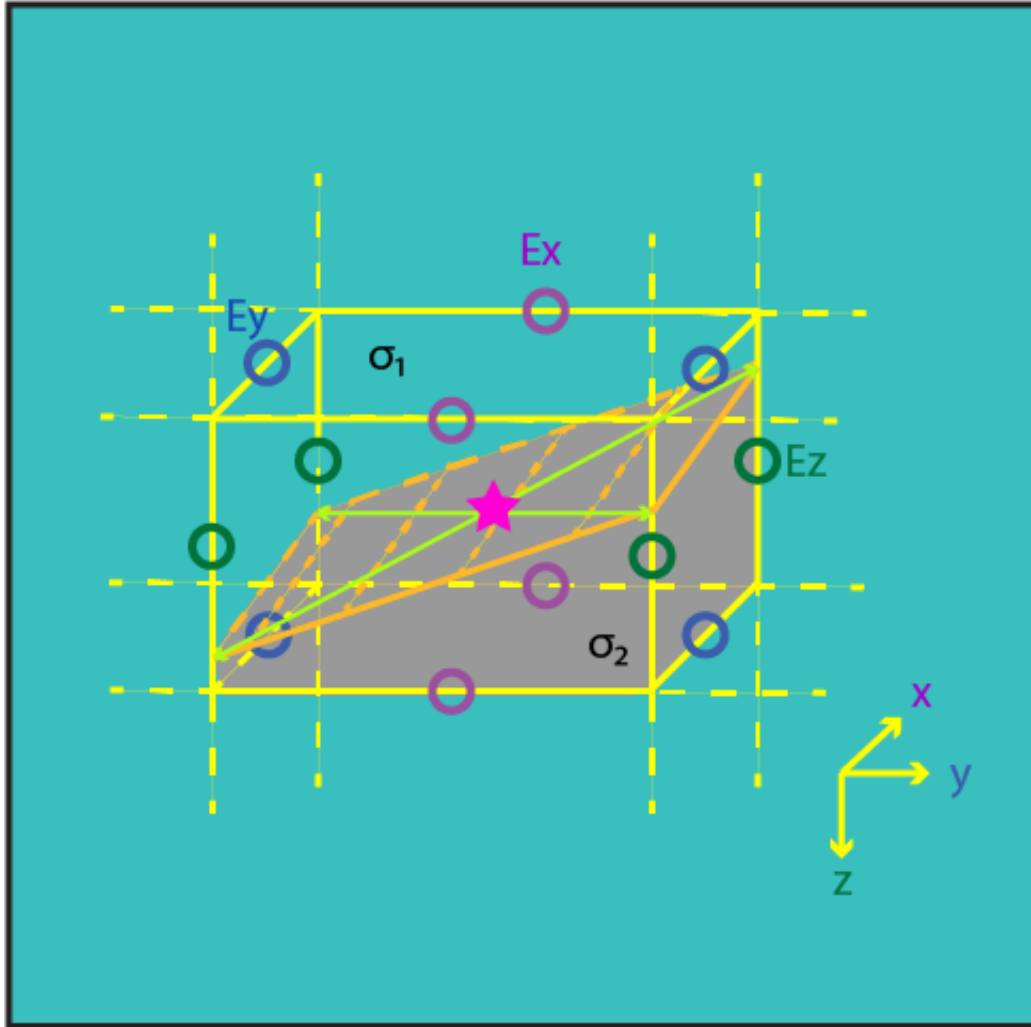


FIGURE 3.3. An illustration of the planar interpolation strategy used in this dissertation. The star references the station, known in this dissertation as  $x_d$  that the electric field will be interpolated to. The green lines dictate the process of interpolating the rotated field values from their respective nodes along the cell,  $x_k$  to the station. The EM field values are interpolated from their location nodes at the cell edge (the colored circles) across a planar boundary using a coordinate system defined by the inserted plane. The location of the field values need to be rotated into this new coordinate system and projected onto the plane, to where the plane intersects the cell edges.



Previously the code had only been used to calculate EM fields and needed to have data structures related to the inversion penalty functional(equation 1.5) added for troubleshooting purposes. Additionally several classes and subclasses underwent some redesign and had structures moved to three new classes: TDataFunc, TMTsite, and TPlane. Table 3.1 depicts the key classes involved in the process.

TABLE 3.1 A table displaying the key class's necessary in adapting our improved interpolation schemes to the simplified Matlab version of ModEM3D.

TABLE 3.1 Adapting ModEM3D

Class Name	Purpose	Key Modifications
<b>TVector3D</b>	<ul style="list-style-type: none"> <li>– This provides the basic vector structure for ordering and storing the solution electric fields.</li> <li>– Weights for interpolation of electric fields are defined here based on the 8 nearest cell edges (equation 3.3).</li> </ul>	Discontinuity term from Shantsev and Maa0 is integrated into the interpolation here (equation 3.2)

TABLE 3.1, continued

Class Name	Purpose	Key Modifications
<b>TMTsite</b>	<ul style="list-style-type: none"> <li>- This class takes the interpolated fields from TVector3D and puts them into a usable data structure.</li> </ul>	None
<b>TDataFunc</b>	<ul style="list-style-type: none"> <li>- Takes the fields from TMTsite and uses them to calculate the modeled impedance's for the station.</li> <li>- Uses the fields from TMTsite to calculate the penalty functional, equation 1.5</li> </ul>	<p>Takes the field structure from TMTsite and applies the rotation term derived from the SVD and QR decomposition undertaken in Tplane to introduce interpolation across a tilted planar conductive interface (Figure 3.3).</p>

TABLE 3.1, continued

Class Name	Purpose	Key Modifications
<b>TPlane</b>	<ul style="list-style-type: none"> <li data-bbox="597 474 1016 569">– Reads bathymetric data from file</li> <li data-bbox="597 632 1016 1119">– Calculates a Single Value Decomposition(SVD) using the bathymetry data to define a station-local coordinate system normal and within the bathymetrically-defined (often tilted) plane</li> <li data-bbox="597 1182 1016 1669">– Defines a designer matrix to calculate a QR decomposition using the location of field nodes rotated in the coordinate system of the plane to define new interpolation coefficients for the system.</li> </ul>	<ul style="list-style-type: none"> <li data-bbox="1101 827 1321 1314">– Created for the purpose of implementing the new planar interpolation scheme</li> </ul>

TABLE 3.1, continued

Class Name	Purpose	Key Modifications
<b>TPlane</b>	<ul style="list-style-type: none"> <li data-bbox="597 474 967 898">– The designer matrix includes the Shantsev and Maa0 discontinuity term, to preserve the inclusion of that interpolation strategy through the rotation.</li> <li data-bbox="597 953 967 1184">– Defines the new interpolation coefficients from that QR decomposition.</li> <li data-bbox="597 1239 967 1604">– Potential bugs in the software lie here, aligning the modeled plane with the test bathymetry. This is a complicated class.</li> </ul>	<ul style="list-style-type: none"> <li data-bbox="1101 793 1321 1276">– Created for the purpose of implementing the new planar interpolation scheme</li> </ul>

TABLE 3.1, continued

Class Name	Purpose	Key Modifications
<b>TSourceMT</b>	<ul style="list-style-type: none"> <li data-bbox="597 478 1016 701">– First data structure to be called, defines the two separate polarizations of the fields</li> <li data-bbox="597 764 1016 919">– Sets the initial boundary conditions for the forward model.</li> <li data-bbox="597 982 1016 1533">– When inversion functionality is fully introduced to this Matlab version of ModEM3D this is where the previous iteration’s penalty functional (equation 1.5) will influence the next forward model.</li> </ul>	None

The classes most important for the new interpolation adaptations are Tvector, TDatafunc, and Tplane. Tvector is where the Shantsev and Maaouf ([30]) discontinuity term (equation 3.2) is added to the preexisting interpolation weights. Interpolation in ModEM3D is done using a trilinear spline technique ([5]), where every node has its

own weighting coefficient defined by its distance from the station. This interpolation function is defined by equation 3.3 where each differently indexed  $c$  variable is a node dependent weighting coefficient and  $(x_0, y_0, z_0)$  defines the location of the station.

$$E_x(x_0, y_0, z_0) = \sum_i \sum_j \sum_k c_x(i)c_y(j)c_z(k)E_x^{i,j,k} \quad (3.3)$$

These coefficients govern the averaging used to project the field components to the location of the data site. The approximation from equation 3.1 is used to calculate the  $c_z$  coefficient across the conductive boundary. Adding equation 3.2 to equation 3.1 leads to more accurate estimations of the interpolated field.

The new planar interface interpolation strategy is primarily implemented in the newly created Tplane class. The first step requires us to define the bathymetry of the system, a data structure containing the bathymetry data is imported into Tplane. Tplane reads in a separate file with bathymetric and topographic information, locates cells in which stations lie, then determines the coordinates for those cell edges and midpoints. In doing so, it converts between surface coordinates expressed as latitudes, longitudes, depths into a simple Cartesian system. Tplane also determines the intersections between cell edges expressed in Cartesian coordinates and the topographic surface, and then assembles an array of the distances from each of the nearest grid/surface intersection points to the station (lime green lines in Figure 3.3), for each model dimension,  $x$ ,  $y$  and  $z$  defined as  $R$ . The components of  $R$  are multiplied by weighting coefficients:  $w_x, w_y$ , and  $w_z$  that are defined for the coordinates of each data point, built to go to 0 for points farther than a defined range from the station site, varying depending on the resolution of the model grid, and becoming 1 for coordinates within the same cell as the station. The weighting

coefficients take the form of equation 3.4, where the station's coordinate is  $x_d(i)$ , the observation point's coordinate is  $x_k(i)$ ,  $i$  is the given coordinate (e.g.,  $x, y, z$ ), and  $L$  is the distance between the farthest observation points for the given coordinate. The scaling by  $L$  for a given component ensures the weights are properly normalized.

$$1 - \frac{(|x_d(i) - x_k(i)|)}{L(i)} = w_i \quad (3.4)$$

Each weight is effectively 1 minus what percent of the maximum distance between observation points it falls. Since the observation points are on either side of the stations coordinates, the weights add up to 1. A station coordinate ( $x_d(i)$ ) point's distance from an observation point ( $x_k(i)$ ) coordinate will never be more than half of  $L$ .

Once the array  $R$  has been defined, a single-value decomposition (SVD) is undertaken, equation 3.5 where  $S$  is the matrix of positive real singular values,  $V$  is not used here, and a rotation matrix  $U$  is recovered.  $U$  can be used to rotate into the coordinate system of the plane defined by the bathymetry nearest to the station.

$$USV = R \quad (3.5)$$

Once the rotation matrix  $U$  has been created by the SVD, it can be used to rotate the vector  $x_k$  that holds the locations of the nearby fields within the staggered grid, cell edges for E fields and cell faces for H fields in to  $x'_k$ .

$$x'_k = U^T(x_k - x_d) \quad (3.6)$$

Ultimately we want the value of the EM fields interpolated to the station in the normal Cartesian coordinate system, to do that we need to define a set of interpolation coefficients that can be multiplied by the EM field solution vector structure that comes out of the forward model. Once the plane has been defined and a rotation matrix constructed a QR decomposition is undertaken upon a design matrix, described next, to define these new interpolation coefficients. A QR decomposition provides a solution to the overdetermined problem for field interpolation (one 3-component field at the station location interpolated from 8 adjacent edges for each field component where solutions are found). It defines new interpolation coefficients to be applied to the solution fields within the forward model. As these coefficients are rotated by the previously-determined, surface-normal rotation matrix ( $U$ ), they already account for rotation into and then out of the surface-normal coordinate system.

Once rotated into the new coordinate system through equation 3.6, a design matrix is constructed that includes a set of equations describing the known and unknown variables of this overdetermined system. The design matrix is built upon the idea of Taylor expanding the fields described in equations 3.1 and 3.2 and will be the set of equations that QR decomposition will 'solve'. The rotated electric field vectors are stored in array  $e_{ki}^*$ , depicted in equation 3.7 where  $e_{di}$  describes the sought after value of the fields at the station, the  $i$  index denotes the x, y, or z coordinate (the 1, 2, and 3 indices denote the x, y, and z coordinates as well), index  $k$  represents which staggered grid node the field is associated with and the  $\beta$  terms are the coefficients for the gradients of the electric field. The  $*$  denotes that the z component of the derivative of the electric field has been replaced by the current  $J_z$  to account for the included Shantsev and Maa0 coefficients  $\alpha_{ki}(\sigma)$ . The value  $\alpha_{ki}(\sigma)$  is



determined by what side of the conductivity interface the given  $x_k$  point lies, having the form  $\frac{1}{\sigma_k} - \frac{1}{\sigma_d}$ , where  $k$  indicates the observation point and  $d$  the station.

$$e_{ki}^* = e_{di}^* + \beta_{i1}x'_{k1} + \beta_{i2}x'_{k2} + \alpha_{ki}(\sigma)\beta_{i3}^*x'_{k3} \quad (3.7)$$

One can see from equation 3.7 that each component of the interpolated field,  $e_{di}^*$ , is associated with all 3 components of the solution fields,  $e_{ki}^*$ , through the 3 right-most terms. Equation 3.7 can be deconstructed into  $e_k^* = X_k^*b$ .  $b^T$  holds the values of the electric field at the station location and the  $\beta$  coefficients in the rotated planar coordinate system as shown in equation 3.8. The  $\beta$  coefficients incorporate the spatial derivatives of the fields between solution locations and the interpolation location at the site.

$$b^T = [e_{d1}^* \ e_{d2}^* \ e_{d3}^* \ \beta_{11} \ \beta_{12} \ \dots \ \beta_{23}^* \ \beta_{33}^*] \quad (3.8)$$

$X_k^*$  contains the location vectors for the electric and magnetic field nodes, expressed in the plane-normal coordinate system, for the staggered grid and the Shantsev and Maaou  $\alpha_{ki}(\sigma)$  coefficients. We then define  $X_k$  as the form of  $X_k^*$  that has its  $z$  components divided by the conductivity at point  $x_k$  to convert the current density coefficients back into electric field coefficients, via the definition for current density. We end up with  $e'_k = X_k b$ . The matrix  $U$  rotates  $e'_k$  back into its standard (model grid) coordinate system form  $e_k$  through  $e_k = Ue'_k$ . We can define equation 3.9, where  $U(i)$  is the row of the rotation matrix dependent on the coordinate system associated with the node in question, recall that each node corresponds to a different  $x$ ,  $y$ , or  $z$  component of the fields.

$$e_{ki} = U_{i(k)}X_k b \Rightarrow d = Xb \quad (3.9)$$

The left hand side of this equation can be used to construct a vector defined here as  $d$  that holds all of the  $e_{ki}$  fields needed to calculate the interpolated field  $e_d$  at location  $x_d$ . The matrix  $X$  is designed to have a row for each of the  $U_{i(k)}X_k$  terms for the needed  $e_{ki}$  fields in vector  $d$ . This defines the right hand side of equation 3.9. The matrix  $X$  is the design matrix, now rotated back into the model grid coordinate system, and through its QR decomposition the interpolation coefficients needed to perform the interpolation from the nearby unrotated electric field values  $e_k$  to the station are calculated.

As only the first 3 components of  $b$  (equation 3.8) are relevant to the desired interpolated field  $e_d$ , the only relevant components of the QR decomposition are those that can be used to find  $e_d$ , not the  $\beta$  terms in  $b$ . So  $e_d = R_3^{T-1}Q_3^T d = c^T d$ , where the 3 subscript indicates we only need the first three columns of  $Q$  and the upper right 3 by 3 block of  $R$ .

### 3.3 Results

The first adaptation undertaken with the Matlab version of the ModEM3D forward solver code was independent of the interpolation strategies discussed in the section above. Conservation of current density normal to cell boundaries was introduced as a necessary but mostly experimental improvement to test how all of the classes responded to changes in the interpolation function (equation 3.3). This adaptation proved that the changes in interpolation strategy could have an observable impact, so the two primary interpolation adaptations were then applied to the Matlab code.

We were able to adapt the SVD to the code and use it to define a plane that fits modeled bathymetry as shown in Figure 3.3. The interpolated electric fields created

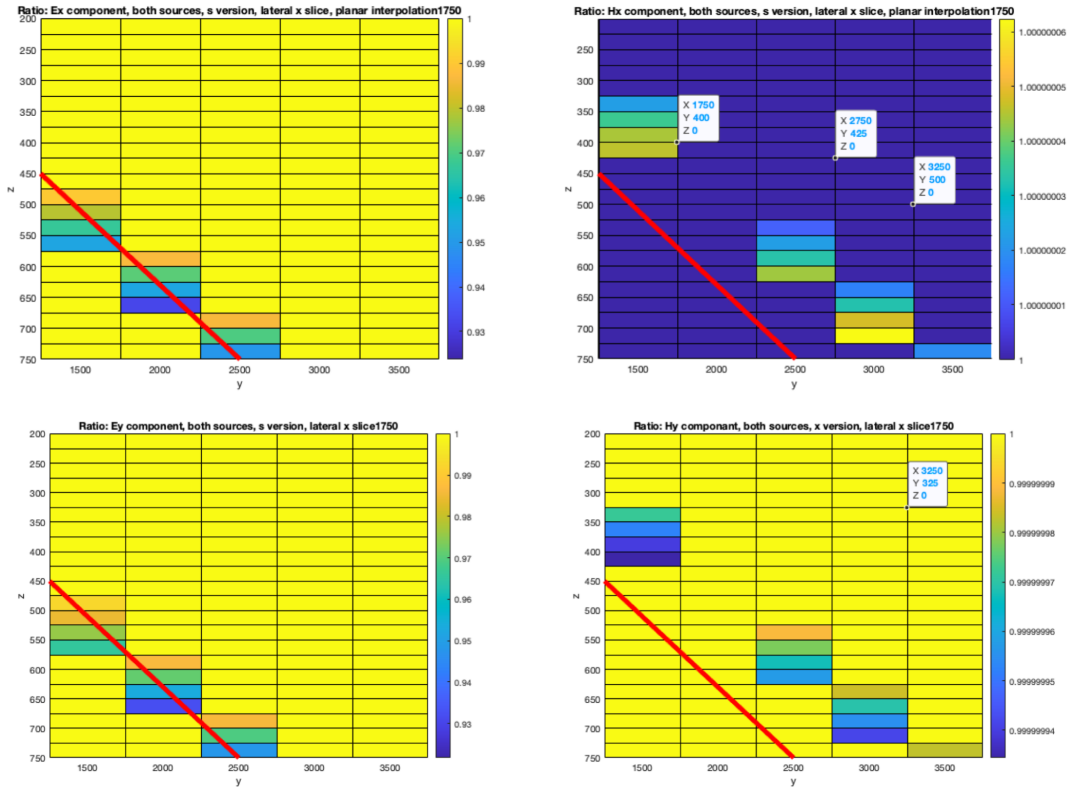


FIGURE 3.4. For each of these plots the electric and magnetic fields were interpolated to a station located in each cell, using the original trilinear spline interpolation strategy and the Shantsev and Maa0 Interpolation. The ratios of the fields using these different interpolation strategies are shown. The fields for both x and y source polarization are combined here. The red line shows the planar conductivity interface. The right column shows the electric fields, the left the magnetic. Cells that have a different color than the background indicate a change in the field do to the Shantsev and Maa0 interpolation scheme at that cell

from the new Shantsev and Maa0 and planar interface interpolation schemes differ from those created using the original tri-linear spline interpolation method. The Shantsev and Maa0 interpolation generates differences in interpolated field values for both the E and H fields along the sloped conductivity interface, as shown in Figure 3.4. This figure plots the ratio of the fields interpolated to each model cell using the Shantsev and Maa0 term over the original interpolation strategy. The new interpolation strategy shows changes in the fields along the sloping model bathymetry, particularly for the electric fields. The magnetic fields show a slight offset in where they experience the change from the boundary, compared to the electric fields. This is possibly related to the fact that the magnetic fields are being interpolated from cell faces rather than cell edges.

These fields appear to be affected by the conductive boundary imposed by the bathymetry, as shown in Figure 3.4, as well as Figure 3.5 and Figure 3.6 , where the interpolated electric or magnetic field of a station positioned in each block is calculated. For Figures 3.5 and 3.6 a separate forward model was run to calculate the displayed color in each of the cells of these plots, placing the station inside the cell and interpolating the field forward modeled fields to that location. Only the real components of the x oriented source polarization are plotted. The left hand column uses the original trilinear spline technique where as the right uses the new interpolation strategies, so that we can critique the new interpolation scheme. For the right hand column, we see greater contrasts in solution fields upon crossing the tilted surface(red line), as we would expect. The y components in particular for the E and H x source polarized fields appear to be more sensitive to the conductive boundary with the new interpolation.

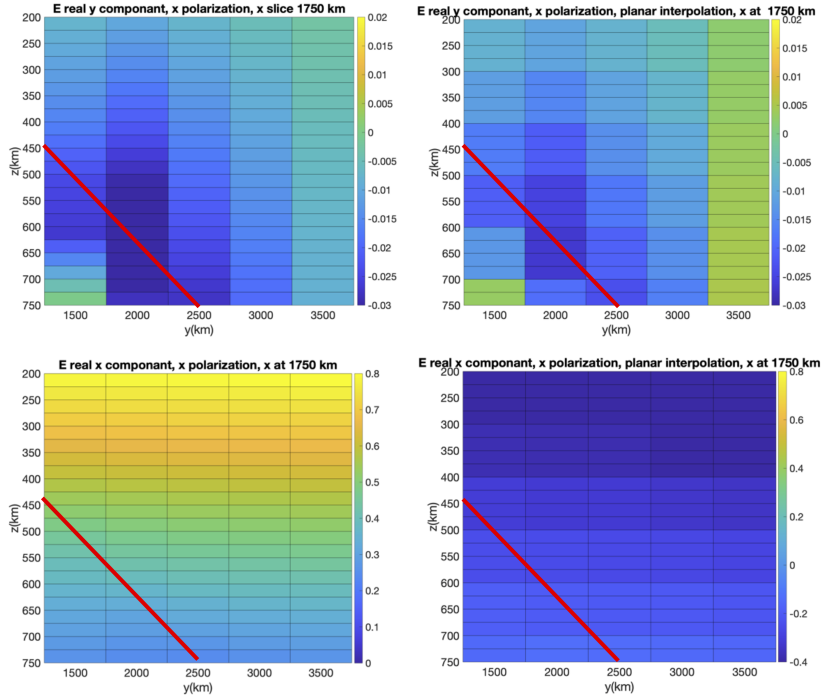


FIGURE 3.5. A  $x$  cross section of a plot of the  $x$  polarization of the real components of the  $E$  fields interpolated to a station located within each cell. This was done for the old trilinear spline interpolation strategy and the joint Shantsev and Maa/planar interpolation scheme. For each of the cells modeled here the electric fields were interpolated to the location of test a station placed in the cell. The left column of plots is from before inclusion of the new interpolation methods, and the right column is after. The red lines indicate the position of the model bathymetry. The polarization refers to the orientation of the source field.

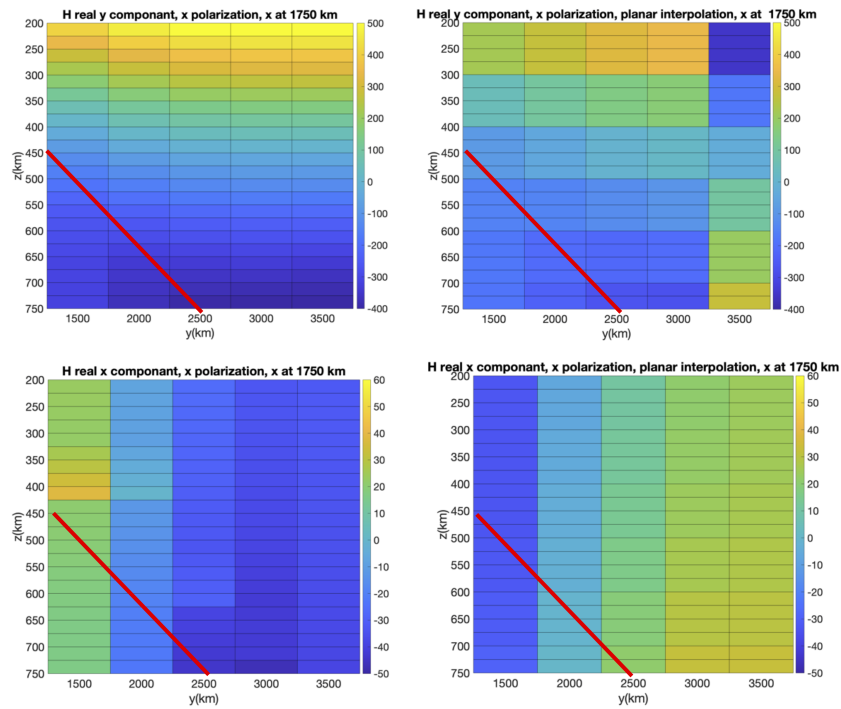


FIGURE 3.6. The Magnetic field version of the previous figure. A x cross section of a plot of the x polarization of the real components of the H fields interpolated to a station located within each cell. This was done for the old trilinear spline interpolation strategy and the joint Shantsev and Maa0/planar interpolation scheme. For each of the cells modeled here the magnetic fields were interpolated to the location of test a station placed in the cell. The left column of plots is from before inclusion of the new interpolation methods, and the right column is after. The red lines indicate the position of the model bathymetry. The polarization refers to the orientation of the source field.

These changes still need to be adapted to the working, FORTRAN version of ModEM3D.

This entire process was very complicated, so undiscovered bugs are likely. Once the QR solution for the interpolated fields is found, the principle challenge is sorting the resulting coefficients so that they operate upon both local like-component fields,  $E_x$  at nodes from adjacent forward solutions and, also, add other components(eg.,  $E_y$  and  $E_z$  in this instance) that have contributions arising from the rotation( $U$ ) before the interpolation. Also, the addition of other field components(like  $E_z$ ) of the discontinuous, surface-normal derivative corrections outlined in Shantsev and Maa0 [30] need to be preserved. Another possible source for errors that arose is the underlying fact that interpolation to the station location comes from a different set of locations for each of  $E_x, E_y, E_z$  and  $H_x, H_y$ , and  $H_z$  the latter determined for the center of faces of the Yee cell. Potential bugs aside, the framework for the new interpolation schemes is in place for further development.

## CHAPTER IV

### MEETING THE CHALLENGE OF MAGNETOTELLURIC IMPEDANCE

#### ‘PHASE TAILS’

Magnetotelluric data containing phase tails have been collected around the world from the Archean shield of Canada ([51] ), the South American Andean volcanic Belt [52], the Cascadia Subduction Zone [53], to the Himalayan Fold Belt [54]. In this chapter we investigate the phenomenon where the phases of off-diagonal elements of magnetotelluric impedances exceed 90 degrees, known as ‘rolling out’ of their normal quadrants. This phase roll out makes it difficult to invert the affected sites, hereafter referred to as ‘phase tail’ sites.

Phase tail phenomena are properly identified when phases of impedances relating observed horizontal (x & y) electric to magnetic fields(1.2 equation 1.4) for a given MT station ‘rolls’ out of quadrant for several successive periods, and in a manner that does not match what is expected from slopes of loglog graphs of corresponding resistivities. Often this type of behavior occurs over the longer periods extending to the longest acquired period, this aspect of a phase plot looks like a tail, hence the name 4.1. Phase can be expressed for four different arrangements of the arctangent of the imaginary divided by the real parts of the horizontal EM field data  $\frac{E_x}{H_y}$ ,  $\frac{E_y}{H_x}$ ,  $\frac{E_x}{H_x}$ ,  $\frac{E_y}{H_y}$ . Changes in phase for a given impedance element indicate sounding through variations in conductivity, and are related to the slope of loglog plots of apparent resistivity for that element, with phases typically remaining within an expected quadrant, for example 0 to 90 degrees. When mathematically rotated to an appropriate angle, the diagonal elements of the MT impedance will be nominally minimized and the off-diagonals will present information about strike, the direction in which conductivity varies the least or not at all, and it’s horizontal, orthogonal



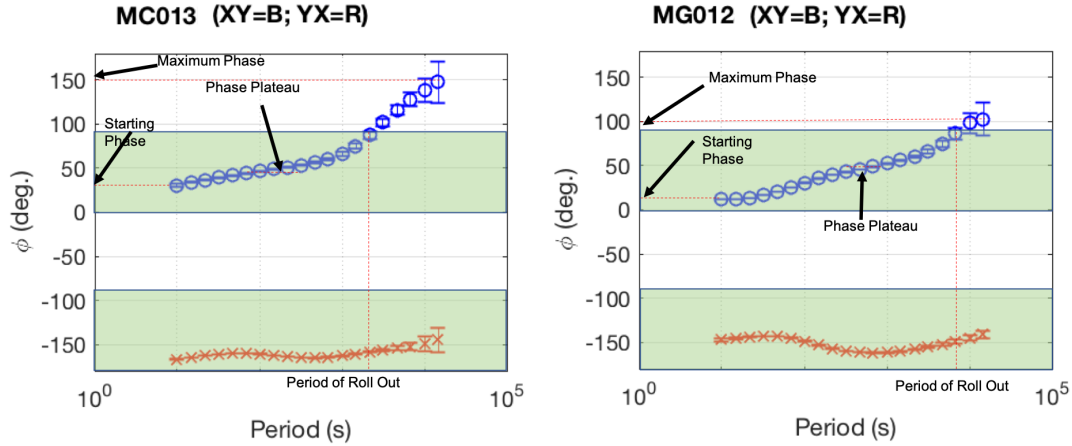


FIGURE 4.1. This an example of two phase tail sites, Stations MC013 and MG012 of the MOCHA Array. The green area highlights phases from 0 to 90 degrees. The XY phase is in blue while the YX is in red, both of these site display XY phase tail behavior.

complement. When the impedances are properly rotated to be pointing along strike, phase tail phenomena are characterized by behavior of the off-diagonal terms,  $\frac{E_x}{H_y}$  and  $\frac{E_y}{H_x}$ , as phase of the diagonal terms routinely spans quadrants in otherwise non-phase tail-affected observations. Usually only one of the off diagonal phases is affected, depending on the orientation of strike, or local strike, defined as the orientation of a prominent nearby large elongate conductor that does not orient in the same direction as strike. A conductor significant enough to impose a local strike can cause phase tail phenomenon as well, potentially observed in both off diagonal modes, maximized in a coordinate system rotated in the direction of the local strike. As phase tail events don't match 'normal' phase behavior, such as not correlating with the slope of the resistivity graphs, they present significant challenges to traditional interpretation processes, namely iterative, linearized inversion of data through minimization of a penalty function. Thus phase tail-impacted data is typically omitted from inversion, resulting in information loss, and a loss of resolution in the resulting model.

Egbert [24] demonstrated theoretically that complex 3D conductive structures, in a manner analogous to folded wires, could channel induced electric currents so as to reverse their expected directions relative to an inducing (source) magnetic field. Further, currents induced by both source polarizations (TM and TE) can be channeled in the same direction, generating the phase tail phenomena. Wannamaker et al. [55] discussed how anomalous behavior in the electric fields at low frequencies, oriented parallel to finite-length, shallow tabular conductors, is caused by deficient current gathering, known as ‘current starvation’, through surrounding host resistive layers. Livelybrooks et al. [51] attributed observed phase tails to deflections of currents gathered via mineralized conductive zones in ‘feeder’ faults bounding the Trillabelle ore body into directions typically associated with the other source mode. Heise et al. [53] explained this phenomenon by creating 2-D models that relied primarily on horizontally anisotropic conductivity; they overlay two layers of contrasting anisotropy to generate the phase tail phenomena. Lezaeta and Haak [52] showed that extending a smaller, anisotropic or elongate conductor from the ocean, itself a large region-spanning conductor, at various oblique angles, can lead to phase tails. Employing the distorted field impedance decomposition method of Smith [56], they attributed this phenomena to both current channeling and distortion in associated magnetic fields. Ichihara and Mogi [57] synthesized the work above into the idea of specific geometries for a ‘local’ conductor extending from a larger, shallow, tabular ‘regional’ conductor. They showed that a local conductor extending from the end of a much larger ‘regional’ conductor can generate phase tails without relying on arguments for anisotropic conductivity or connecting to an ocean. This is significant because here we attempt to explain phase tail phenomena observed in

Cascadia (onshore Washington and Oregon), a region that some have interpreted as exhibiting little evidence for anisotropy [34].

Here we first examine results from variations of 3-D forward models, based primarily on the shallow tabular conductor model geometries advocated by Ichihara and Mogi [57], and with none invoking conductivity anisotropy. Models we consider are constrained by assumed local geologic limits on conductivities. Through this process we identify key parameters that control the presence and content (period, shape, etc.) of phase tails. We next describe the consequences of these key parameters and present physical explanations for their individual effects. An overarching goal of this work is to determine inversion methodologies that retain, rather than omit or downweight, phase tail-impacted data, as we deem it likely that downweighting or omitting phase tail data reduces the resolution of resulting inversions.

We apply the resulting inversion methodology to analysis of, in particular, MOCHA, EarthScope Transportable Array [58], and historic data from the Pacific Northwest region of North America 1.2 to investigate the potential of these revised inversion methodologies. Under certain conditions phase tail data can be used to identify a range of conformations of conductors, here we assume these to be range between L-shaped and T-shaped, following Ichihara and Mogi [57]. This work thus expands and generalizes the example of Xiao et al. [54], who used the presence of phase tail data to identify low resistivity structures along the Northern Qaidam Basin; and used forward models with specific structures inserted that replicated, approximately, observed phase tail data.

A goal of this work is to determine the key model parameters controlling the behavior of phase tail-impacted impedances, for example at what periods phases will

roll out of quadrant and the shape of the phase curve near and beyond those points. With these parameters identified we can optimize them with constraints assumed from the geological environment surrounding the sites; we started by identifying some candidates from the literature. Lezaeta and Haak [52] identified placing intermediary conductive layers between a model's background resistivity and the extended conductors as an optional parameter that can be varied, additionally they extended their tabular conductor from the ocean. Ichihara and Mogi [57] first suggest using a .3 ohm- regional conductor with a 3  $\Omega$ -m local extension, which they do adjust, and a 1000  $\Omega$ -m background resistivity, however this background resistivity is a bit resistive compared to what the surface geology around our sites suggests, requiring some adjustment.

A focal point for this work is to uncover what naturally-probable geological structures and surface geologies correspond to phase tail behavior. Theoretical works such as Ichihara and Mogi [57] use very conductive structures and a resistive background to generate phase tail behavior that would likely be unrealistic for structures found in Cascadia. To compensate for this inconsistency we adapted their theoretical models using a geologically reasonable background resistivity, regional, and local conductor resistivity values taken from both the geological literature and previous conductivity models made of the region [[22]; [59]].

We experimented with the parameters of the L shape, such as length, conductivity contrast, and depth, to generate synthetic phase tails that more closely match those observed in real data. Stretching the regional conductor main body of the L conductor, against the direction of local strike laterally beneath the local conductor, leads to a smoother shaped phase plot and starting phase consistent with observations. The stretching also allows for more geologically-reasonable resistivity

values for the models conductors and background resistivity. Having conductors surrounding the structure, and a layered resistive background more accurately reflects the phase behavior in the MOCHA-related data 4.2. We show through forward modeling that a more T-like structure, where a smaller ‘local conductor’ slides towards the center of the larger, tabular ‘regional conductor’, better reproduces the behavior of the phase tail sites observed for MOCHA, using more resistive and realistic regional and local conductors, especially when coupled with other nearby conductive features. We located the sites that displayed phase tail behavior on USGS surface geology maps and noted that the phase tail sites correlated to regions with mapped and inferred, near-surface basaltic, siltstone, and soapstone formations encompassing large swaths of Earth such as old river and lake beds. Figure 4.3 shows an example of a MOCHA site, MC13 mapped on a USGS surface map. These correspond with the tabular, elongate regional near-surface 5-7  $\Omega$ -m conductors that we model as overlying resistive layers, referred to as surface conductors later in this chapter. Surface geological studies supports the presence of somewhat more resistive, 5-10  $\Omega$ -m regional conductors and 1-5  $\Omega$ -m local conductors[59]. By comparing these geological features to our models, we propose a motif that explains the appearance of phase tail behavior in our data, expanding upon the work of Ichihara and Mogi [57] and others.

Our starting point for this research was a forward model resulting from an inversion of MOCHA data, achieving an RMS misfit of 2.6, and generated without fitting any of the observed phase tail data [22]. Using the results from the first two elements of this work– identifying specific model geometries that result in phase tails, and employing information about parameters that control specifics of the shape of phase tail plots– we hope to insert specific phase tail-related structures into the

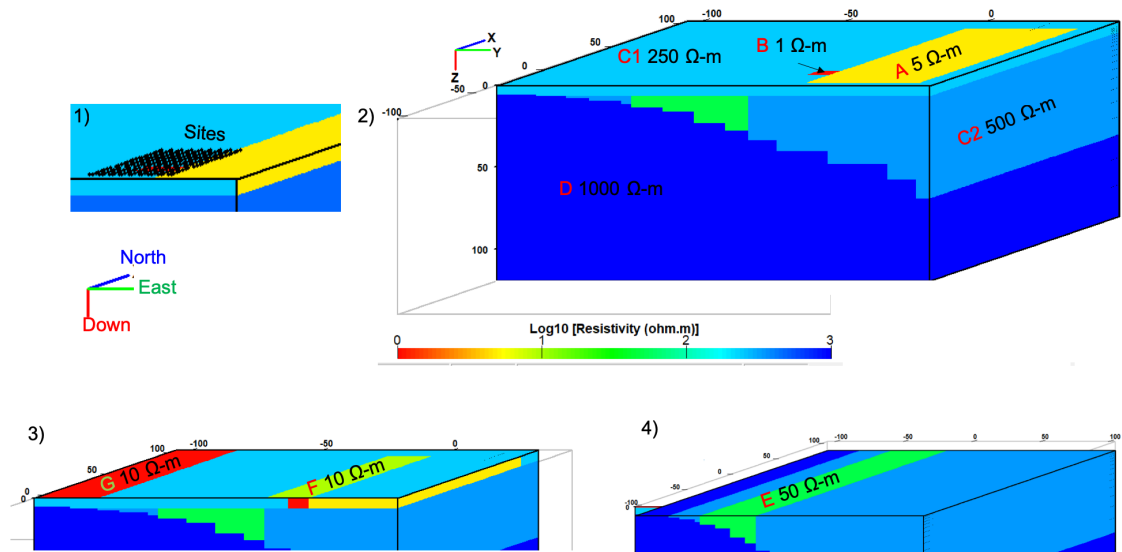


FIGURE 4.2. A 3-D cross section of a typical starting model used to determine which model variables best recreate phase tail phenomena, each subsection shows a different slice into the model to highlight different features. A refers to the regional conductor; B is the local conductor; C1 and C2 point to the surrounding resistive background, note that the background is layered; D refers to the modeled subducting slab; E refers to a conductive structure referred to here as a ‘subconductor’ located below the ‘T-shaped’ conductor made up of the local(B) and regional(A) conductors; F refers to a conductive structure located above the local conductor referred to here as a ‘surface’ conductor; and G refers to a conductive structure built to replicate the effects of the ocean. Black markers in section 1 indicate where phase tail sites are observed. Note that this model cross section in section 2 is taken several layers below the surface starting at roughly 2 km deep. Section 3 shows the top layer of the model and section 4 shows a cross section starting directly below the ‘T-shaped’ conductor. The conductivities shown are for this specific model, conductivities and dimensions of features can vary for different desired phase tail behavior as described in this chapter.

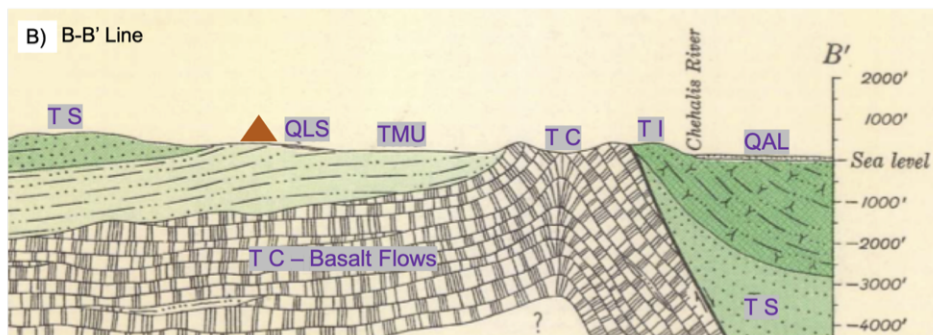
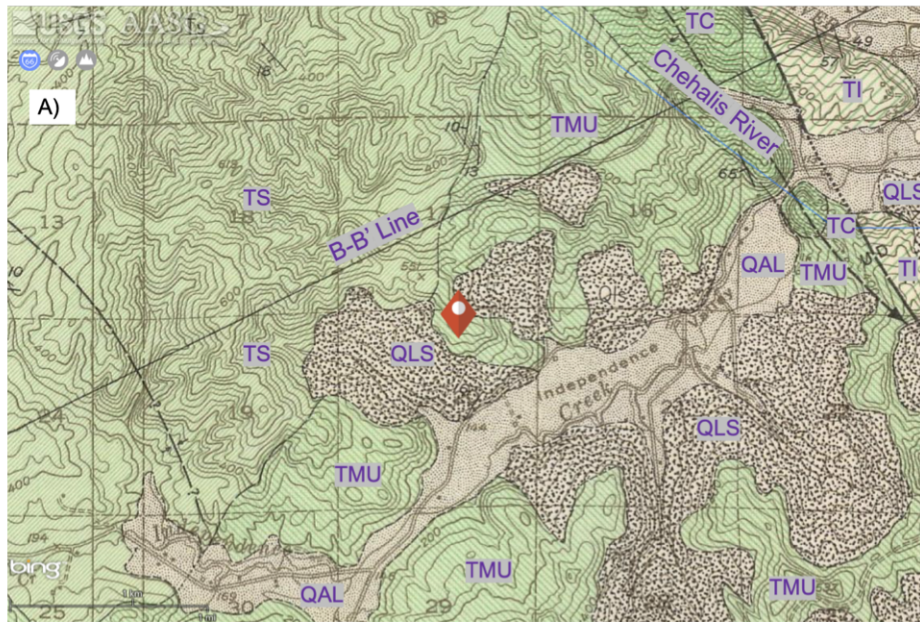


FIGURE 4.3. A) MOCHA site exhibiting phase tales, MC13 shown on a USGS surface map as an orange diamond. The letters correspond to the surface geology in each color coded region. TMU - The region directly below site MC-13, it corresponds to layering of bedded siltstone above regularly bedded basaltic tuffaceous sand stone and siltstone, thin basalt flows, and tuff. TS - The Skookumchuck formation consisting of broken up powdery micaceous feldspathic sandstone and thin bedded siltstone and sandstone. TC- Crescent Formation, consists mostly of basalt flows and tuffaceous and basaltic sedimentary rocks. TI- Tuffaceous sandstone and sandy silstone, thin calcareous sandstone beds. QAL- Alluvium made up of silt, sand, and gravel. QLS- Land slide debris, debris from tertiary and quarternary rocks. B) A cross section along the B-B' line drawn in Figure A, the orange triangle represents the approximate projection of MC13 onto this line. While this line is not precisely below MC13, this cross-sectional view is likely representative of what lies directly below MC13.

starting model. Ultimately, we will insert the structures so that phase tail data can contribute to the inversion, eliminating the need to remove it to preserve a reasonable fit of model simulated to actual data.

#### 4.1 Model Geometric and Associated Geological Settings

Region-spanning, shallow tabular electrical conductors corresponding with, for example, elongate basins, are common throughout much of the world, and comprise basalts, silts and sandstones, to other sedimentary rocks [1]. Magnetotelluric modeling methods involving inversion delineate these large conductors accurately because the method is very sensitive to the tops of conductive bodies. The two-dimensional concept of strike assumes there is one direction along which conductivity does not vary. This sets a natural coordinate system for the two source polarizations necessary to find complete forward solutions for given 2D or 3D conductivity models and, further, for inversion of observed data. In a three-dimensional scenario, strike may not be as obvious, but is generally assumed to be in the direction of and horizontally orthogonal to the direction of elongate features, such as oceans, coastlines, basins, volcanic arcs, etc. This, then, defines the cardinal horizontal directions for estimating magnetotelluric response functions for 3D models used in inversions. Near-surface 3D conductors, however, can channel current in problematic ways that complicate interpretation, causing electromagnetic effects, such as frequency-dependent induced current loops or ‘galvanic’ (frequency-independent) shifts [24].

For example, strong conductivity gradients, encountered in passing through the end faces of elongate tabular 3-D conductors, into surrounding more resistive host



rock, can ‘starve’ the conductor of induced currents when compared to the 2-D case [55]. Boundary conditions dictate that current oriented normal to the face,  $J_x$  for faces perpendicular to a chosen x-direction, be continuous through the boundary, which effects a discontinuity in  $E_x$  in crossing the boundary, following the relationship in equation 4.1 and 4.2 as depicted in Figure 4.4.

$$J_x = \sigma E_x \quad (4.1)$$

$$\sigma_{outside} E_{outside} = \sigma_{inside} E_{inside} \quad (4.2)$$

When compared to the 2-D case, however, current starvation effects result in diminished  $J_x$  within the tabular conductor and, thus, the total electric field,  $E_x$ , is suppressed compared to the 2-D case. This can be thought of, alternately, as an overabundance of ‘free boundary charge’ defined by equation 4.3 where  $y$  is the admittivity of the material containing the conductor in [55], time-varying charge along the end boundary faces of the tabular conductor serving as an electric field source that, when added to the strike-parallel electric field for the 2-D solution, diminishes the total field within the conductor.

$$\sigma_{boundary} = -\frac{1}{y} \vec{\nabla} J_{surface} \quad (4.3)$$

The greater the amount of ‘free boundary charge’, or alternately ‘current gathering’, as estimated using the above term, the greater propensity to try to channel x-directed current from elsewhere into the tabular conductor, where possible. [55] suggest that this current gathering effect gains importance at lower frequencies. The inductive scale length C 4.4, (e.g., [60]) can be calculated for a given frequency

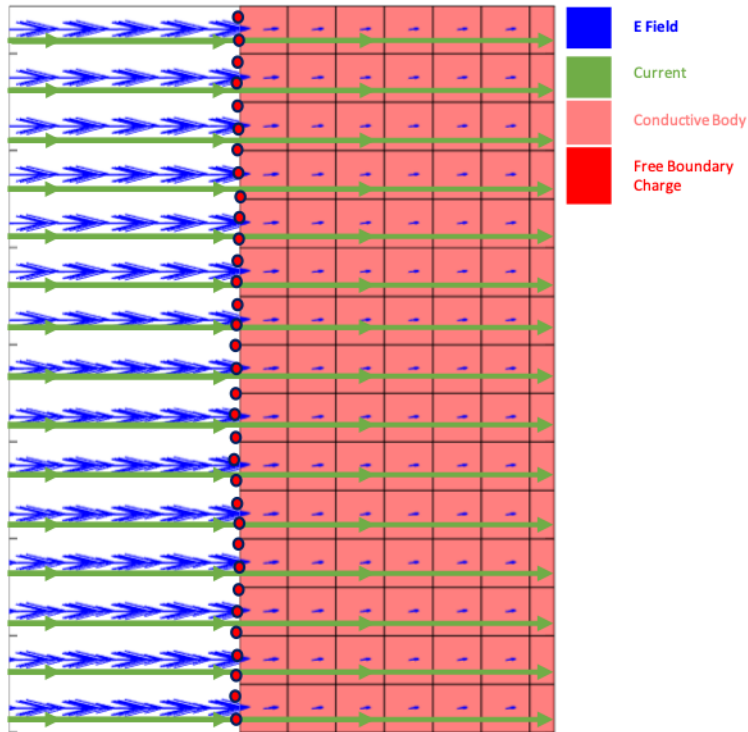


FIGURE 4.4. The boundary conditions on the electric field and current between a resistive medium, and one that is more conductive. The current in green is continuous across the boundary while the E-field in blue is discontinuous to compensate according to electromagnetic boundary conditions imposed by Maxwell's equations. Free boundary charge in red gathers at the border between the conductivity difference to accommodate the discontinuity in the E-field.

and resistivity of the resistive host. Current starvation effects are enhanced when the inductive scale length approaches and exceeds the overall length of the tabular (regional) conductor.

$$C = \frac{|Z|}{i\omega} \quad (4.4)$$

Scavaging of currents causes currents to act in ways counter to the basic assumptions of MT as shown in Figure 4.5 [[24]; [55]]. Given favorable configurations of electrical conductors, this current starvation effect drives the gathering of currents from the other source polarization,  $H_x$ . The  $H_x$  source polarization otherwise induces electric fields ( $E_y$ ) perpendicular to the elongate vertical faces of the tabular conductor, though of course these induced electric fields can deflect vertically as well. Given appropriate configurations of conductive and resistive elements this vertical deflection can itself cause anomalous phase behavior [[24]; [57]]. Currents incident normal to the end faces of tabular conductors, where the free charge initially gathers, increases the build up of free charge at the boundary, making a time varying effect that gathers more current [24]. In the near surface case, where model configurations disallow the scavenging of other-mode ( $H_y$  sourced) electric fields, this type of anomalous behavior can result in galvanic distortions in the the presence of smaller conductors, or as focused upon in this dissertation, phase tail phenomena [[52];[24]].

Earlier research often invoked anisotropy, where conductivity differs depending upon direction, essentially a scalar physical property becoming a tensor, to explain phase tail phenomenon [53]. Heiss and Pous [53] employ a thin anisotropic sediment layer, assumed to be primarily composed of black schist and graphite, but without a large tabular conductive body, to explain phase tail phenomena. Thus a current-sharing relationship between two conductors isn't required for this

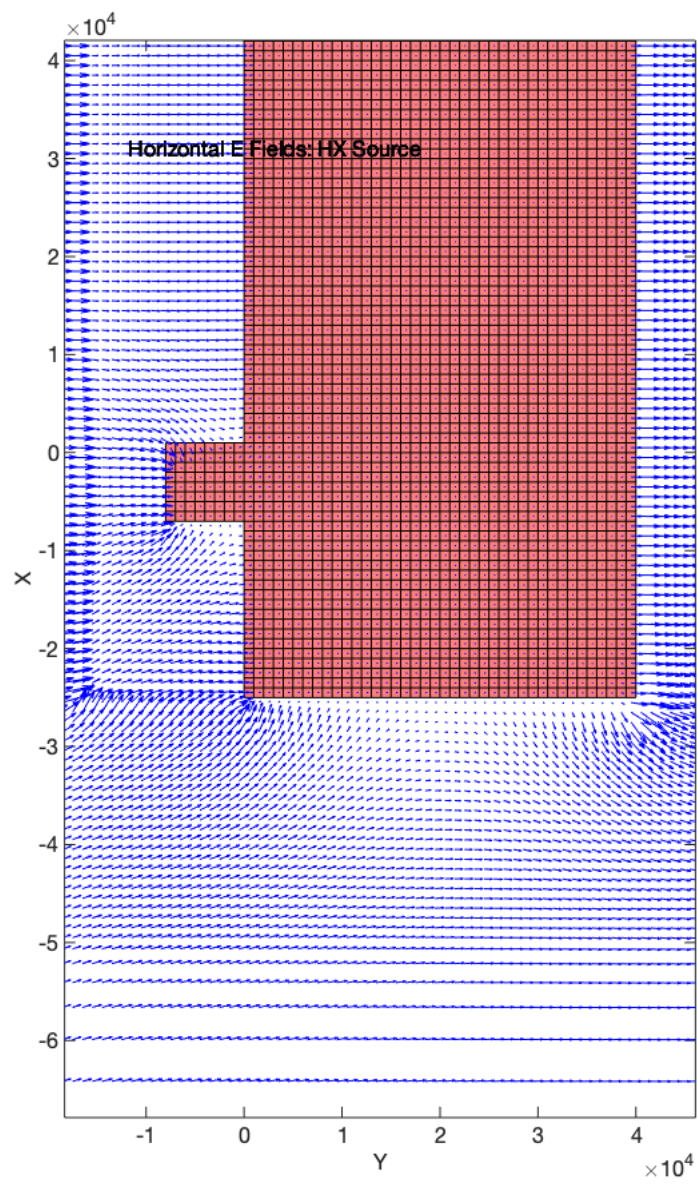


FIGURE 4.5. The distribution of the  $H_x$  sourced polarized Electric field around an L shaped conductor.

explanation but, rather, an appeal to the presence of the anisotropy itself within a single, near-surface 250-650 m located depth-spanning feature is employed to explain observations of out of quadrant phase. Ichihara and Mogi [57] criticizes this explanation as not accounting for explanations involving sediments present at greater depths ranging from 1-4 km in depth. Furthermore, non-anisotropic conductivity models resulting from two-dimensional inversion of the EMSLAB MT Lincoln Line (extending approximately east-west at about 45° North) in Cascadia fit non-phase tail impacted data equally well as inversions employing the anisotropic code of Baba et al. [61], leading Evans et al. [34] to conclude that there is "no evidence for significant structural electrical anisotropy beneath the EMSLAB profile." Phase tail behavior can be generated without the need of rarely-found anisotropic sediments like graphite or black schist [57].

Large, tabular, region-spanning conductors connected to smaller local tabular conductors in an L-like configuration can channel currents induced by the free boundary charge to create phase tail behavior without appealing to anisotropy [57]. The orthogonal magnetic ( $H_x$ ) field can source some of these currents channeled by the conductor, causing them to carry quite a different phase relationship than that belonging to the  $H_y$  source polarization induced currents traveling along local strike of the elongate regional conductor. This L-shaped conductor model is quite plausibly found within the northern section of Cascadia, extending from Washington into Oregon along the western coast of the continental United States. Large tabular conductors are common-place throughout the region as shown in Figure 4.6 taken from the same MOCHA inversion discussed in II [[22]; [34] ; [35]]. Figure 4.6 illustrates that many regional conductor candidates exist in the modeled study area, making the L shaped conductor model for phase tails a good candidate for the

area. The conductance and arrangement of the L-shaped conductor, as well as other variables not investigated in the previously mentioned literature, must be adapted to generate the specific phase tail behavior seen in the region; as models considered by Ichihara and Mogi [57] generate more extreme phase tail plots than are observed in the expanded MOCHA data set. Another goal of this research is to examine local geological constraints on the shapes and conductivities of L-shaped conductor models employed to explain phase tail behavior.

Most of the MOCHA sites exhibiting phase tail behavior are located in regions with extensive, mapped silts and sand stones, within a kilometer of a river, and often situated on a dry river bed 4.3 [62]. Silts and sandstones both exhibit a wide range of conductivities, for example dry sandstones are known to have conductivities ranging between about 25  $\Omega$ -m to 1000  $\Omega$ -m [63]. Siltstone and sandstone together can have conductivities from 5  $\Omega$ -m for wet sandstone to 500  $\Omega$ -m for dry [64]. These resistivity ranges correlate well with those of background features, such as regional conductors and the background resistivity of the crust and mantle, observed in MOCHA inversions above 5 km [22]. As phase tail behavior is thought to be primarily controlled by conductive structures that lie within the first 4-5 km in depth, minerals and other geological features normally found at those depths naturally become the best targets to explain the make-up of the regional and local conductors necessary to explain phase tail behavior. Limestone, shales, and shallow water reservoirs are known to exist within geosynclines, like those located near fluvial features such as dry stream or river beds, from respective depths of 1.5-5 km, 0.5-2km, and 0.1m-2km, but greater salinities are found at greater depths [[65]; [1]]. Limestones, shales and fresh-water reservoirs exhibit a range of resistivities between from 50 to 2000  $\Omega$ -m , approximately 5-30  $\Omega$ -m , and approximately 5 to 100  $\Omega$ -m , respectively

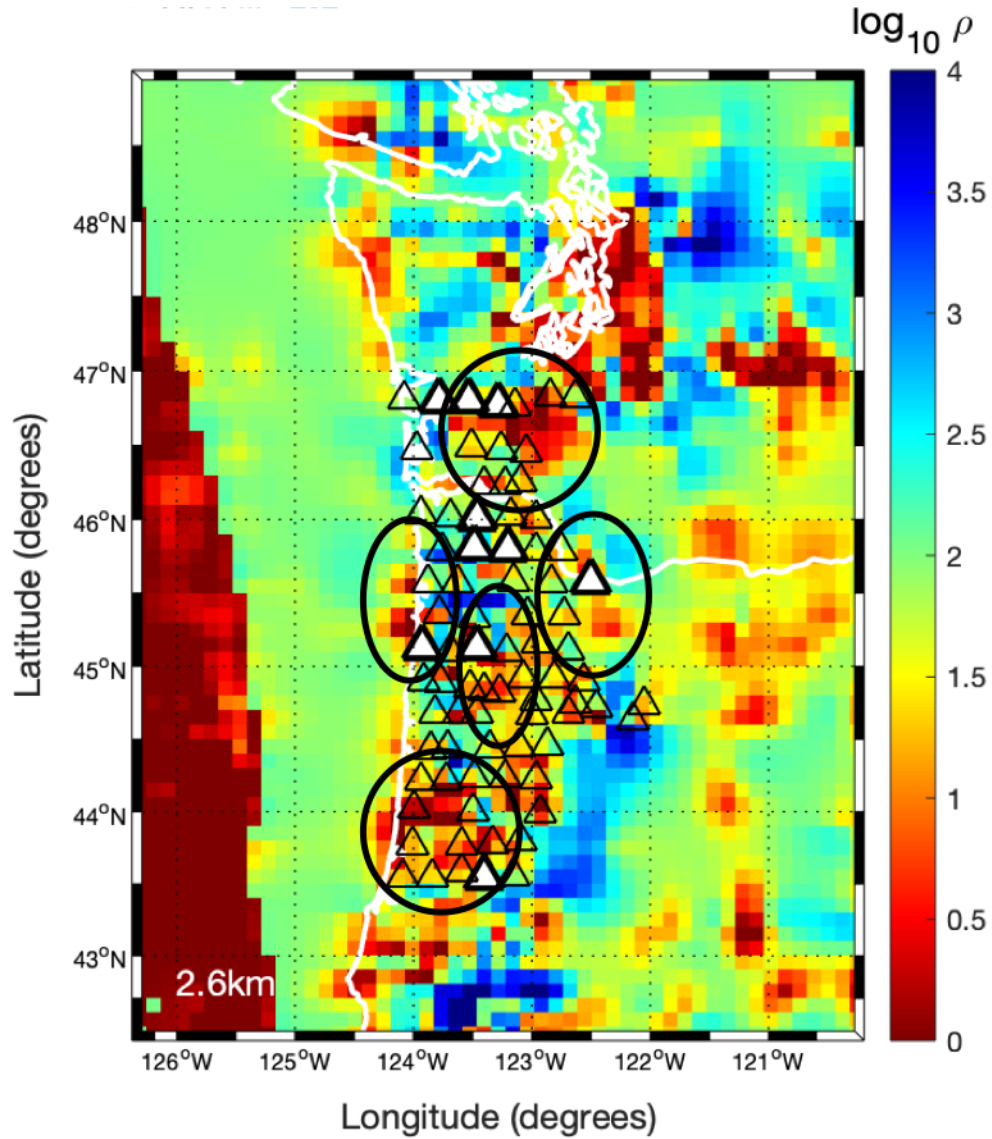


FIGURE 4.6. An unsmoothed conductivity map of the Cascadia model from II[22], this map shows conductivity sliced at 2.6 km depth. Circled features are potential regional conductors near phase tail sites, noted with white filled triangles. Red features are more conductive while blue are more resistive. The red conductor to the right is the conductive ocean.

[[59]; [66]]. Aquifers have a wide range of potential conductivities depending on their depths, resistivities can range as low as  $4 \Omega\text{-m}$  [65]. Other geologies that could realistically account for electrical conductors giving rise to phase tails within this depth range include: minerals mixed with magnetite—  $.00005 \Omega\text{-m}$  , graphite—  $0.1\text{-}10 \Omega\text{-m}$  , and massive sulfides—  $0.01\text{-}1 \Omega\text{-m}$  , however these more likely comprise of isolated small conductive bodies [59]. The conductivity ranges for all of the previously listed materials vary due to a variety of factors, including: porosity, permeability, salinity of the water within the pore spaces, pressure at depth, or the presence of networks of fluid-filled fractures. We have used these ranges to limit conductivities of features in trial models that produced phase tails.

## 4.2 Methods and Geological Constraints

We employed two main strategies to better understand plausible causes of phase roll out behavior in our data. The first involved locating the MOCHA sites on surface geological maps to determine the surface geology around each site. The second was to run a series of forward models using the MOD3DEM Inversion software [5] to see what modeled conductivity structures generated phase tail behavior similar to that observed in our data sets. The overarching goal was to both match observed data and to do so using only models with geologically-realistic conductivities and structures. While trialing a variety of forward models another goal presented itself, to impose the features that are known to cause phase tail behavior into the starting model of an inversion, in hope of mitigating the large RMS misfits introduced when trying to fit phase tail sites.



As previously discussed, out of quadrant phase roll out (‘phase tails’ ) have been shown theoretically to correspond to the presence of L shaped conductors, consisting of a regional conductor spanning 40-100 km or more connected to a smaller conductive tabular feature, known as the local conductor, nearer to the sites in question. More specifically, affected sites are found inside corners formed by a connected large regional conductor and a smaller local conductor protrusion close to the target site, see Figure 4.2 (1) [57]. It is useful to explore what key parameter values are necessary to replicate specific details of the phase tails present in the actual data, such as the starting period of roll out, how the slope changes with period, distance from a conductive body, etc. Ichihara and Mogi [57] used an L-configuration comprising of a  $0.3 \Omega\text{-m}$  regional conductor connected to a  $3.0 \Omega\text{-m}$  local conductor, all embedded within a  $1000 \Omega\text{-m}$  resistive background. We concluded, however, that this model does not accurately reflect the geology of the region, for example the conductivity of the large, regional conductor seems unrealistically high. While conductivities of  $0.3 \Omega\text{-m}$  are possible for saline reservoirs found at 2km or deeper depths [65], they would have to be prohibitively large, 40 km long or more, to fill this role. These reservoirs could still potentially explain the smaller local conductors. Ichihara and Mogi [57] showed that the conductance of the regional conductor and the position of the local conductor can be varied to be located at a position up to half way along the regional conductor and have conductivities from  $.03 \Omega\text{-m}$  to  $10 \Omega\text{-m}$  while simulating site data evincing phase tails. We have found that the constraints of the placement of the local conductor and the resistivity of the regional conductor can be relaxed when other features and variables are introduced into the model. For example, the resistivity of Ichihara and Mogi’s [57]  $1000 \Omega\text{-m}$  resistive background

can be reduced, effecting a transition from more extreme (higher slope) phase tail behavior to behavior more similar to that observed in Cascadia.

To better understand the phase tail behavior exhibited in certain Cascadia MT sites, we experimented to see how changes in each model parameter, fitting geological constraints on resistive backgrounds and regional/local conductors, affected the shapes of phase tail plots. This variable tweaking gave us a set of ‘knobs’ that we could adjust with respect to realistic geological parameters to effectively model the phase tail phenomena that we saw in the actual data. Further, plots of the observed phases inform the values for conductance, shape and other relevant model variables that inform our picture of the surrounding geology. Examination of these ‘knobs’ also forms a starting point for discussing the necessary physics driving phase tail phenomena. The rest of this section will describe each of these tunable controls and their significance. We describe the effects they have on the phase tail plots produced by forward models. We provide an explanation of the geological limitations of, and some of the physics behind what is happening for each control. The discussion and results section will delve further into the physics behind the most successful models and will propose a physical theory behind the cause of the phase tail phenomena.

The parameters (‘knobs’) with the most significant impact on forward model responses include:

- (a) the presence of near surface (depth range of 0.1-1.5 km), moderate (5-15  $\Omega$ -m) conductors (Near Surface Conductor in table) below the site but also above the more deeply-located regional/local conductor pair (0.6-5 km depth range).
- (b) the conductivity contrast between the regional and local conductors

- (c) the conductivity contrast between the regional/local conductor pair and the resistive host material, both around the conductors and underneath them (Background Resistivity in table).
  - (d) the shape, extent, and the placement of the regional conductor with respect to the local conductor
  - (e) the shape and extent of the local conductor
  - (f) the proximity to a highly-conductive ocean (Ocean in the table)
  - (g) the presence and location of a resistive subducting slab with respect to the site (Slab Resistor in the table)
  - (h) the presence of adjacent conductive structures under the regional and local conductors, referred to here as ‘subconductors,’ that more gradually transition the conductivity difference between the conductors and the background resistivity. They model the presence of deeper conductive structures (Subconductor in the table), for example the supraslab conductors imaged through inversion of the MOCHA data set in Chapter II.
- The challenge lies in finding the physical significance of each control and finding plausible geological origins for each. Some ‘knobs’ control the beginning phases of modeled phase tail curves, like the surface conductor, while others, like the length of the regional conductor control the maximum phase of the curve. Table 4.1 shows the effects that a change in each of the ‘knob-controls’ has on the phase of a comparison model (Figure 4.2a without the ocean conductor), chosen to best illustrate the effects of the ‘knobs’. Many models had to be made and tested to see what variable combinations proved the most viable. For the purposes of this discussion, length refers to changes in the x direction (along strike), width to changes

in the y (orthogonal to strike) direction, and thickness and depth to changes in z, cardinal directions listed are in reference to those labeled on Figure 4.2.

TABLE 4.1 Table displays the effects that the controls or ‘knobs’ discussed in this section 4.2 have on magnetotelluric phase. Each row corresponds to a different knob. All of the changes relating to the knobs were evaluated in comparison to the model displayed in row a of this table, with the exception of the \* rows, as noted above. When a particular knob is changed the other variables in the model are left unchanged. The comparison models displayed in every plot (black) follow the same basic structure as Figure 4.2, without the ocean conductor. The comparison models use a 5Ω-m regional conductor, 1 Ω-m local conductor, and a T-like structure with a 28 km extension south of the local conductor. The regional conductor is 150km long, 40 km wide, 6.5 km thick and is buried 0.5 km. The local conductor is 8km long (length here refers strictly to the x direction), 8km wide (width referring strictly to the y direction), and 6.5 km thick. A 50 Ω-m ‘sub-conductor’ lies beneath the regional and local conductors and extends in depth to the slab resistor. The slab resistor models the presence of a resistive subducting slab, it has resistivity of 1000 Ω-m and is introduced into the model starting at 7km depth.

\* These rows include the models without the presence of a surface conductor (open circles). The surface conductor can over-dampen the phase tail effect, limiting the range of observable phase changes before the phase tail effect is dampened out entirely.

TABLE 4.1 Phase Tail Plot

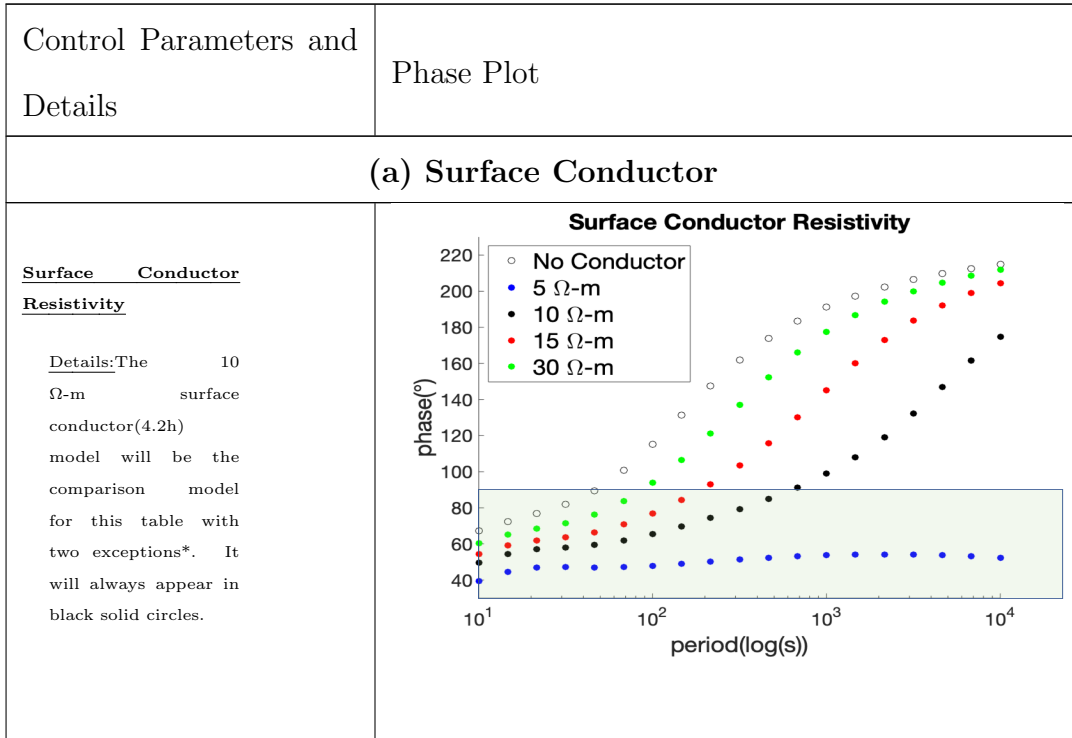


TABLE 4.1, continued

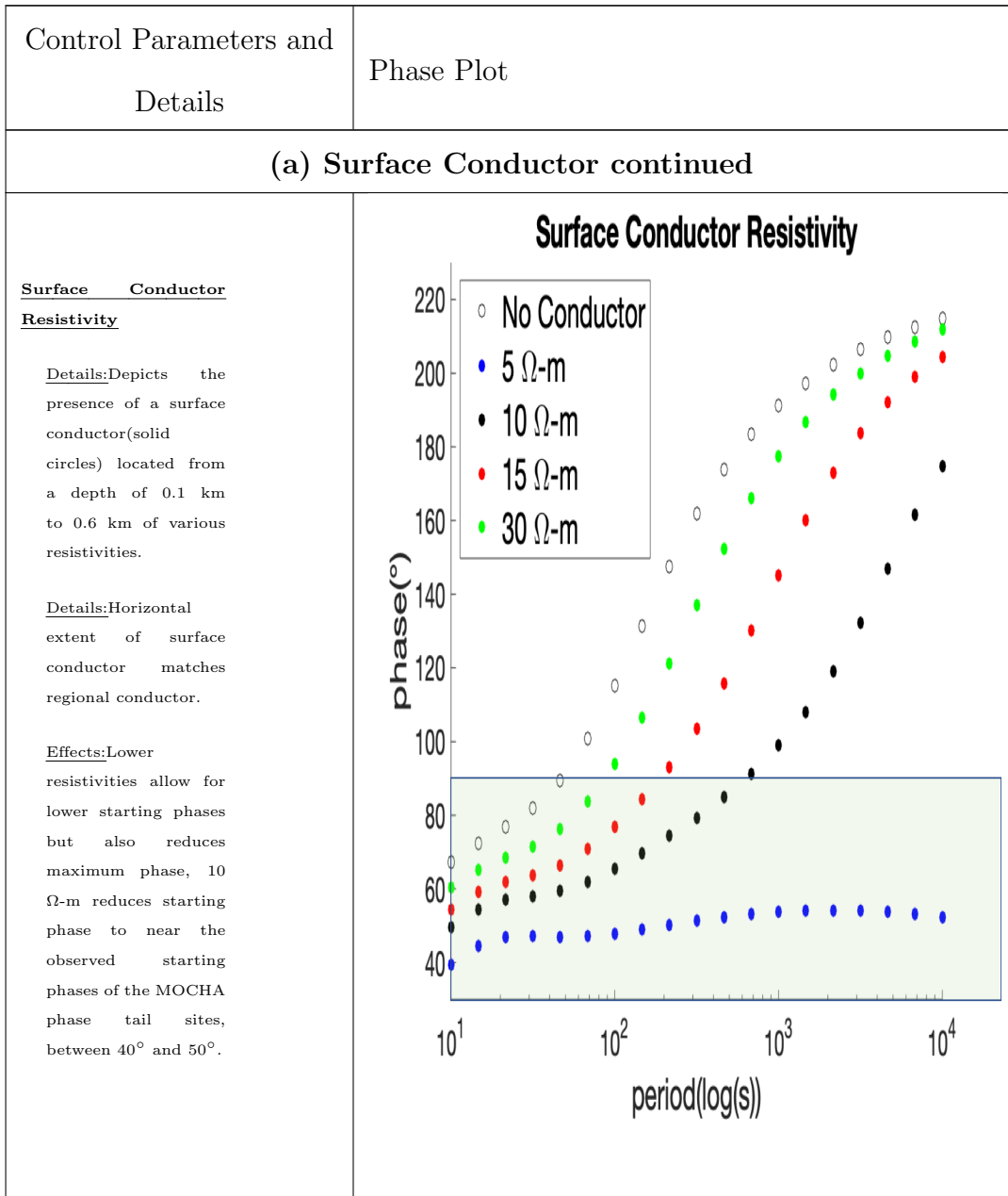


TABLE 4.1, continued

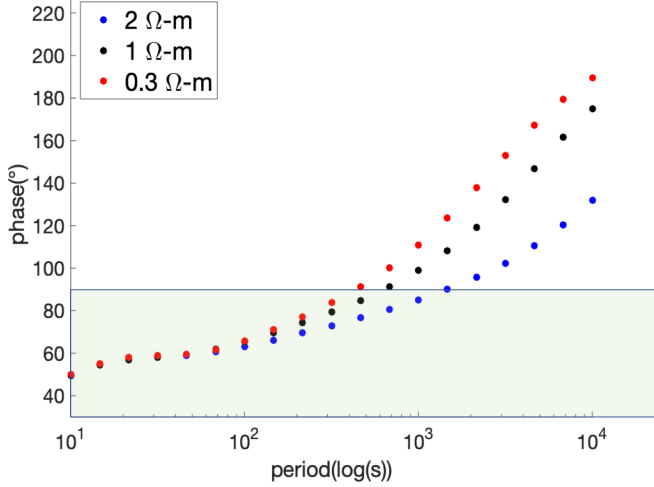
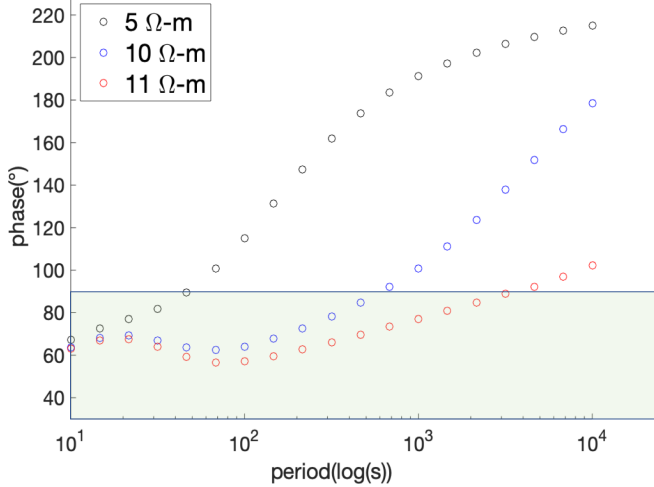
Control Parameters and Details	Phase Plot
<b>(b) Regional and Local Conductor Resistivity Contrast</b>	
<p><u>Local Conductor Resistivity</u></p> <p>Effects: 3 <math>\Omega</math>-m and higher lead to no phase tail.</p>	<p style="text-align: center;"><b>Local Conductor Resistivity</b></p>  <p>The plot shows phase angle (°) on the y-axis (40 to 220) versus period (log(s)) on the x-axis (10<sup>1</sup> to 10<sup>4</sup>). Three data series are shown: 2 <math>\Omega</math>-m (blue dots), 1 <math>\Omega</math>-m (black dots), and 0.3 <math>\Omega</math>-m (red dots). All series show a similar upward trend, starting around 50-60 degrees at 10<sup>1</sup> s and reaching approximately 130-190 degrees at 10<sup>4</sup> s. A light green shaded region is present at the bottom of the plot, between 40 and 80 degrees.</p>
<p><u>*Regional Conductor Resistivity</u></p> <p>Effects: 11 <math>\Omega</math>-m is the limit for this base model to exhibit phase tails.</p> <p>Effect: Any regional conductor resistivity above 7 <math>\Omega</math>-m leads to no phase tail with a 10 <math>\Omega</math>-m surface conductor.</p> <p>Details: Alternate comparison model without surface conductor used, open black circles*.</p>	<p style="text-align: center;"><b>Regional Conductor Resistivity</b></p>  <p>The plot shows phase angle (°) on the y-axis (40 to 220) versus period (log(s)) on the x-axis (10<sup>1</sup> to 10<sup>4</sup>). Three data series are shown: 5 <math>\Omega</math>-m (open blue circles), 10 <math>\Omega</math>-m (open red circles), and 11 <math>\Omega</math>-m (open black circles). The 11 <math>\Omega</math>-m series shows the highest phase angles, reaching nearly 220 degrees at 10<sup>4</sup> s. The 5 <math>\Omega</math>-m and 10 <math>\Omega</math>-m series show lower phase angles, generally below 180 degrees. A light green shaded region is present at the bottom of the plot, between 40 and 80 degrees.</p>

TABLE 4.1, continued

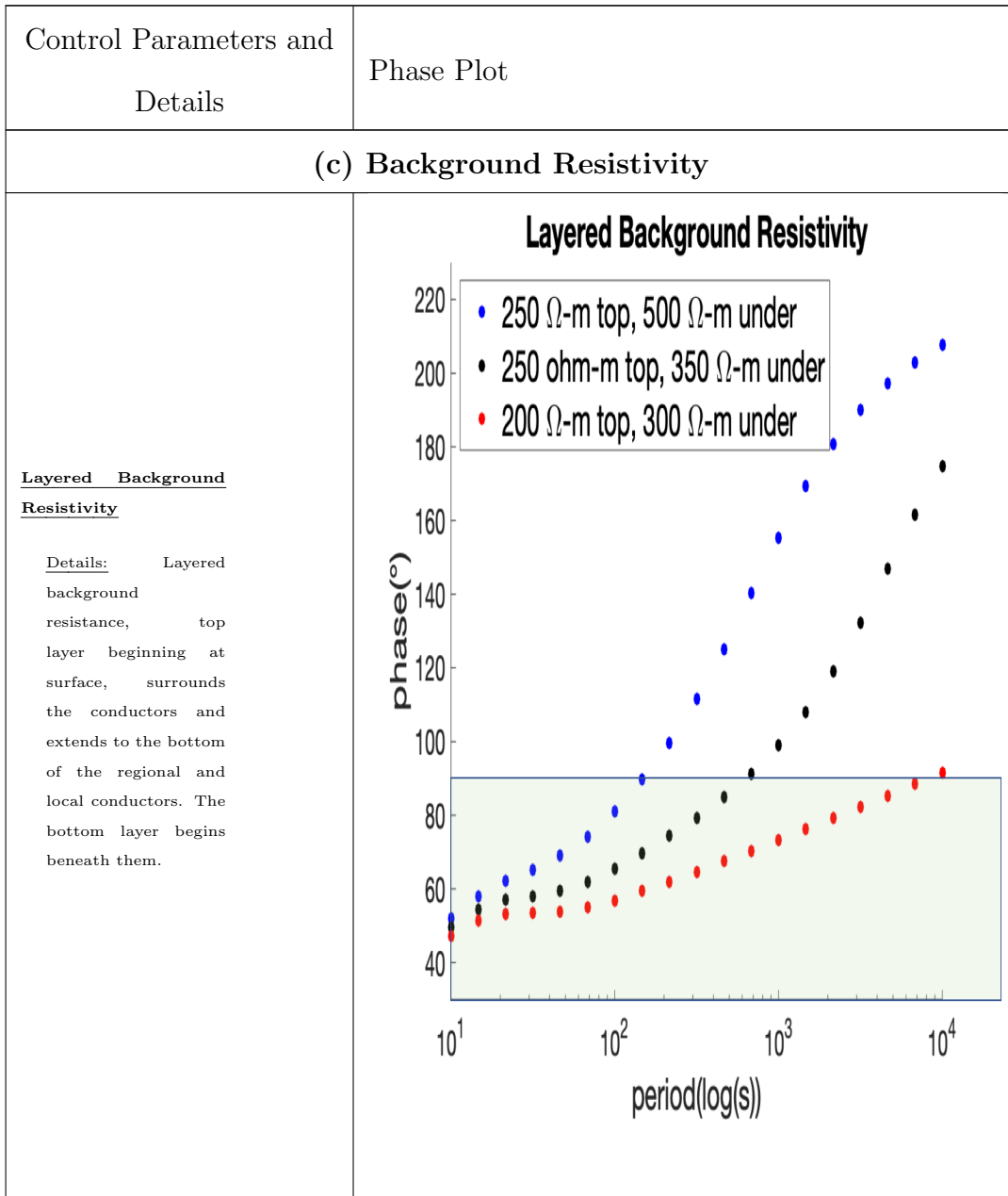


TABLE 4.1, continued

<p>Control Parameters and Details</p>	<p>Phase Plot</p>
<p><b>(d) Shape, Extent, and Placement of the Regional Conductor with Respect to the Local Conductor</b></p>	
<p><u>Regional Conductor Length</u></p> <p><u>Details:</u> Regional conductor length extended or reduced from the north end of the base model.</p> <p><u>Effects:</u> Phase tails disappear for conductors shorter than 100 km in length.</p>	<p style="text-align: center;"><b>Regional Conductor Length</b></p>
<p><u>Regional Conductor Extension Below Local Conductor</u></p> <p><u>Details:</u> Extending the length of the regional conductor below the local conductor, to the south.</p>	<p style="text-align: center;"><b>Regional Conductor Extension Below Local Conductor</b></p>



TABLE 4.1, continued

Control Parameters and Details	Phase Plot
<p><u>Regional Conductor Width</u></p> <p><u>Details:</u> Increasing or reducing the regional conductor width from comparison model's far right side.</p>	
<p><u>Regional and Local Conductor Depth Extent</u></p> <p><u>Details:</u> Thickness of local and regional conductors recorded in legend, all starting at a depth of 500 m.</p>	

TABLE 4.1, continued

Control Parameters and Details	Phase Plot
<b>(e) Shape and Extent of Local Conductor</b>	
<p><u>Local Conductor Length</u></p> <p><u>Details:</u> Local conductor length extended or reduced from the southern edge of the comparison models local conductor.</p>	<p style="text-align: center;"><b>Local Conductor Length</b></p>
<p><u>Local Conductor Width</u></p> <p><u>Details:</u> Local conductor width extended or reduced from the left edge of the comparison model's local conductor.</p>	<p style="text-align: center;"><b>Local Conductor Width</b></p>

TABLE 4.1, continued

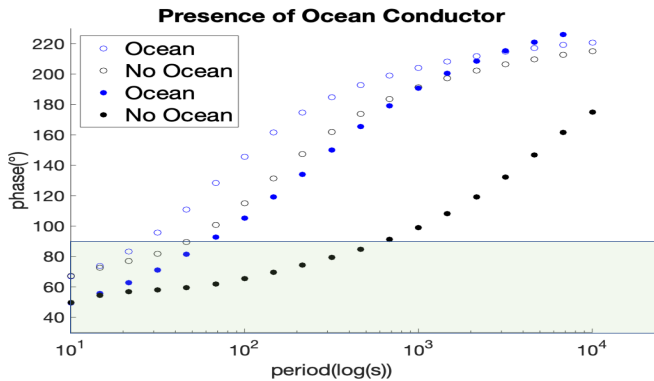
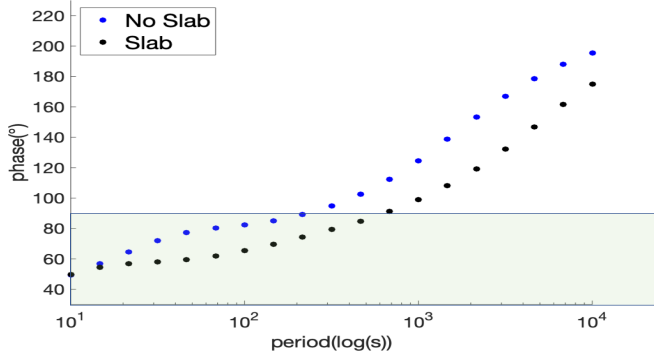
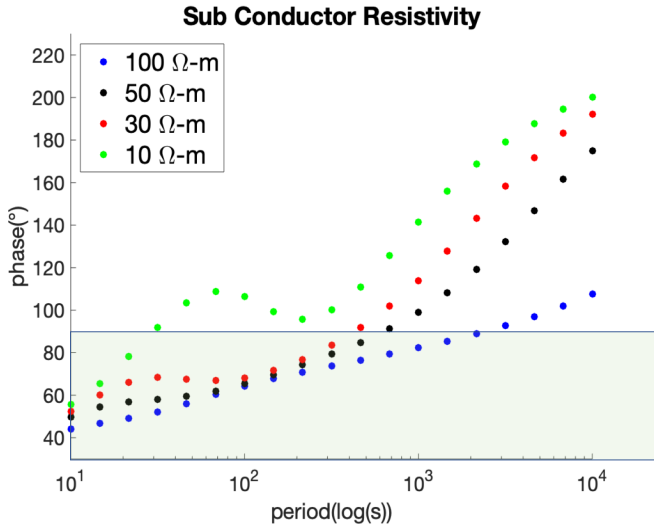
Control Parameters and Details	Phase Plot
(f) Ocean	
<p><b>*Presence of Ocean Conductor</b></p> <p><u>Details:</u> Blue dots show the presence of the ocean conductor located starting at the western edge of the model, extending in 25 km and going to a depth of .5 km of the model as in 4.2</p> <p><u>Details:</u> Solid dots indicate the presence of a 10 Ω-m surface conductor</p> <p><u>Details:</u> Plots without surface conductors are present here with open circles*</p>	 <p><b>Presence of Ocean Conductor</b></p> <p>Legend:   ○ Ocean (No Ocean)  ● Ocean (Ocean)  ● No Ocean</p> <p>The plot shows phase angle (°) on the y-axis (40 to 220) versus period (log(s)) on the x-axis (10<sup>1</sup> to 10<sup>4</sup>). A shaded region is present between 40° and 80°. Data points for 'Ocean' (blue) and 'No Ocean' (black) are shown, with open circles representing models without surface conductors.</p>
(g) Slab Resistor	
<p><b>Presence of Slab Resistor</b></p> <p><u>Details:</u> The resistor appears at a depth of 7 km on the left side of the model, and increases in thickness eastward, appearing at deeper depths, like a subducting slab. As shown in 4.2(structure D).</p>	 <p><b>Presence of Slab Resistor</b></p> <p>Legend:   ● No Slab  ● Slab</p> <p>The plot shows phase angle (°) on the y-axis (40 to 220) versus period (log(s)) on the x-axis (10<sup>1</sup> to 10<sup>4</sup>). A shaded region is present between 40° and 80°. Data points for 'Slab' (black) and 'No Slab' (blue) are shown.</p>

TABLE 4.1, continued

Control Parameters and Details	Phase Plot
<b>(h) Subconductor</b>	
<p><b><u>Subconductor</u></b></p> <p><b><u>Resistivity</u></b></p> <p><u>Details:</u> A conductor located directly below the sites near a depth of 6 km, extending to the slab resistor. Referred to in this thesis as a 'subconductor'</p> <p><u>Effects:</u> Phase tails disappear for models with subconductors that have greater resistivity than 100 <math>\Omega</math>-m.</p>	 <p>The figure is a scatter plot titled "Sub Conductor Resistivity". The y-axis is labeled "phase(°)" and ranges from 40 to 220 in increments of 20. The x-axis is labeled "period(log(s))" and is on a logarithmic scale from 10<sup>1</sup> to 10<sup>4</sup>. A legend in the top-left corner identifies four data series: 100 <math>\Omega</math>-m (blue dots), 50 <math>\Omega</math>-m (black dots), 30 <math>\Omega</math>-m (red dots), and 10 <math>\Omega</math>-m (green dots). The data points show a general upward trend in phase with increasing period. A light green shaded region highlights the area between approximately 40° and 90° phase. The 10 <math>\Omega</math>-m series (green) consistently shows the highest phase values, while the 100 <math>\Omega</math>-m series (blue) shows the lowest.</p>

Referred to here as a ‘surface’ conductor and depicted in Figure 4.2(3) F, the presence of conductive material beneath the sites, but above the intersection of the regional and local conductors, dramatically lowers the starting phase of a phase tail curve. As illustrated in table 4.1 (a), the more conductive a surface conductor, the lower the starting phase of the model. For a 200 to 350  $\Omega$ -m background resistivity and a 5-10  $\Omega$ -m regional conductor, the starting phase can vary between 60° and below 40°, depending on the conductivity and placement in depth of this near surface conductor. This upper layer conductivity seems to be one of the primary controls of a site’s starting phase, the phase for the first recorded period. The extension of the regional conductor below the local conductor from table 4.1 (d) and table 4.1 (h) the subconductor are the others, both described in greater detail below.

These variables do affect each other, the proper subconductor, surface conductor, and regional conductor extensions are needed to find a realistic starting phase that does not also have too small of a maximum phase. However, the starting phase is more sensitive to the surface conductor than these other controls. This sensitivity makes it the most direct control of the starting phase, with a of variation of 5-30  $\Omega$ -m accounting for over  $20^\circ$  of starting phase range. This lines up with expected phase behavior, phase as described by eq. 1.4, indicates the slope of a log-log plot of resistivity vs. period[21]. Sounding from a resistor into a conductor increases phase. Reducing the resistivity of a medium above a conductive body would lead to a reduced phase increase from the sounding. As the conductivity of the surface conductor is enhanced, the maximum phase for the longest periods goes down as well, causing a natural limit for the starting phase of a particular model. The thickness of the surface conductor also has an effect on the phase but not a very strong one. The thinner the surface conductor, the larger the starting phase becomes. Allowing the surface conductor to be in contact with the regional and local conductors minimizes the starting phase, but only by less than  $5^\circ$ , the resistivity of the conductor is more critical. This is likely to do with the fact that our starting period is 1 second, which is big enough that any gap between the surface conductor and the T-shaped conductors at this shallow of a depth would not be resolved by the EM wave. Recall that resolution in MT relates to skin depth (eq. 1.1), which at 1 second within a 10  $\Omega$ -m surface conductor is approximately 1.5 km. The surface conductor only exists within the first half a kilometer of our model, well within a 1.5 km skin depth. The overall shape of the phase curves for this control in table 4.1 don't change very noticeably with a change in resistivity of the surface conductor, just the locations of the starting and ending phase. The effect of the surface conductor has more to do

with the effects of the conductive medium on wave propagation directly under the sites than any direct current channeling effects around the model. This implies that a model, that has a tabular regional conductor with a low starting phase between  $40^\circ$  and  $50^\circ$  on a phase plot, indicates the presence of a conductive body directly under the site in question.

The conductivity contrast between the regional and local conductors(table 4.1 (b)) and between the conductors and the surrounding background material(table 4.1 (c)) controls the value of the phase tail maximum and the slope of the out of quadrant roll out in the phase plots. Garambois et al. [65] suggests that the near-surface crust has a conductance closer to  $250 \Omega\text{-m}$ , so that is the value we use for the top layer of the background resistivity in the comparison model. Using previous inversions [[22]; [34]; [35]] as a guide, we know that material immediately surrounding large tabular conductors can be more conductive than this. Additionally, USGS maps show surface outcrops of limestone and a mix of sandstone and siltstone around phase tail-impacted sites, so a range of about  $150$  to  $300 \Omega\text{-m}$  was considered reasonable for the surrounding resistive background. These more resistive background values allowed a more resistive regional conductor to generate phase tails. A background resistivity lower than around  $150 \Omega\text{-m}$  limits the regional conductor to have unphysical resistances of  $3\Omega\text{-m}$  or lower. The USGS maps(Figure 4.3) and geologic literature show that the most likely naturally-occurring materials, extrapolating from the presence of near surface materials, that could form structures large enough to be considered regional conductors, and located near the phase tail sites, consist of a mix of sandstone and siltstone, shales, or reservoirs [[65]; [62]]. A lower limit on reasonable resistivities for these materials is  $5 \Omega\text{-m}$  , but through forward modeling we discovered that  $12 \Omega\text{-m}$  is the limit for a  $150\text{-}300 \Omega\text{-m}$

background resistivity to generate phase tail behavior. An important caveat is that, in order to generate phase tail-like behavior for regional conductor resistivities greater than 5 or 6  $\Omega\text{-m}$ , the surface conductor must be absent or resistive enough to result in a starting phase higher than  $60^\circ$ . The MT data (Figure 4.1) taken from physical sites suggests that modeling a starting phase that high is an unrealistic constraint on the model. With this in mind table 4.1 (b) does not include a surface conductor in the comparison model, in order to illustrate the range of control that the resistivity of the regional conductor can have on a phase tail plot.

The resistivity of the local conductor works similarly to that of the regional. The same material candidates for regional conductors can also fill the role of local conductor. More conductive materials, originally discussed in the previous section, such as saline reservoirs, mineralized zones (e.g., massive sulfides) now become more viable since the local conductors do not require as much material. Taking these previously unsuitable geological materials into account, a reasonable range of resistivities for a local conductor in Cascadia becomes roughly .03 to 10  $\Omega\text{-m}$  [[65]; [59]]. This range depends on the value of the regional conductor, phase tails do not form if the local and regional conductors are the same unless they both possess high conductivities, lower than approximately 1  $\Omega\text{-m}$ , which is geologically unfeasible for Cascadia. A more geologically plausible conductivity of 5  $\Omega\text{-m}$  ([65]) for the regional conductor allows for a range of local conductor resistivities between .3 $\Omega\text{-m}$  and 2 $\Omega\text{-m}$ , as shown in table 4.1 (b). According to our models analysis, this conductivity range of a 1  $\Omega\text{-m}$  change in local conductivity can control 20-40 degrees of max phase. The max phase decreases as the local resistivity increases, going below 90 degrees close to 3  $\Omega\text{-m}$  for the geologically realistic resistivity of the comparison models regional conductor. For a regional conductor of resistivity 10-12  $\Omega\text{-m}$  the local conductor

can only have a resistivity of up to 5  $\Omega$ -m. This suggests that, within the realm of realistic local and regional conductor resistivity values, the local conductor can only have a resistivity value as high as about half of the resistivity of the regional conductor. This conductivity contrast between the regional and local conductors would introduce another boundary condition to the model. The current flowing from the local conductor into the regional must stay continuous, this would lead to the presence of more boundary charge to the system[50]. This boundary charge would be located near the elbow created by the regional and local conductors where the phase tail effect occurs, it is plausible that this additional boundary charge further starves the regional conductor of current.

In order to have phase tails simulated from models with background resistivities less than 1000  $\Omega$ -m and geologically feasible regional conductor values, around 5  $\Omega$ -m, there must be a difference in resistivity values between the resistive background layer containing the regional and local conductor and the resistive background layer under this composite structure. This layered background structure is illustrated in 4.2. The layered background resistivity approach allows for a geologically reasonable 250  $\Omega$ -m ([65]) value around the T-shaped conductor. Through studies by Garambois et al. [65], Evans et al. [34], Wannamaker et al. [35], and many others we know that the earth's crust gets more resistive with depth, even in transition from 3-20 km depth. We used different conductivities for the background resistivity surrounding the regional and local conductors and the background resistivity directly under those conductors. We chose the range for the deeper layer of resistive background under the regional and local conductors to be between 250-500  $\Omega$ -m ; the main reason for this is that the surrounding crust in Cascadia should be more conductive than the subducting slab, yet more resistive than the shallower crust. This likely has



to do with current channelling, as discussed previously currents can be induced in to the system from the ‘other’ mode, the mode not exhibiting phase tail behavior [24]. This induced current is channelled into the system by bound charge located along stark conductivity boundaries. Egbert [24] alludes to the presence of these currents as essential to the build up of enough current in the geological system to generate phase tail behavior. Charge will flow toward more conductive features, if able, including any located below the T-shaped conductor [50]. A more resistive background layer(4.2(1)C2) below the T-shaped conductor will insulate the system from any conductive features(‘subconductors’) located deeper in the model. More current will be present around the T-shaped conductor rather than escaping toward any deeper ‘subconductors’ [50]. This interpretation is supported by table 4.1c which shows that the higher the resistivity of the lower background layer, the higher the maximum phase of the model.

Table 4.1d shows two opposing behaviors regarding the length of the regional conductor. Extending the length of the regional conductor from the northern edge of the comparison model (Figure 4.2) increases the maximum phase of the model and causes the phase to roll out of quadrant at an earlier period. In contrast, extending the length of the regional conductor from the south end of the comparison model decreases the maximum phase of the model, causes the phase to roll out of quadrant at a later period, and decreases the starting phase of the model. In making this comparison, regardless of which edge the regional conductor was extended from, the local conductor stayed in the same spot. Flipping which side of the T-shaped conductor that has the longer regional conductor section, simply flips which side of the local conductor the phase tail behavior occurs. The ratio between the lengths of the regional conductor on either side, north or south, of the local conductor appears

to be the relevant variable, with phase tails only appearing on the side of the local conductor with the longer portion of regional conductor. This may have to do with the nature of current channeling, both sides of the T-shaped conductor are competing for a finite amount of charge [50]. The longer section of the regional conductor is more current starved than the shorter section, and so the 'elbow' between the long regional conductor segment and local conductor on that side see phase tail effects.

Table 4.1d shows that the width of the regional conductor and the thickness of the entire T-shaped conductor affect the phase of the model in similar ways. Increasing the width of the regional conductor increases the maximum phase of the model and causes the period with which the phase rolls out of quadrant to decrease. Likewise, increasing the thickness of the local and regional conductors led to the same behavior in the phase. This is likely due to the fact that increasing the size of the conductors in thickness or width adds more conductive material to the system, there is more current flowing through the conductor. Increasing the width or thickness of the regional conductor, increases the cross-sectional area of the ends of the conductor. Wider conductor ends allow more current to flow through them [50], the conductor being analogous to a wide wire. The larger ends of this conductor likely act as a bigger source for the current starvation effect discussed above.

The local conductor has a unique response to altering its shape. Table 4.1 (e) shows that decreasing the length of the local conductor from its southern edge increases the maximum phase, and causes the period with which the phase rolls out of quadrant to decrease. The phase maximum of the blue 4km line shows the beginning of a plateau, this could hint at a possible saturation effect, where the increase of the maximum phase reduces as the local conductor decreases in length until the local conductor disappears and no phase tails are present. This is odd, because it suggests

that for the x direction having less conductive material excites the phase tail effect, which is the opposite of how the regional conductor appears to work. It is likely that the increased proximity of the two ‘elbows’ formed on either side of the local/regional conductor intersection has something to do with this. Current induced in the elbow on the smaller regional conductor side of the T-shaped conductor may more easily contribute to the phase tail effect in the elbow of the side of the T-shaped conductor with the larger regional conductor section. Table 4.1 (e) shows that decreasing or increasing the width of the local conductor from 8km by 4km, decreases the maximum phase and increases the period with which the phase rolls out of quadrant, in the case of 4.1 (e) to a period beyond the scope of the model leading to no phase tail. This is the only control where increasing or decreasing it has the same effect. This implies that the proximity of the site to the location of the outer edges of the local conductor on the far west side has significance. It is possible that having this boundary farther away from the regional conductor interferes with the current channeling needed for phase tail phenomena. This edge likely acts as a source for boundary charge in the system ([55]), the farther it is from the crook of the conductor elbow of the T-shaped conductor the less this source can contribute to the phase tail effect.

Insertion of an ocean conductor(table 4.1(f)) as shown in Figure 4.2 (3) G, causes a marked increase in both the amount of phase tail behavior present in the model sites and an increase in the intensity of the phase tail plots. The conductor extends from the far west side of the model for 25km and has a thickness of .5 km. This conductor is meant to model the presence of nearby ocean, but does not connect to the regional or local conductors, unlike in the case of Lezaeta and Haak [52]. We chose not to connect the ocean to any other conductors to increase authenticity, our models(Figure 4.6 show that most of the MOCHA phase tail sites are not near

any shallow conductors in contact with the ocean. The ocean acts to excite current channeling throughout the entire system [52]. Table 4.1(f) suggests that a phase tail site near the ocean would require an increased amount of phase dampening knobs in order to replicate a realistic phase tail graph, such as those in Figure 4.1. The ocean conductor, has been one of the most difficult variables to work with, its presence causes the maximum phase of the system to increase to very high values compared to the models without an ocean conductor. This will be discussed further in the summary and further work section (section 4.4).

The presence of conductive or resistive features below, but not in contact with, the local and regional conductors control the starting phase, ending phase, and for which periods a phase plot plateaus before beginning to exponentially increase in phase. Referred to as "subconductors" in table4.1(h) and "slab resistors" in table4.1(g) they act as further boundary conditions for the system as well as an additional factor to enhance or diminish 'current starvation' in the system.

The 'subconductors' are built to represent the conductive geological features that exist near the mantle wedge corner, and elsewhere just above the subducting slab as discussed in Chapter II of this dissertation. They are of specific interest to the geophysical study of the Cascadian subduction zone and have a significant impact on phase tail effects, as shown in table4.1(g), it is important to account for their presence. Without this feature present, the conductivity contrast between a realistically resistive crust and the L shaped conductor required for phase tail behavior demands an unrealistically low resistivity for the regional conductor,  $3 \Omega\text{-m}$  or lower. Table 4.1, shows that this is one of the controls, other than the regional conductor length, that primarily determines for how many periods the phase stays constant, or plateaus over, before rolling out of quadrant into phase tail like behavior.

We speculate that this is related to the depths to the centers of these conductors, between 6km and 40 km deep primarily effect the middle range of periods used in this paper. The skin depth equation(eq.1.1) that governs the resolution of MT, dictates that longer periods are more sensitive to features at greater depth. As stated previously, this is one of the few features that controls the starting phase of a model, like the surface conductor feature previously discussed, but it works the opposite way, the more resistive the subconductor the lower the starting and ending phase of a particular site. We speculate that this works similarly to the ocean conductor, the presence of a conductive body allows more induced current to be channelled into the regional, local conductor system [24]. In addition, more boundary charge is introduced near the system by EM fields entering the subconductor, adding another source for current starvation effects near the regional, local conductor system [55]. In contrast the slab resistor(table4.1(g)) dampens the phase tail effect, it leads to decreased phase for higher periods. Current will not as easily flow through such a resistive body, reducing any contributions to the current channeling that a more conductive structure would have introduced to the system [50].

### **4.3 Results and Discussion**

After discovering how each specific control altered the phase tail curves of our model, we are now able to attempt to mimic the phase tail behavior exhibited by the MOCHA sites. A difficult factor in trying to replicate realistic phase tail curves through forward modeling is that the controls affect one another and often multiple aspects of a models phase curve. For example, most of the control knobs listed in table4.1 control the maximum phase of a phase tail curve in addition to other

effects. As these effects stack, using too many controls that reduce the phase can get rid of the phase tail effect entirely. A useful strategy is to introduce controls that primarily only increase the maximum phase of the phase tail plot, such as extending the length of the regional conductor to the north(table4.1 (d)), the depth of the T-shaped conductor(table4.1 (d)), or the resistivity of the local conductor (table4.1 (b)) so that other controls can be used to better customize the phase curve without negating the phase tail effect.

Early on we discovered that the primary controls on the starting phase of a model were the resistivities of the surface conductor (table4.1 (a)) and the subconductor (table4.1 (h)). Recall that the resistivity of the subconductor also controls how flat or ‘plateaued’ a phase tail graph is in the early periods before they begin to more rapidly rise out of quadrant. Since decreasing the resistivity of the subconductor both decreases the starting phase and reduces this plateau effect, relying on the subconductor resistivity as the primary control of starting phase can lead to unrealistic early period phase plateaus. The surface conductor became the primary control for the starting phase of the model. While troubleshooting for ideal models to mimic phase tail sites, once the subconductor had a resistivity that produced a desirable phase plateau effect, it’s resistivity would remain unchanged, usually around 100  $\Omega$ -m.

The surface geological structure hosting station MC13 is shown in Figure 4.3. Phase plots for this station are shown in Figure 4.1, and is typical for MOCHA sites evincing phase tail behaviors, for example, a shorter-period plateau, a low starting phase between 30 and 50 degrees, and a maximum phase under 150 degrees. Figure 4.7 shows a phase plot comparison of the best attempt to model the phase data of MC13(blue) compared to that of MC13. This suggests that MC13 is located

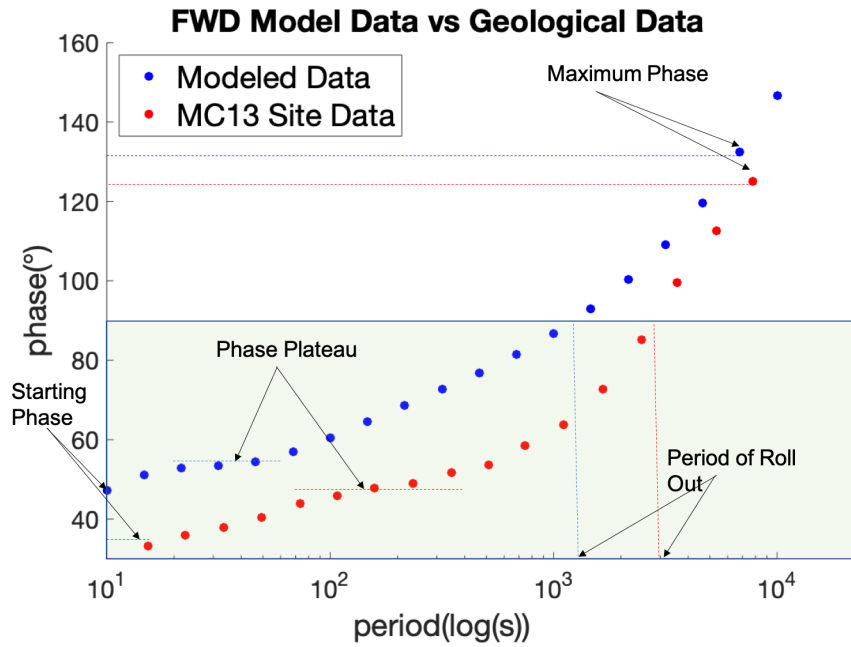


FIGURE 4.7. This plot compares the phase plot of station MC013 from the MOCHA Array to one of our most promising models. The green area highlights phases from 0 to 90 degrees. The Model is a variant of the comparison model used in table 4.1, with the following changes: it has a 200  $\Omega$ -m top layer background resistivity and a 300  $\Omega$ -m second layer background resistivity, the local conductor has a resistivity of 2  $\Omega$ -m, and the regional conductor is extended to the north by 50 km.

near a surface conductor with resistivity lower than 5  $\Omega$ -m, or a regional conductor extending asymmetrically on the opposite side of a local conductor by an extra fifth of the entire regional conductor length. In table 4.1 (d) the one fifth regional conductor extension was the extension that led to the lowest starting phase. Alternately, placing constraints on the size and shape of the local conductor is more difficult because it is likely that several combinations of regional and local conductor sizes could be used to help create a phase tail plot with the proper maximum phase. This model from Figure 4.7 extended the comparison model of 4.1 by 50 km to help generate an appropriately high enough maximum phase to counteract the dampening of the phase tail effect brought on by a reduced background resistivity and a reduced surface conductor resistivity. The two phase plots share similar shapes below  $10^3$  seconds, suggesting that a subconductor is likely present with a resistivity value around 50  $\Omega$ -m. Relatedly, a 200  $\Omega$ -m top background resistivity layer (Figure 4.2 (2) C1) with a 300  $\Omega$ -m bottom background resistivity layer (Figure 4.2 (2) C2) allowed the modeled phase to best match, on average, the slope of the phase curves for phase tails present in the MT data. Our inversion of Cascadia shown in Figure 4.6 shows that a surrounding background resistivity of 200  $\Omega$ -m is reasonable for this station. The inversion also agrees with a 300  $\Omega$ -m background resistivity deeper in the model. The background resistivity is important because as noted in equation 4.4, current starvation effects require an induction length greater than the length of the regional conductor. This can only happen if the background resistivity within the elbow of the T-shaped conductor is large enough.

The attempt to recreate the phase tail curve of MC13 alludes to some clues that could improve the process of inverting phase tail sites. As discussed in Chapter II, MT is better at resolving conductance than conductivity. It is also better at



resolving the tops of conductors but is less able to accurately determine the tradeoff between conductivity and thickness below this. The local conductors seem to be approximately the same size as a typical model cell (8km  $\times$  8km), so depending on model smoothing, features important for phase tail effects, like conductor thickness and the location of local conductors can be estimated incorrectly by the inversion. With MT it is a common practice to engage in hypothesis testing, where the resistivity of a cell or group of cells is given a specific value and either locked to that value, or incentivized to stay within a specific range of it, using smoothing constraints [21]. Inversion run with and without these cell 'freezing' techniques are trialed and tested for significant variations in achieved RMS misfit reduction. This tool can be used to impose conditions that the forward models suggest generate the observed phase tail behavior, with the hope that these imposed features will improve model fit, such as the background resistivity of the model block under the site, the estimated location of a local conductor, or the thickness and conductivity of an estimated surface conductor or subconductor feature.

#### 4.4 Summary and Future Work

Throughout this chapter I have described how an overabundance of free boundary charge is introduced into the system through current conservation and EM boundary conditions on electric fields normal to planar boundaries between large contrasts in resistivity [[50]; [24]]. This boundary charge and conductivity contrast between large tabular conductors and their surrounding background resistivity leads to a current starvation effect brought on when the induction scale length of the system (equation 4.4) generally exceeds the length of the tabular regional conductor[

[55];[24]]. This current starvation effect can lead to the scavaging of currents induced by the other, horizontally-orthogonal MT source field, leading to phase tail effects [24]. To discover what parameters were the most important for controlling phase tail behavior a series of forward models were run to discover a list of ‘knobs’ or controls that could be used to more accurately reproduce the phase tail curves seen in MT data(table4.1). Once this list of controls was generated, they were used to generate a model to match the phase behavior of site MC13 to see what reasonable geological features should be expected around the site to generate its observed phase tail behavior (Figure 4.7). The insight learned from this forward modeling exercise will be used to impose conductive features into an inversions starting model to see if phase tail sites could be inverted more accurately.

A control that would benefit from further exploration is the conductive ocean. In explorations using forward modeling with the T-structure and other model features, it proved to be a difficult knob to control. It frequently led to unnaturally high phase tail maximums, decreased early period phase plateaus, and an overly-steep out of quadrant phase roll out in the later periods. Different extents and depth of conductive ocean conductors should be explored with various phase tail maximum dampening controls, such as conductive surface conductor and resistive subconductors, to see if the ocean can be more accurately included in the forward models. Lezaeta and Haak [52] discuss how ocean structures can enhance the distortion of H-fields, introducing a change to a variable that the phase is dependent upon(eq. 1.4). Additionally, there are other phase tail site characteristics than those noted for MC13,, recreating some of them would lead to further insight about phase tails.

## CHAPTER V

### REFLECTION

Engaging in the work described in this dissertation has been one of the most meaningful experiences of my life. I have had the opportunity to engage with brilliant minds, see places I would never have had the opportunity to visit otherwise, such as a research vessel traveling along the Pacific coast to collect ocean-bottom seismometers, San Diego, San Francisco, Thailand, Denmark, and several very densely-packed old growth forests. I have spoken at several conferences and had the good fortune of being able to develop my teaching skills along the way.

I was given the opportunity to delve into the fields of geophysics and geology for the first time through the MOCHA experiment. I learned a lot of new material. Through my efforts described in chapter II I was able to contribute my own insights into the story of Cascadia and ETS. Our MOCHA collaboration has focused primarily on fluid roles along the crust-slab interface up-dip of the mantle-wedge corner (MWC), while I've concentrated on analysis of fluids near the MWC and ETS occurrence. I included some discussion on those features updip of the MWC but wandered a bit eastward with my application of Nakajima and Hasegawa's ([17]) take on the relationship between fluids escaping from a plate interface and ETS tremor occurrence. I wondered if Farallon asthenosphere remnants forming blocks within the Siletzian crust bounded by deeply-penetrating faults, as discussed by Wells et al. ([18]) would provide a mechanism for fluid egress through the crust that serves to suppress ETS occurrence, while the MOCHA collaboration focused, instead, on explanations relying on changes in physical properties of the overlying crust up-dip of the MWC to explain latitudinal variations in ETS. This led me to try my cross correlation analysis discussed in the methods section of chapter II.

The work was often challenging, particularly the interpolation work described in chapter III. The modifications required me to pick up quite a few new skills, object oriented programming being one of them. Truth be told there is a lot of work still needed to be done on this front, but the architecture has now been built, and the basic structure for the new added interpolation methods appears to work in a simplified setting. It needs to be built into the full version of ModEM3D, and needs to be applied to a more complicated bathymetry or tomography than the test cases I have been using.

The work described in chapter IV gave me the opportunity to work on a problem that has been vexing scientists in the field of magnetotellurics for some time. This is a problem that my own advisor, Dean Livelybrooks, worked on during the start of his post Ph.D career [51]. I was ultimately able to recreate some of the phase tail data present in the MOCHA data set. I documented some key controls that determine the shape and magnitude of phase tail behavior, that can be used to predict what type of geologically-plausible features are most likely present when observing a particular type of phase tail behavior. Examples include the depth of a surface conductor or the likely resistivity range of the values of the surrounding background. Using these new insights to improve an inversion has been challenging. I have run quite a few inversions that were predisposed with structures based on my forward models. So far I have been unsuccessful, but my attempts continue to guide me forward. Inversions take a long time to run, usually about a week, so progress with them can be slow.

The work in this thesis will continue to be developed. Chapters II and IV have been written to be readily adapted to article submissions, likely to *Geophysical Journal International* or the *Journal of Geophysical Research*. The work in chapter III will be passed on to other graduate students, and hopefully further developed.

## APPENDIX

### GLOSSARY OF TERMS

A brief glossary of terms used in this dissertation. See the dissertation itself for a more in depth discussion of these terms.

Accretionary Wedge: The most distal forarc feature of a continental plate going through subduction, the part that protrudes the furthest before meeting an Oceanic Plate. This wedge buckles as subduction goes on.

Anisotropy: A physical property of a material where a parameter, in this case electric resistivity, varies depending on what direction a wave travels through it.

Cascadia Subduction Zone: A spreading center, where new crust is formed off the Pacific coast of North America. The Juan de Fuca Oceanic Plate subducts under the less dense North American Continental Plate.

Conductance: The conductivity thickness product integrated over a specific distance. It more accurately reflects fluid distributions than conductivity.

Crescent Terrane: The segment of Siletzia comprising the Olympic Peninsula, and underlain by the Crescent formation.

Crust: The upper most layer of the Earth. Located above the mantle.

Episodic Tremor and Slip (ETS): Seismic events correspond with the occurrence of swarms of low-frequency tremor that occur every 11-22 months depending on location [13]. These events correspond with a small updip slip along the plate interface, releasing the same amount of energy as a magnitude 6 or 7 earthquake, but over the span of 10-14 days rather than the few minutes of a typical earthquake [14]. The

danger and interest in these events resides in the fact that they have been observed prior to large scale events [15].

Farallon Subduction Zone: A previously existing subduction zone, where the old Farallon plate subducted under the North American Plate, its remnants form modern day Siletzia.

Finite Difference Method: A computational modeling technique involving a grid where variables, in this case electromagnetic fields stored in near by grid cells are used to solve equations, in this case Maxwell's Equations, at each cell.

Forarc Mantle Wedge Corner (MWC): Where the subducting oceanic plate meets the Mohorovic Discontinuity (Moho).

Greenschist Facies: A metamorphic facie involving clays.

Inversion: An iterative computational modeling technique, used to create conductivity models from Magnetotelluric data.

Klamath Mt Terrane: A Terran located directly south of Siletzia, bordered by the Wildlife Safari Fault.

Locked Zone: The location between two subducting plates, where the plates are physically locked together and move together. Seismic. Stress builds up here over time.

Magnetotellurics: A geological observation technique that uses electromagnetic waves generated within the Earth's ionosphere and by thunderstorms as probes in order to generate conductivity maps of the Earth's interior in three dimensions.

Mantle: The layer of the Earth directly below the crust.

Megathrust Earthquakes: A large scale earthquake that occurs when two subducting plates buckle and slip rapidly along their common interface, known as a thrust surface.

Metamorphic Facies: Hydration reactions store water metamorphically within these clusters of rock types known as mineral facies. Under the right pressure and temperature, the fluid is released through dehydration reactions.

Magnetotelluric Observations of Cascadia using a Huge Array (MOCHA): One of the world's first 'amphibious 3-D' surveys, began with the acquisition of 173 stations, 102 onshore stations and 71 offshore stations, from a large, nominally rectangular array of stations spaced and average of 25 kilometers apart. The array provided amphibious data useful for imaging subducted fluids from trench to mantle wedge corner (MWC).

Mohorovic Discontinuity (Moho): The seismically-defined boundary surface between the continental crust and the mantle.

Phase Tail: A term this work uses to define anomalous phase behavior where the phase of a magnetotelluric station reaches values above 90 degrees for long periods, known as going out of quadrant.

QR Decomposition: A least squared solution method for solving an over determined system.

Remote Referencing: A filtering technique in magnetotellurics that uses nearby stations as reference points for each frequency, to reduce the effect of outside noise on the data using coherence testing.

Serpentinite: A metamorphic rock present in dehydration reactions along the Cascadian Subduction Zone.

Siletzia: A terrane formed from the remnants of the Farallon subduction zone. It runs along Pacific Northwest, terminating at the Wildlife Safari Fault.

Siletz Terrane: The southern segment of the Siletzia Terrane encompassing most of Oregon.

Singular-Value Decomposition (SVD): A solution technique involving the factorization of a complex matrix using a form of eigen decomposition. It is often used to define a plane.

Smoothing: A technique used to compensate for the non uniqueness of solutions stemming from the magnetotelluric inversion problem. Smoothing prioritizes models that minimize strong conductivity contrasts, hoping to prioritize realistic geological behavior.

Source Polarizations: Magnetotellurics has two primary source polarizations, the  $H_x$  and  $H_y$  polarizations. These are the primary polarizations that result from the natural polarization of electromagnetic waves traveling into the Earth.

Spreading center: An area where new oceanic crust is formed, from magma from the upper mantle rising up through a crack formed by two moving plates.

Subduction Zone: A spreading center, a region where new oceanic crust is formed, moves relatively landward, plows below (subducts) less dense continental crust, and eventually sinks deep enough to contribute to magmas forming volcanoes.

Terrane: A fragment of a previously existing plate that has been accreted or otherwise attached onto another geological plate. Siletzia is an example, it was formerly a fragment of the Farallon plate that is now attached to the North American plate.

Yee Grid: A way of formatting a grid used in the finite difference method where solutions are stored at the edge and face centers of a grid.



## REFERENCES CITED

- [1] F. Press and R. Siever, *Earth*, 4th ed. (W.H. Freeman and Company, San Francisco, 1985).
- [2] G. Rogers and H. Dragert, *Science* **300**, 1942 (2003).
- [3] Y. Furukawa, *Tectonophysics* **469**, 85 (2009).
- [4] G. D. Naidu, in *Deep Crustal Structure of the Son?Narmada?Tapti Lineament, 13 Central India, Springer Theses* (Springer, Berlin Heidelberg, 2012) Chap. 2, pp. 13–35.
- [5] A. Kelbert, N. Meqbel, G. D. Egbert, and K. Tandon, *Computers & Geosciences* **66**, 40 (2014).
- [6] K. J. Walowski, P. J. Wallace, E. H. Hauri, I. Wada, and M. A. Clynne, *Nature Geoscience* **8**, 404 (2015).
- [7] M. G. Bostock, N. I. Christensen, and S. M. Peacock, *Seismicity in Cascadia* **332-333**, 55 (2019).
- [8] S. M. Peacock, *Geological Society of America* **29**, 299 (2001).
- [9] J. P. Canales, S. M. Carbotte, M. R. Nedimovi, and H. Carton, *NATURE GEOSCIENCE* **10**, 864 (2017).
- [10] M. B. Underwood, *Geology* **30**, 155 (2002).
- [11] S. Han, N. L. Bangs, S. M. Carbotte, D. M. Saffer, and J. C. Gibson, *NATURE GEOSCIENCE* **10**, 954 (2017).
- [12] S. M. Peacock, *Journal of Geophysical Research* **114**, B00A07 (2009).
- [13] M. R. Brudzinski and R. M. Allen, *Geophysics* **37**, 98 (2007).
- [14] R. D. Krogstad, D. A. Schmidt, R. J. Weldon, and R. J. Burgette, *Earth and Planetary Science letters* **439**, 109 (2016).
- [15] G. C. Beroza and S. Ide, *Annual Review of Earth and Planetary Sciences* **39**, 271 (2011).
- [16] R. D. Hyndman, P. A. McCrory, A. Wech, H. Kao, and J. Ague, *Journal of Geophysical Research: Solid Earth* **120**, 4344 (2015).
- [17] J. Nakajima and A. Hasegawa, *Nature Communications* **7**, 13863 (2016).

- [18] R. Wells, D. Bukry, R. Friedman, D. Pyle, R. Duncan, P. Haeussler, and J. Wooden, *Geosphere* **10**, 692 (2014).
- [19] G. M. Schmalzle, R. McCaffrey, and K. C. Creager, *Geochemistry, Geophysics, Geosystems* **15**, 1515 (2014).
- [20] G. M. Schmalzle, R. McCaffrey, and K. C. Creager, *Earth and Planetary Science Letters* **304**, 202 (2011).
- [21] M. N. Berdichevsky and V. I. Dmitriev, *Models and Methods of Magnetotellurics*, 1st ed. (Springer, Berlin, 2008).
- [22] B. Yang, P. A. Bedrosian, G. Egbert, K. Key, D. Livelybrooks, B. Parris, and A. Shultz, (2020).
- [23] G. D. Egbert, *Surveys in Geophysics* **23**, 207 (2002).
- [24] G. D. Egbert, *Geophys Journal International* **102**, 1 (1990).
- [25] T. D. Gamble, W. M. Goubau, and J. Clarke, *GEOPHYSICS* **44**, 53 (1979).
- [26] S. C. Constable, R. L. Parker, and C. G. Constable, *Geophysics* **52**, 289 (1987).
- [27] W. Siripunvaraporn and G. D. Egbert, *Physics of the Earth and Planetary Interiors* **173**, 317 (2009).
- [28] G. D. Egbert and A. Kelbert, *Surveys in Geophysics* **189**, 251 (2011).
- [29] W. Siripunvaraporna, G. Egbert, Y. Lenburyc, and M. Uyeshimad, *Physics of the Earth and Planetary Interiors* **150**, 3 (2005).
- [30] D. V. Shantsev and F. A. Maa, *Geophysical Journal International* **200**, 745 (2015).
- [31] W. Soyer and M. Unsworth, *Geology* **34**, 53 (2006).
- [32] R. S. McGary, R. L. Evans, P. E. Wannamaker, J. Elsenbeck, and S. Rondenay, *Nature* **511**, 338 (2014).
- [33] P. Wannamaker, J. Booker, J. Filloux, A. Jones, G. Jiracek, A. Chave, P. Tarits, H. Waff, G. Egbert, C. Young, J. Stodt, M. Martinez, L. Law, T. Yukutake, J. Segawa, A. White, and A. Green, *Geochemistry, Geophysics, Geosystems* **94**, 14111 (1989).
- [34] R. L. Evans, P. E. Wannamaker, S. McGary, and J. Elsenbeck, *Earth and Planetary Science Letters* **402**, 265 (2014).
- [35] P. E. Wannamaker, R. L. Evans, P. A. Bedrosian, M. J. Unsworth, V. Maris, and R. S. McGary, *Geochemistry, Geophysics, Geosystems* **15**, 4230 (2014).

- [36] C. Aprea, M. Unsworth, and JohnBooker, *Geophysical Research Letters* **25**, 109 (1998).
- [37] P. A. Bedrosian and S. E. Box, Paper presented at American Geophysical Union Fall Meeting 2006 abstract id. T43C-1649 **39** (2006).
- [38] N. M. Meqbel, G. D. Egbert, P. E. Wannamaker, A. Kelbert, and A. Schultz, *Earth and Planetary Science Letters* **402**, 290 (2014).
- [39] A. Levander and M. S. Miller, *Geochemistry Geophysics Geosystems* **13**, Q0AK07 (2012).
- [40] P. A. McCrory, J. L. Blair, F. Waldhauser, and D. H. Oppenheimer, *JOURNAL OF GEOPHYSICAL RESEARCH* **117**, B09306 (2012).
- [41] P. W. J. Glover, *Geophysics* **75**, E247 (2010).
- [42] R. E. Wells, C. S. Weaver, , and R. J. Blakely, *Geology* **26**, 759 (1998).
- [43] J. R. Delph, A. Levander, and F. Niu, *Geophysical Research Letters* **45**, 11021 (2018).
- [44] R. E. Wells, R. J. Blakely, A. G. Wech, P. A. McCrory, and A. Michael, *Geology* **45**, 515 (2017).
- [45] K. Creager, C. Ulberg, P. Bodin, S. Malone, J. Gomberg, K. Marczewski, J. Connolly, and N. Chow, Tremor map, <https://pnsn.org/tremor>.
- [46] S. M. Peacock, *Science* **248**, 329 (1990).
- [47] E. M. Baldwin and R. K. Perttu, *Oregon Geology* **51**, 2 (1989).
- [48] K. Hall, D. Schmidt, and H. Houston, *Geochemistry, Geophysics, Geosystems* **20**, 4665 (2019).
- [49] K. Hall, D. Schmidt, and H. Houston, *Geochemistry, Geophysics, Geosystems* **19**, 2706 (2018).
- [50] D. J. Griffiths, *Introduction to Electrodynamics*, 3rd ed. (Prentice-Hall, New Jersey, 1999).
- [51] D. Livelybrooks, M. Mareschalt, E. Blais, and J. T. Smith, *GEOPHYSICS* **61**, 971 (1996).
- [52] P. Lezaeta and V. Haak, *JOURNAL OF GEOPHYSICAL RESEARCH* **108**, 2305 (2003).
- [53] W. Heise and J. Pous, *Geophysical Journal International* **105**, 308 (2003).

- [54] Q. Xiao, G. Shao, G. Yu, J. Cai, and J. Wang, *Physics of the Earth and Planetary Interiors* **255**, 1 (2016).
- [55] P. E. Wannamaker, G. W. Hohmannl, and S. H. Ward, *GEOPHYSICS* **49**, 1517 (1984).
- [56] J. T. Smith, *Geophysical Journal International* **130**, 65 (1997).
- [57] H. Ichihara and T. Mogi, *Geophysical Journal International* **179**, 14 (2009).
- [58] P. K. Patro and G. D. Egbert, *Geophysical Research Letters* **25**, L20311 (2008).
- [59] D. K. Butler, *Near-Surface Geophysics*, Vol. 13 (Society of Exploration Geophysicists, 2008).
- [60] K. Bahr, *Physics of the Earth and Planetary Interiors* **66**, 24 (1991).
- [61] K. Baba, A. D. Chave, R. L. Evans, G. Hirth, and R. L. Mackie, *Journal of Geophysical Research Solid Earth* **111**, B02101 (2006).
- [62] USGS, Usgs geological map database,  
<https://www.usgs.gov/products/maps/geologic-maps>.
- [63] J. McNeil, *Geonics LTD TN5* (1980).
- [64] A. Duba, A. J. Piwinskii, M. Santor, and H. C. Weed, *Geophysical Journal of the Royal Astronomical Society* **53**, 583 (1978).
- [65] S. Garambois, P. Senechal, and H. Perroud, *Journal of Hydrology* **259**, 32 (2002).
- [66] Z. Fadhli, R. Saad, M. M. Nordiana, M. Syukri, I. N. Azwin, and A. A. Bery, *Electronic Journal of Geotechnical Engineering* **20**, 1447 (2015)